VALIDATION OF EXPERIMENTAL-ANALYTICAL SUBSTRUCTURING USING THE TRANSMISSION SIMULATOR METHOD

by

Daniel P. Rohe

A thesis submitted in partial fulfillment of

the requirements for the degree of

Master of Science

Engineering Mechanics

at the

UNIVERSITY OF WISCONSIN-MADISON

2012

ABSTRACT

Dynamic substructuring provides an analyst the ability to perform tests on small, simple structures and combine them into a single built-up structure. This methodology often decreases the cost of analysis because expensive tests and simulations on large models can be avoided in favor of smaller, component-level tests. Dynamic substructuring has been successfully utilized in the analytical domain for several decades; however, experimental substructuring has lagged behind. Experimental substructuring often gives poor results due to sensitivity of the applied constraints to experimental errors, leading analysts to be reluctant to use it.

A new method for substructuring, dubbed the Transmission Simulator Method, has shown promise to reduce this sensitivity by softening the constraints. However, even with this new methodology, substructuring can give poor results. It would be helpful to be able to perform a some type of validation to give confidence in the results predicted by substructuring. This validation experiment is ideally inexpensive to perform and analyze as to not add significant cost to performing a substructuring analysis.

This thesis initially examines results from two substructuring attempts on similar structures, one that was successful and one that was not. Then, a simpler system will be analyzed to determine which types of errors cause substructuring to go awry. A Monte-Carlo simulation is performed in which random errors are applied to the system before substructuring is performed. Finally, a more complex validation scenario is analyzed. Substructuring is attempted on a complicated, three-dimensional example with many degrees of freedom and a complicated multi-point interface.

TABLE OF CONTENTS

NOMENCLATURE

Sorted in order of appearance:
$\mathbf{I}$ – Identity Matrix
$\mathbf{q}$ – Modal degree of freedom
ζ – Damping ratio
ω – Angular natural frequency (rad/s)
$\mathbf{\Phi}$ – Mode shape matrix
$\mathbf{F}$ – Generalized force vector
$[\ddots]$ - Diagonal matrix
$\mathbf{B}_p$ – Physical constraint matrix
$\mathbf{B}$ – Modal constraint matrix
$\mathbf{x}$ – Physical degree of freedom
$\mathbf{L}$ – Transformation matrix
$\mathbf{q}_u$ – Unconstrained generalized coordinate
null( ) – Function returning the null space of the argument
$^+$ - Pseudo-inverse of a matrix
$\mathbf{M}$ – Generalized mass matrix
$\mathbf{C}$ – Generalized damping matrix
$\mathbf{K}$ – Generalized stiffness matrix
$\widehat{\mathbf{M}}$ – Unconstrained mass matrix
$\widehat{\mathbf{C}}$ – Unconstrained damping matrix
$\widehat{\mathbf{K}}$ – Unconstrained stiffness matrix
f – Natural frequency (Hz)
F – Frequency weighting factor for mode correlation
$MAC(\ )$ - Function returning the modal assurance criterion between the two arguments
W_{ij} – Mode selection weights between the ith truth mode and the jth substructured mode
$\mathbf{N}$ – Noise matrix for creating noisy mode shapes
$\mathbf{\Phi}_n$ **–** Noisy mode shape matrix

ACKNOWLEDGEMENTS

First, I would like to thank my advisor Professor Matthew Allen for the opportunity to work on this project. His helpful insights and willingness to help have made him instrumental in the completion of this body of work.

Second, I would like to thank Randy Mayes for giving me the opportunity to work with him over the summer at Sandia National Laboratories. Working with someone with such immeasurable experience in the field of experimental modal analysis and testing was a great benefit to my research, and his guidance was much appreciated. Being able to use the resources of the Modal Lab at Sandia helped immensely to take good data for the experimental portions of this work.

I would also like to thank Sandia National Laboratories and the National Physical Science Consortium for supporting my research financially. Sandia is a multiprogram laboratory operated by Sandia Corporation, a Lockheed Martin Company, for the U.S. Department of Energy under Contract DE-AC04-94AL85000. Kohler Company also supported this research through the donation of finite element models which provided the basis for a significant portion of the work in this thesis.

Finally, I would like to thank my fiancée Nikki for putting up with my schedule and providing support and encouragement throughout my graduate studies. You kept me grounded when I was stressed out, and you kept me motivated when I wanted to slack off.

1. Introduction

Experimental-Analytical substructuring is a technique in which a model of a specific subcomponent is derived experimentally and coupled to an analytical representation of the rest of the system to predict the assembled response. This technique is particularly well-suited to situations in which a subcomponent may be difficult to analytically model. If a material has intricate geometric features or uncertain or complex material properties, an experimental model may be less expensive to generate.

However, several barriers exist to creating a good experimental subcomponent. Modal truncation is always an issue, since one can never capture all of the modes of a system; this must be considered in the creation of a model. Additionally, some constraints between the experimental and analytical subcomponent may require knowledge of the displacements and rotations at each connection point, with the latter being much more difficult to measure. Additionally, the connection points on the experimental substructure may not be accessible for instrumentation if the joint is complex. Experiments also necessarily have some level of error, to which experimental substructuring can be very sensitive. For these reasons, experimental substructuring has remained underutilized in industry.

1.1. Substructuring Methodology

Substructuring exists in multiple forms, and de Klerk, Rixen, and Voormeeren give a good overview of the various techniques [1]. As all of the work in this thesis uses the Component Mode Synthesis technique, the general methodology will be reproduced here for the reader's convenience.

Components of the system of interest (here A and B) are represented using modal parameters (natural frequencies, mode shapes, and damping ratios) in the typical equation of motions cast in modal form, and they are concatenated to form a global system of equations.

$$\begin{bmatrix} \mathbf{I}_A & \mathbf{0} \\ \mathbf{0} & \mathbf{I}_B \end{bmatrix} \begin{Bmatrix} \ddot{\mathbf{q}}_A \\ \ddot{\mathbf{q}}_B \end{Bmatrix} + \begin{bmatrix} \ddots 2\zeta_A \omega_A \ddots & \mathbf{0} \\ \mathbf{0} & \ddots 2\zeta_B \omega_B \ddots \end{bmatrix} \begin{Bmatrix} \dot{\mathbf{q}}_A \\ \dot{\mathbf{q}}_B \end{Bmatrix} + \begin{bmatrix} \ddots \omega_A^2 \ddots & \mathbf{0} \\ \mathbf{0} & \ddots \omega_B^2 \ddots \end{bmatrix} \begin{Bmatrix} \mathbf{q}_A \\ \mathbf{q}_B \end{Bmatrix} = \begin{Bmatrix} \boldsymbol{\Phi}_A^T \mathbf{F}_A \\ \boldsymbol{\Phi}_B^T \mathbf{F}_B \end{Bmatrix} \tag{1.1.1}$$

The assumption here is that the mode shapes are mass-normalized, so the mass matrix becomes an identity matrix. Constraints between the subsystems can be added in the form

$$\mathbf{B}_p \begin{Bmatrix} \mathbf{x}_A \\ \mathbf{x}_B \end{Bmatrix} = \mathbf{0} \tag{1.1.2}$$

Typically the $\mathbf{B}_p$ matrix will be a signed Boolean matrix as the motions between degrees of freedom will be set equal to one another. The $\mathbf{B}_p$ matrix will be, for example, $[1 \quad -1]$ if $\mathbf{x}_A$ and $\mathbf{x}_B$ are scalars and constrained to move together.

The constraints for the ith subsystem can be cast into modal coordinates by using the transformation into modal coordinates $\mathbf{x}_i = \boldsymbol{\Phi}_i \mathbf{q}_i$.

$$\mathbf{B}_p \begin{bmatrix} \boldsymbol{\Phi}_A & \mathbf{0} \\ \mathbf{0} & \boldsymbol{\Phi}_B \end{bmatrix} \begin{Bmatrix} \mathbf{q}_A \\ \mathbf{q}_B \end{Bmatrix} = \mathbf{0} \tag{1.1.3}$$

or

$$\mathbf{B}\begin{Bmatrix}\mathbf{q}_A\\ \mathbf{q}_B\end{Bmatrix} = \mathbf{B}\mathbf{q} = 0 \qquad (1.1.4)$$

The goal is now to seek some transformation which will transform the set of constrained modal coordinates to some unconstrained set of generalized coordinates $\mathbf{q}_u$. This transformation will be of the form $\mathbf{q} = \mathbf{L}\mathbf{q}_u$. When substituted into equation (1.1.4) this yields

$$\mathbf{B}\mathbf{L}\mathbf{q}_u = \mathbf{0} \qquad (1.1.5)$$

which, for a general $\mathbf{q}_u$ means that the transformation matrix $\mathbf{L}$ must span the null space of $\mathbf{B}$.

$$\mathbf{L} = \text{null}(\mathbf{B}) \qquad (1.1.6)$$

This transformation can then be applied to the full equations of motion, for which the eigenproblem can be solved and natural frequencies, damping ratios, and mode shapes can be derived, which are the modal properties for the substructured system.

$$\begin{aligned}
&\hat{\mathbf{M}}\ddot{\mathbf{q}}_u + \hat{\mathbf{C}}\dot{\mathbf{q}}_u + \hat{\mathbf{K}}\mathbf{q}_u = \mathbf{Q}\\
&\hat{\mathbf{M}} = \mathbf{L}^T\begin{bmatrix}\mathbf{I}_A & \mathbf{0}\\ \mathbf{0} & \mathbf{I}_B\end{bmatrix}\mathbf{L}\\
&\hat{\mathbf{C}} = \mathbf{L}^T\begin{bmatrix}\begin{bmatrix}\ddots & \\ & 2\zeta_A\omega_A\end{bmatrix} & \mathbf{0}\\ \mathbf{0} & \begin{bmatrix}\ddots & \\ & 2\zeta_B\omega_B\end{bmatrix}\end{bmatrix}\mathbf{L}\\
&\hat{\mathbf{K}} = \mathbf{L}^T\begin{bmatrix}\begin{bmatrix}\ddots & \\ & \omega_A^2\end{bmatrix} & \mathbf{0}\\ \mathbf{0} & \begin{bmatrix}\ddots & \\ & \omega_B^2\end{bmatrix}\end{bmatrix}\mathbf{L}\\
&\mathbf{x} = \begin{bmatrix}\boldsymbol{\Phi}_A & \mathbf{0}\\ \mathbf{0} & \boldsymbol{\Phi}_B\end{bmatrix}\mathbf{L}\mathbf{q}_u
\end{aligned} \qquad (1.1.7)$$

It should be noted that the constraints applied to substructure these system are ‘hard’ constraints, and require strict obedience from the degrees of freedom to which they are applied. This is adequate for analytical substructuring where results are ‘perfect’ to computational precision, but it can be detrimental to experimental substructuring in which there may be small errors. A new substructuring method has recently been introduced to try to alleviate this and other issues.

1.2. The Transmission Simulator Method

Recently, a new method of dynamic substructuring, dubbed the Transmission Simulator (TS) Method in [2], has shown promising results in reducing the problems discussed previously. The transmission simulator method is named after the ‘transmission simulator’, a fixture that simulates the boundary condition between the experimental substructure and analytical substructures. This fixture helps to mass-load the interface between the two subcomponents, which provides a better set of basis vectors for substructuring. Additionally, the increased mass loading can shift modes down into the testable frequency band. However, the TS substructure does not exist in the final built up system, so it must be subtracted typically using an analytical representation of the free-free transmission simulator. If this analytical representation of the transmission simulator does not perfectly match the experimental model derived from the test, errors in the subtraction can lead to negative mass or stiffness developing, but efforts have been made to diagnose [3] and correct [4] this negative mass or stiffness, so this has not been a substantial issue.

Since the transmission simulator method requires the subtraction of the transmission simulator, a new, negative TS subsystem must be concatenated into the system. In the example substructuring of system A and B shown previously, this will look like

$$\begin{bmatrix} \mathbf{I}_A & & 0 \\ & \mathbf{I}_B & \\ 0 & & -\mathbf{I}_{TS} \end{bmatrix} \begin{Bmatrix} \ddot{\mathbf{q}}_A \\ \ddot{\mathbf{q}}_B \\ \ddot{\mathbf{q}}_{TS} \end{Bmatrix} + \begin{bmatrix} \begin{bmatrix} \ddots 2\zeta_A\omega_A \ddots \end{bmatrix} & & 0 \\ & \begin{bmatrix} \ddots 2\zeta_B\omega_B \ddots \end{bmatrix} & \\ 0 & & -\begin{bmatrix} \ddots 2\zeta_{TS}\omega_{TS} \ddots \end{bmatrix} \end{bmatrix} \begin{Bmatrix} \dot{\mathbf{q}}_A \\ \dot{\mathbf{q}}_B \\ \dot{\mathbf{q}}_{TS} \end{Bmatrix} + \begin{bmatrix} \begin{bmatrix} \ddots \omega_A^2 \ddots \end{bmatrix} & & 0 \\ & \begin{bmatrix} \ddots \omega_B^2 \ddots \end{bmatrix} & \\ 0 & & -\begin{bmatrix} \ddots \omega_{TS}^2 \ddots \end{bmatrix} \end{bmatrix} \begin{Bmatrix} \mathbf{q}_A \\ \mathbf{q}_B \\ \mathbf{q}_{TS} \end{Bmatrix} = \begin{Bmatrix} \boldsymbol{\Phi}_A^T \mathbf{F}_A \\ \boldsymbol{\Phi}_B^T \mathbf{F}_B \\ \boldsymbol{\Phi}_{TS}^T \mathbf{F}_{TS} \end{Bmatrix} \quad (1.2.1)$$

Variations on this method in which two transmission simulators are used (one on each of system A and B) have been utilized in the past [5], and in this case the bottom block row of equation (1.2.1) corresponding to the transmission simulator can simply be multiplied by 2, since two transmission simulators will now be subtracted. All the cases studied in this thesis only use one transmission simulator, and will follow the formulation shown in (1.2.1)

The transmission simulator method also modifies the point-by-point constraints applied by typical substructuring methods. Instead of strict enforcement of the hard constraints shown in (1.1.4), the constraints are softened and satisfied in a least-squares sense. This constraint method, dubbed Modal Constraints for Fixture and Subsystem (MCFS) [5], weights the constraint equations with the pseudoinverse of the transmission simulator mode shapes partitioned to the measurement points, designated by the subscript m. The measurement

points are defined as the measured points on the transmission simulator that will be used to apply constraints, and are analogous to interface degrees of freedom in point-by-point constraints.

$$\boldsymbol{\Phi}_{TS,m}^{+}\mathbf{x}_{A,m} = \boldsymbol{\Phi}_{TS,m}^{+}\mathbf{x}_{TS,m} \qquad (1.2.2)$$

Similar to the point-by-point method, this constraint can be cast into modal form, which reduces to

$$\boldsymbol{\Phi}_{TS,m}^{+}\boldsymbol{\Phi}_{A,m}\mathbf{q}_{A} = \mathbf{q}_{TS} \qquad (1.2.3)$$

Performing the same computation on system B and switching to matrix form gives the entire set of constraint equations

$$\begin{bmatrix} \boldsymbol{\Phi}_{TS,m}^{+}\boldsymbol{\Phi}_{A,m} & \mathbf{0} & -\mathbf{I} \\ \mathbf{0} & \boldsymbol{\Phi}_{TS,m}^{+}\boldsymbol{\Phi}_{B,m} & -\mathbf{I} \end{bmatrix} \begin{Bmatrix} \mathbf{q}_{A} \\ \mathbf{q}_{B} \\ \mathbf{q}_{TS} \end{Bmatrix} = \mathbf{B}\mathbf{q} = \mathbf{0} \qquad (1.2.4)$$

from which Equation (1.1.6) and onwards can be used to formulate the substructured model properties.

2. Substructuring Examples on the Ampair 600 Wind Turbine

Even with the introduction of the transmission simulator method to alleviate some of the problems when substructuring with experimental substructures, it is still possible to obtain poor results using it. Based on its history, experimental substructuring is not used very often in industry due to a lack of confidence in the results. This section illustrates two examples of experimental substructuring on the Ampair 600 Wind Turbine [6]. This structure was selected by the Substructures Focus Group at the International Modal Analysis Conference

(IMAC) to serve as a test bed for substructuring. Various organizations have performed or plan to perform tests on this system.

The first test attempted to couple a blade of the Ampair 600 Wind Turbine to the rest of the turbine structure. This test was not successful in predicting the response of the built up turbine. The second example was performed almost a year later after the author had gained considerable experience with experimental modal analysis and substructuring. The attempt successfully coupled the Ampair Wind Turbine hub with blades attached to the nacelle. In both cases, a full, system-level test was performed to which the substructured results could be compared. In practice, such truth data is often unavailable, though in this case it is helpful to evaluate the performance of the substructuring method.

2.1. Substructuring a Wind Turbine Blade to a Turbine System

This experiment attempted to predict the response of the entire Ampair Wind Turbine system based on experimental subcomponent models of the blade and the turbine with a blade removed. Three modal tests were performed to characterize the two systems shown in Figure 2.1.1 as well as the final built up system to validate the substructured models.

Figure 2.1.1: Components tested for initial turbine substructuring. The full turbine missing one blade (left) and the missing blade (top right). A transmission simulator (bottom right) was fixed to the blade to mass-load the interface.

For these tests, the coordinate system used had its origin at the base of the tower. The y-direction pointed up along the tower. The z-direction pointed along the direction the turbine was facing, and the x-direction pointed in the direction perpendicular to the y and z axes, forming the appropriate right-handed coordinate system.

2.1.1. Experimental Setup

Data was taken using roving ¼ pound hammer inputs with a soft plastic tip with accelerometers located near the blade tips and on the nacelle. The frequency range of the tests was up to 500 Hz. All test boundary conditions were approximated as free-free. The

full turbine system and the turbine system missing a blade were both supported on a commercial trampoline which was modified to decrease its stiffness. The blade was hung from soft bungee cords.

The structures were excited at a large number of points, which provided very good spatial resolution for the mode shapes. The line models derived from the input locations are shown in Figure 2.1.2. Responses and force inputs were averaged over 10 impacts at each point.

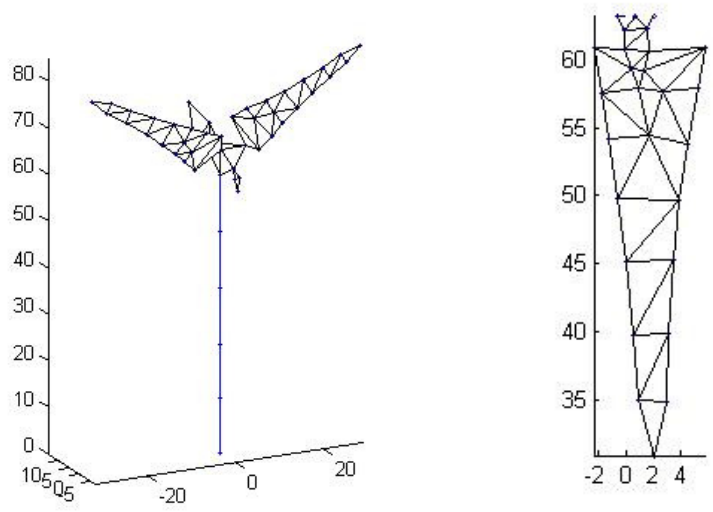

Figure 2.1.2: Two-bladed turbine and mass-loaded blade geometry. Units are inches.

The transmission simulator in this case was a steel block sandwiched between two aluminum plates. The fixture provided additional mass-loading to the blade interface, and attached to the blade similarly to how the blade would attach to the built-up structure. The transmission simulator was designed to be as simple as possible while still imitating the joint. Over the frequency range of interest the transmission simulator was assumed to be rigid, having only the six rigid body modes—three principal translations and rotations. This allowed an

accurate transmission simulator model, since only its mass properties and measurement point geometry were needed to construct an accurate model.

Since all structures were assumed to have free-free boundary conditions, rigid body modes were needed to complete each modal model. These were constructed using approximated mass properties for the system. Each component's mass could be easily determined by weighing the structure, but rotational inertia was more complex to derive. Simplified solid models were created and assigned material densities based on weights of the components. For example, the two-bladed turbine was split up into the cylindrical base, the tower, the nacelle and hub, and the blades. Each component was weighed (Table 2.1.2) and given a uniform density to match that weight. Rotational inertia values were then extracted from the solid models generated in the SolidWorks modeling software, shown in Figure 2.1.3. This does leave room for errors; however, at the time very little was known about the turbine and blade geometry.

Hub/Nacelle/Tail	Blade	Tower	Base
12.88 kg	0.935 kg	5.59 kg	93.82 kg

Table 2.1.1: Component masses used in the construction of rigid body modes.

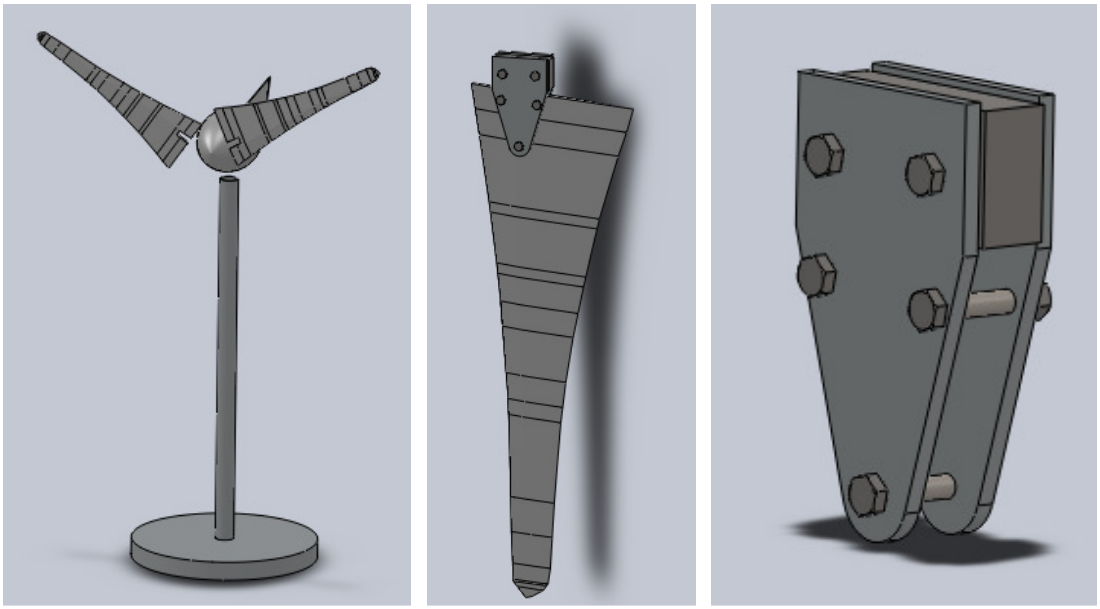

Figure 2.1.3: Rough solid models from which the mass properties of each component were derived.

2.1.2. Blade Results

The blade test was performed and the natural frequencies, damping ratios, and mode shapes were extracted using the Algorithm of Mode Isolation (AMI) [7]. Figure 2.1.4 shows the isolation and refinement step of the algorithm and can indicate the adequacy of the modal parameter fit. All the peaks appear to be fit well, but the low level data between the peaks appears contaminated. Because the Ampair turbine is shared between multiple research institutions, it needed to be shipped elsewhere before any new data could be taken.

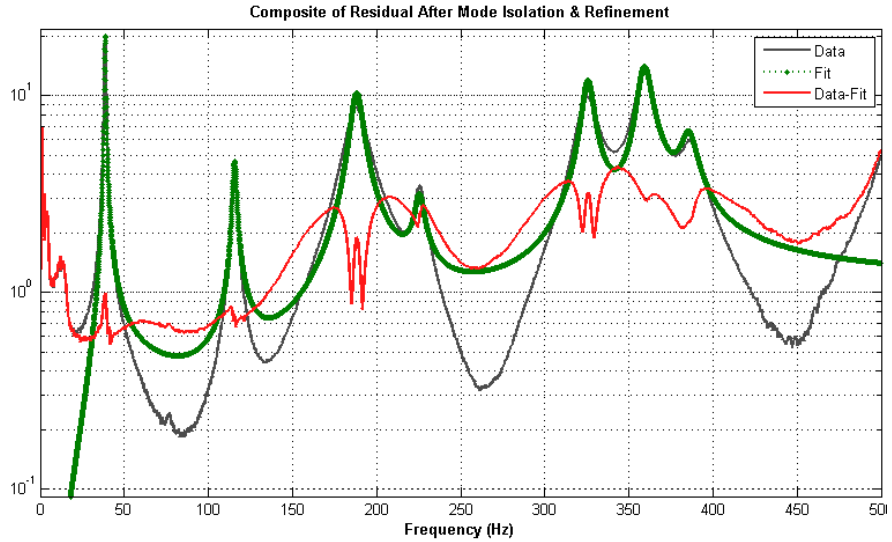

Figure 2.1.4: Algorithm of Mode Isolation (AMI) isolation and refinement phase. The peaks were fit with reasonable accuracy, but significant errors between the peaks suggest that there are problems with the data.

The blade modes extracted from this frequency range are summarized in Table 2.1.2.

Mode	Frequency	Damping Ratio	Description
1	0.00	0.00%	x-direction Translation
2	0.00	0.00%	y-direction Translation
3	0.00	0.00%	z-direction Translation
4	0.00	0.00%	Rotation about x
5	0.00	0.00%	Rotation about y
6	0.00	0.00%	Rotation about z
7	38.62	0.83%	1st Bending
8	115.55	0.98%	2nd Bending
9	188.06	1.86%	1st Torsion
10	225.01	1.21%	2nd Torsion
11	325.58	1.02%	3rd Torsion/Bending
12	359.01	1.15%	See Figure 2.1.5
13	377.41	5.25%	See Figure 2.1.5
14	385.73	1.29%	Torsion

Table 2.1.2: List of modes used in the blade subsystem. The first six modes are rigid body modes created from mass properties. The rest were extracted from modal data.

Select mode shapes are shown in Figure 2.1.5. All extracted mode shapes are summarized in Appendix A. It is easy to classify the first few elastic mode shapes as bending and torsion mode shapes; however some of the higher frequency modes were harder to classify in this manner, for instance, the 7th elastic mode which is shown in Figure 2.1.5.

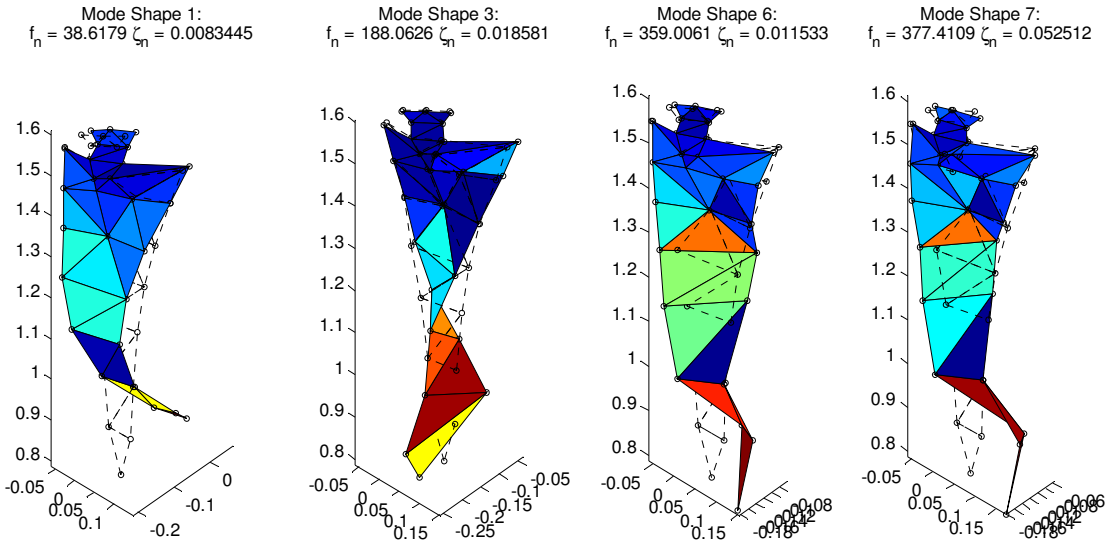

Figure 2.1.5: The first, third, sixth, and seventh elastic mode shapes. This shows the first bending mode, first torsion mode, and two harder-to-classify edgewise modes.

2.1.3. Two-Bladed Turbine Results

The two-bladed turbine data was analyzed similarly to the blade. The AMI algorithm was used to extract modes up to 250 Hz. Figure 2.1.6 shows the isolation and refinement step of the AMI process. The low frequency modes are fit well, but a fairly high residual in the higher frequency portion. The two modes near 175 Hz were not extracted very well.

The blade modes extracted from this frequency range are summarized in Table 2.1.3.

Mode	Frequency	Damping Ratio	Description
1	0	0.00%	x-direction Translation
2	0	0.00%	y-direction Translation
3	0	0.00%	z-direction Translation
4	0	0.00%	Rotation about x
5	0	0.00%	Rotation about y
6	0	0.00%	Rotation about z
7	17.54	0.73%	Blade Bending, Tower Torsion
8	18.65	0.74%	Blades Bending In Phase
9	20.43	0.56%	Tower Bending in xy-plane
10	21.54	0.69%	Tower Bending in yz-plane, Blades in phase
11	35.71	0.90%	Blade Edgewise and some Bending
12	39.19	0.63%	Tail flapping, Tower Torsion, Blade Bending
13	58.27	1.30%	Blade Edgewise and Bending
14	61.66	1.52%	Blade Bending Tower Torsion
15	73.39	0.89%	Left Blade Second Bending
16	81.35	1.08%	Right Blade Second Bending
17	99.68	1.18%	Both Blades Second Bending
18	100.01	0.79%	Tower Bending in xz-plane, Tail Flap in phase
19	108.78	0.90%	Tower Bending in xz-plane, tail flap out of phase
20	132.97	1.07%	Both Blades Third Bending
21	148.00	0.70%	See Appendix A
22	167.90	1.55%	See Appendix A
23	179.66	1.55%	See Appendix A
24	201.27	0.46%	See Appendix A
25	202.92	1.08%	See Appendix A
26	217.47	0.87%	See Appendix A
27	235.87	1.00%	See Appendix A
28	242.25	0.35%	See Appendix A

Table 2.1.3: List of modes used in substructuring calculations from the Two-Bladed Turbine system. The first six modes are rigid body modes created from approximated mass properties, and the rest are extracted from test data. Note that for higher frequencies, mode shapes become combinations of different kinds of tail, blade, and tower motion, so condensing this complex motion into a brief description is difficult.

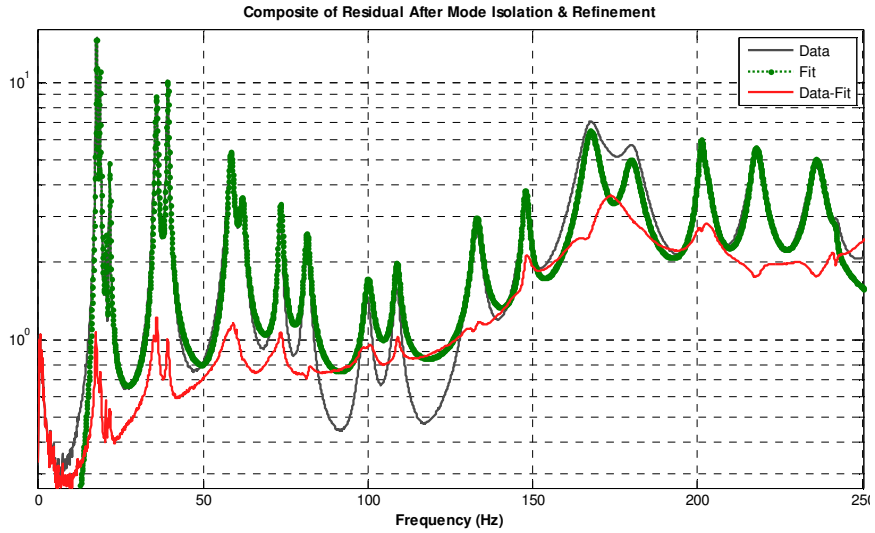

Figure 2.1.6: AMI isolation and refinement phase. The low frequency modes are fit well but there are some issues in near 175 Hz.

2.1.4. Substructuring Methodology

The two substructure models discussed in the previous two sections along with a transmission simulator model consisting of its six rigid-body modes created from mass properties were coupled together. All extracted mode shapes were mass normalized, giving the equations of motion shown below, where the subscript B represents the blade subsystem, the subscript T represents the two-bladed turbine subsystem, and the subscript TS represents the transmission simulator.

$$\begin{bmatrix} \mathbf{I}_T & & 0 \\ & \mathbf{I}_B & \\ 0 & & -\mathbf{I}_{TS} \end{bmatrix} \begin{Bmatrix} \ddot{\mathbf{q}}_T \\ \ddot{\mathbf{q}}_B \\ \ddot{\mathbf{q}}_{TS} \end{Bmatrix}$$

$$+ \begin{bmatrix} \left[\ddots 2\zeta_T \omega_T \ddots\right] & & 0 \\ & \left[\ddots 2\zeta_B \omega_B \ddots\right] & \\ 0 & & -\left[\ddots 2\zeta_{TS} \omega_{TS} \ddots\right] \end{bmatrix} \begin{Bmatrix} \dot{\mathbf{q}}_T \\ \dot{\mathbf{q}}_B \\ \dot{\mathbf{q}}_{TS} \end{Bmatrix} \qquad (2.1.1)$$

$$+ \begin{bmatrix} \left[\ddots \omega_T^2 \ddots\right] & & 0 \\ & \left[\ddots \omega_B^2 \ddots\right] & \\ 0 & & -\left[\ddots \omega_{TS}^2 \ddots\right] \end{bmatrix} \begin{Bmatrix} \mathbf{q}_T \\ \mathbf{q}_B \\ \mathbf{q}_{TS} \end{Bmatrix} = \begin{Bmatrix} \mathbf{\Phi}_T^T \mathbf{F}_T \\ \mathbf{\Phi}_B^T \mathbf{F}_B \\ \mathbf{\Phi}_{TS}^T \mathbf{F}_{TS} \end{Bmatrix}$$

To couple the blade and the negative transmission simulator model, the six modal constraints corresponding to the six rigid body modes of the transmission simulator were used. These six constraints were averaged over all the measurement points in the transmission simulator model (Figure 2.1.7 left).

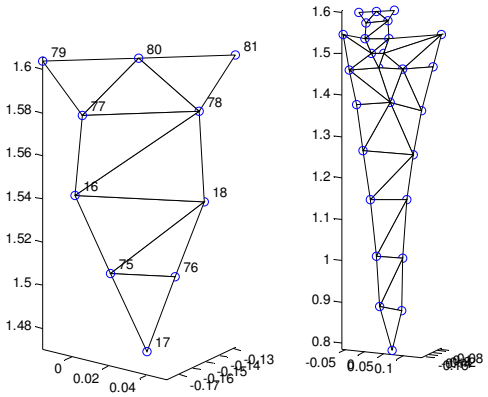

Figure 2.1.7: Figure showing the transmission simulator measurement points (left) and all the blade points (right). The six rigid body modes were applied all the points on the transmission simulator.

The second set of constraints applied to the system consisted of six point constraints to couple the blade to the hub. Since there were three points in common (the three bolts) each

with three degrees of freedom, six constraints were selected from the nine bolt degrees of freedom to perform the constraint: $16x$, $16y$, $16z$, $17y$, $17z$, and $18z$.

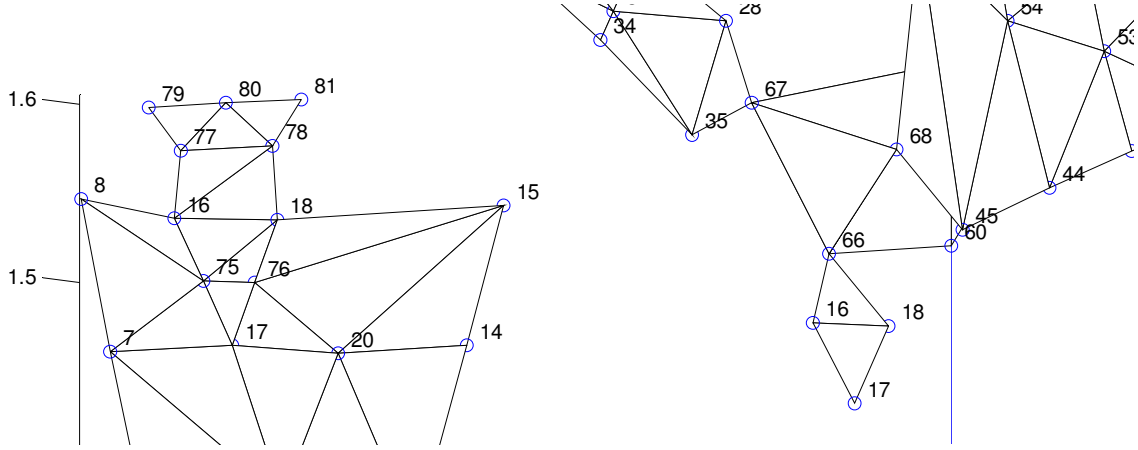

Figure 2.1.8: Degrees of freedom 16, 17, and 18 are the bolt degrees of freedom to which constraints were applied, shown in both the blade and turbine models. They also exist on the transmission simulator.

It is important to note that these degrees of freedom exist on both the blade and the transmission simulator, and so an important distinction exists between coupling the turbine to the blade degrees of freedom and coupling the turbine to the transmission simulator degrees of freedom. Since the least-squares modal constraint was used, the motion of the transmission simulator degrees of freedom will not exactly equal the motion of the blade degrees of freedom. Since there are inevitably errors in the motion of the blade degrees of freedom, it is better to apply the constraints to the transmission simulator, which can only move as a rigid body. Since it is constructed analytically, there should be no errors in these degrees of freedom. In contrast, if one were to constrain the blade degrees of freedom, it would be similar to doing a simple point-by-point connection scheme between the two

models, and the error-sensitivity-reducing effects of the transmission simulator method would be eliminated.

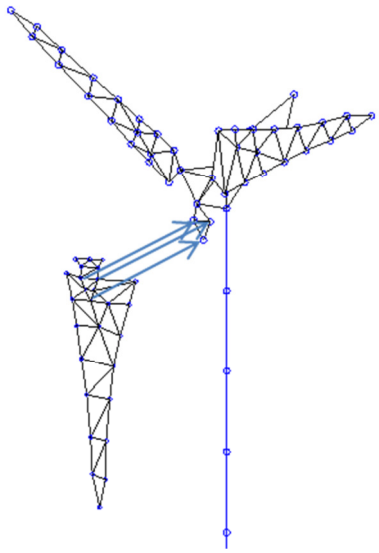

Figure 2.1.9: Visualization of constraints from the transmission simulator bolt degrees of freedom to the turbine bolt degrees of freedom. Only six of the nine degrees of freedom were used in the constraint.

The constraint equations then look like

$$\begin{bmatrix} \boldsymbol{\Phi}_{T,CPT} & \mathbf{0} & \boldsymbol{\Phi}_{TS,CPT} \\ \mathbf{0} & \boldsymbol{\Phi}_{TS,m}^{+}\boldsymbol{\Phi}_{B,m} & \mathbf{I} \end{bmatrix} \begin{Bmatrix} \mathbf{q}_T \\ \mathbf{q}_B \\ \mathbf{q}_{TS} \end{Bmatrix} = \mathbf{B}\mathbf{q} = \mathbf{0} \qquad (2.1.2)$$

where the subscript CPT represents a partition of the mode shape matrix to the connection point degrees of freedom $16x$, $16y$, $16z$, $17y$, $17z$, and $18z$, and the subscript m represents a partition of the mode shape matrix to the degrees of freedom in the transmission simulator. Then the substructuring calculations may proceed as in equations (1.1.5) through (1.1.7).

2.1.5. Substructuring Results

The substructuring calculations were performed, and the results were compared to a truth model derived from a modal test on the entire turbine. The Modal Assurance Criterion (MAC) was used to compare mode shapes between the two tests, which was possible since the truth test had the same accelerometer and input locations as the subcomponent tests. For each truth mode, a substructured mode was assigned for it based on the highest MAC correlation. A plot of the MAC between the two systems is shown in Figure 2.1.10. It is clear that the majority of the mode shapes are poor matches between the two substructures. There are also two substructured modes missing from the representation that should correlate with truth modes 20 and 24.

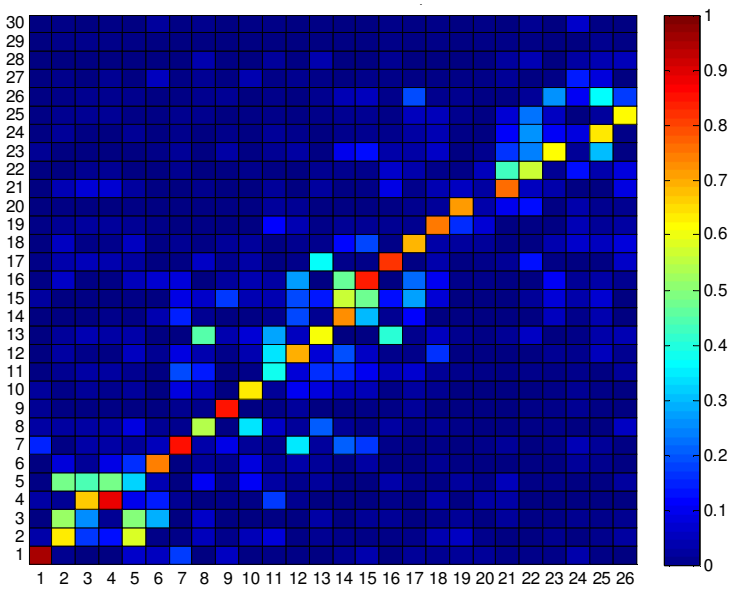

Figure 2.1.10: MAC plot between the truth test modes (columns) and substructured model modes (rows). Although a diagonal is visually present, none of the values on the diagonal are particularly strong, signifying poor mode shape correlation. Note only the elastic modes are compared, so mode 1 corresponds to mode 7 from the previous table.

The modal properties of the truth modes and the correlated substructured modes are then compared in Table 2.1.4.

Truth Mode	Freq (Hz)	SS Mode	Freq (Hz)	Error	MAC
1	17.52	1	17.43	-0.52%	0.9629
2	18.22	2	18.32	0.52%	0.6455
3	19.46	4	21.36	9.77%	0.6776
4	20.8	4	21.36	2.70%	0.8974
5	21.64	2	18.32	-15.34%	0.59
6	31.62	6	30.59	-3.24%	0.7517
7	38.19	7	38.61	1.09%	0.8627
8	52.6	8	56.51	7.44%	0.5515
9	60.66	9	60.18	-0.79%	0.8586
10	64.07	10	65.92	2.89%	0.6465
11	72	11	76.2	5.83%	0.3909
12	74.16	12	79.24	6.84%	0.7049
13	87.26	13	86.23	-1.18%	0.6189
14	99.74	14	99.75	0.01%	0.7372
15	109.9	16	108.8	-1.00%	0.8495
16	126.8	17	124.7	-1.62%	0.8274
17	146.3	18	145.9	-0.24%	0.6979
18	155.3	19	162.9	4.91%	0.7579
19	172.7	20	175.7	1.79%	0.7244
20	173.9	19	162.9	-6.29%	0.0818
21	179.1	21	188.2	5.08%	0.7706
22	186.8	22	195.3	4.58%	0.5754
23	201.4	23	203.3	0.92%	0.6262
24	212.9	27	323.3	51.88%	0.1501
25	219.3	24	217.1	-0.97%	0.6478
26	226.4	25	227.6	0.53%	0.6292

Table 2.1.4: Substructured frequency comparison for correlated modes. Note that only elastic modes are compared in this table, so elastic mode 1 is actually mode 7 since there are six rigid body modes.

Table 2.1.4 shows multiple frequencies with very high errors. There are also instances where one substructured mode had the strongest correlation to two truth modes. It is clear that this

substructured model is not a very good representation of the truth data. However, effort on this problem had to be discontinued because the turbine needed to be shipped to a conference, so no new data could be taken.

Since a truth data was available from a test of the full system, it was known that the results were not very good. But if no truth data was available, we would have no knowledge of the accuracy of the results. A more complete discussion of the results of this test will occur in Section 2.3.

2.2. Substructuring a Bladed Hub to a Bladeless Wind Turbine

Since the first test was unsuccessful, a second test was performed when the opportunity presented itself. The objective of these tests was to create a substructured model of the Ampair 600 Wind Turbine, similar to the last test, but assembled from component models of the tower and a blades-and-hub structure, which differed from the last test. This model was again compared to an experimental 'truth' model from a modal test of the entire assembled structure. The scope of the test was refined. Instead of simply specifying an arbitrary frequency range and extracting as many modes as possible, the frequency range was selected based on specific modes that were desired. Of interest in these experiments were the modes up to the second bending modes of the tower and blades. Previous tests containing these structures in similar configurations [6],[8] showed that the highest frequencies of interest would occur near 100 Hz. Though the second bending mode of the blade from the previous test was over 100 Hz, the hub boundary condition would lower this frequency. The test range was set from 0 to 156.25 Hz to allow these modes (and a few higher) to be captured.

For each test, a 0.3 kg (0.7 lb) impact hammer with the softest available tip was used to excite the structures' elastic modes. The modes were extracted with the "Synthesize Modes and Correlate" (SMAC) algorithm [9].

The pitch, roll, and yaw nomenclature as used in this test are defined as the rotations about the x, z, and y directions, respectively, as shown in Figure 2.2.1. The origin of the coordinate system is defined as the tip of the hub, placing the majority of the structure in the $-z$ direction, to be consistent with the testing done in [6].

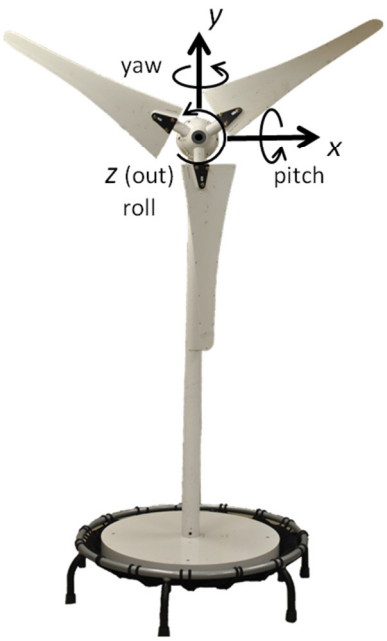

Figure 2.2.1: Global coordinate system and rotation definitions.

2.2.1. Test Structures

Tests were performed on two different substructures in order to assemble them into the complete Ampair turbine structure. The first structure was the hub, disconnected from the nacelle at the mock generator shaft, with the blades attached. The second substructure was

the turbine with the hub locked to the parked shaft and the blades removed. Both structures are shown in Figure 2.2.2. Since both structures include the hub, one will need to be subtracted as is common in the transmission simulator method.

Figure 2.2.2: Structures tested to perform substructuring. (a) Bladeless tower (left) and (b) hub and blades (right)

2.2.2. Bladeless Tower Test

2.2.2.1. Test Setup

Mode shapes from previous tests revealed rough location for tower nodes, which would need to be avoided when placing accelerometers. The tower was instrumented such that the first and second bending of the tower would be visible and distinguishable from one another. The hub and nacelle were both instrumented such that relative rigid body motions between the two components would be visible, and the tail was instrumented to distinguish flapping and torsion modes. The massive base of the tower was instrumented with four high-sensitivity

(500 mV/g) accelerometers because its motion tended to be very small due to its large mass. Accelerometer locations and a line model are shown in Figure 2.2.3.

The structure was excited at a large number of drive points in order to ensure that all of the modes were excited adequately. The tower was impacted to excite pole bending modes. Several drive points were chosen on the transmission simulator, both on the arms (white) and on the clamps (black). The lower tail point was also excited.

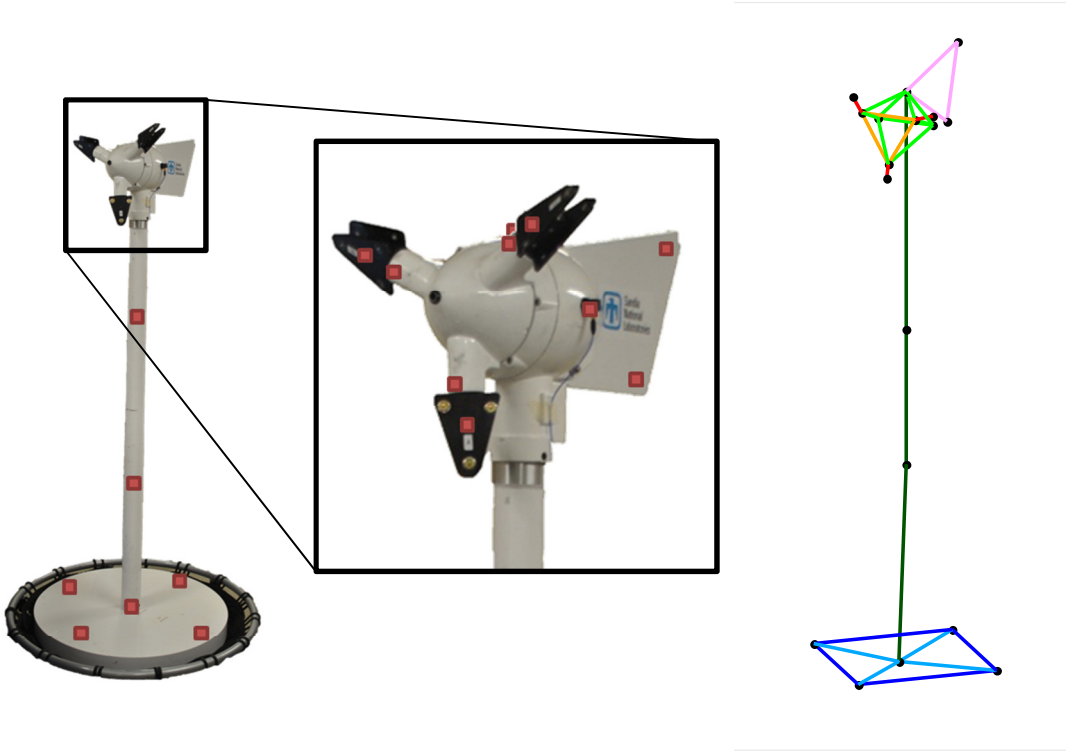

Figure 2.2.3: Instrumentation locations for the tower substructure.

The tower structure rests upon a commercial trampoline. Previous work [6] has shown that the lowest elastic modes near 20 Hz are only about 5 times higher in frequency than the highest rigid body modes near 4 Hz, whereas the desired ratio is typically 10 times or more.

Therefore, considering this system to be a ‘free-free’ approximation may not be an adequate assumption. This was not considered in the first test on the turbine. Also, precise mass properties for this structure, from which properly-scaled rigid body modes could be reconstructed, were not known. The mass properties from the first test could have been used, but since that test was unsuccessful, it was not clear how good the mass properties derived from those models were. In many studies it has been seen that properly-scaled rigid body modes play an integral part in substructuring calculations [10],[11]. For these reasons, the rigid body modes of the structure were measured experimentally in a separate test.

The rigid body modes were excited via a swept-sine shaker input to the base and tower of the structure (Figure 2.2.4). From these inputs, all six rigid body modes could be excited. Since the frequencies were on the order of just a few Hz, the test was operating on the lower end of the accelerometers’ sensitivity. This led to mode shapes which were slightly noisy. To average out these small errors, rigid body modes were constructed from the three principal rotations and three principal translations and then fit to the experimental data in a least-squares fashion. This effort gave smooth, scaled rigid body shapes that matched the frequencies from [6] well. These modes were appended to the elastic modes from the impact test to derive a full modal model of the tower.

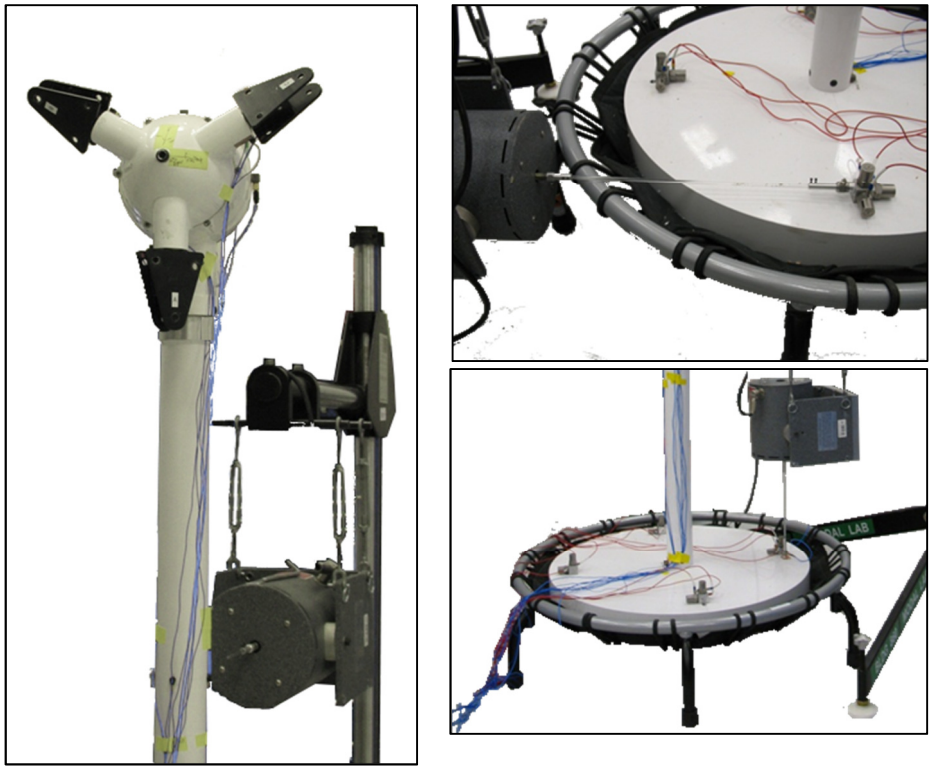

Figure 2.2.4: Drive points to excite rigid body modes: Tower for pitching and rolling modes (left) and base for yawing (top right) and y-direction bounce (bottom right).

2.2.2.2. Results

Six rigid body modes and seven elastic modes were extracted from the data in the test range. The natural frequencies and damping ratios for each mode are shown in Table 2.2.1. Mode shapes are displayed in Appendix B.

Mode	Frequency (Hz)	Damping Ratio (%)	Description
1	0.89	1.62	z-direction Translation
2	0.95	3.64	x-direction Translation
3	2.83	8.24	y-direction Translation
4	3.04	2.90	Yaw Mode
5	3.25	6.57	Pitch Mode
6	3.93	6.69	Roll Mode
7	20.53	1.01	1st Bending in yz-plane
8	20.55	0.95	1st Bending in xy-plane
9	46.84	0.25	Pole Torsion Mode
10	73.89	0.70	2nd Bending in yz-plane
11	84.59	0.70	2nd Bending in xy-plane
12	96.75	0.30	Tail Flapping Mode
13	148.87	1.50	Generator Shaft Torsion

Table 2.2.1: List of extracted modes from the tower test.

The analytical model was a good fit to the experimental data. This can be attributed to the simplicity of the turbine tower system, which resembles a beam with large masses on both ends. Good data was generally taken from impacting the pole and transmission simulator. Data from tail impacts tended to not look as good. Since the tail is quite soft compared to the rest of the system, an adequate force level on the tail would result in large deformations, which resulted in slightly nonlinear behavior. Additionally, this large displacement made it difficult to impact the structure without double hits. Complex mode indicator functions (CMIFs) from pole and tail impacts are shown in Figure 2.2.5.

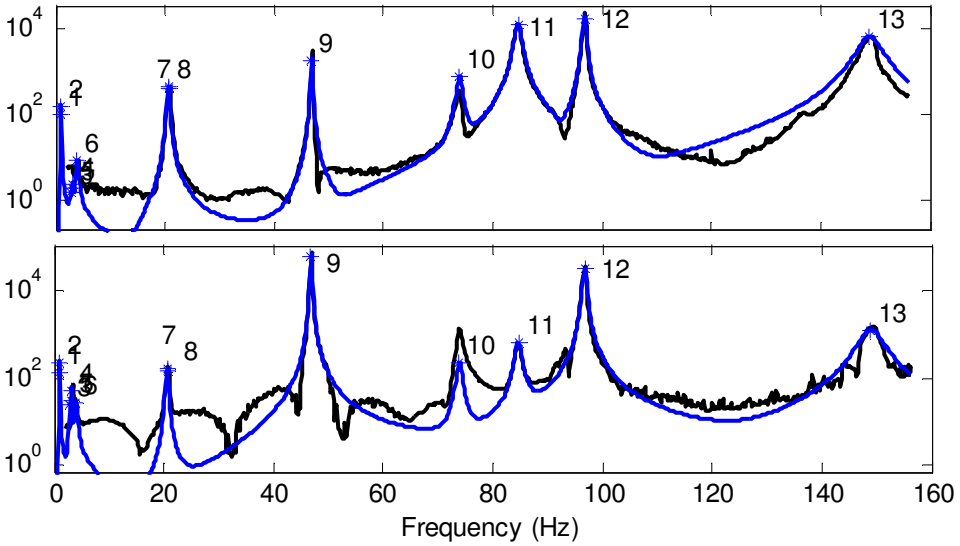

Figure 2.2.5: CMIFs from a tower reference (top) and the tail reference (bottom). Experimental data is shown in black, and the analytical fit is shown in blue.

2.2.3. Hub and Blades Test

2.2.3.1. Test Setup

For the hub and blade structure, the transmission simulator was instrumented identically as for the tower structure test. Each blade was instrumented with two triaxial accelerometers to identify first and second bending and edgewise modes. Torsion modes would not be easily identifiable in this configuration; however, recent tests on the blades [8] suggest that these modes will be out of the frequency range of interest. The accelerometer locations and a line model are shown in Figure 2.2.6.

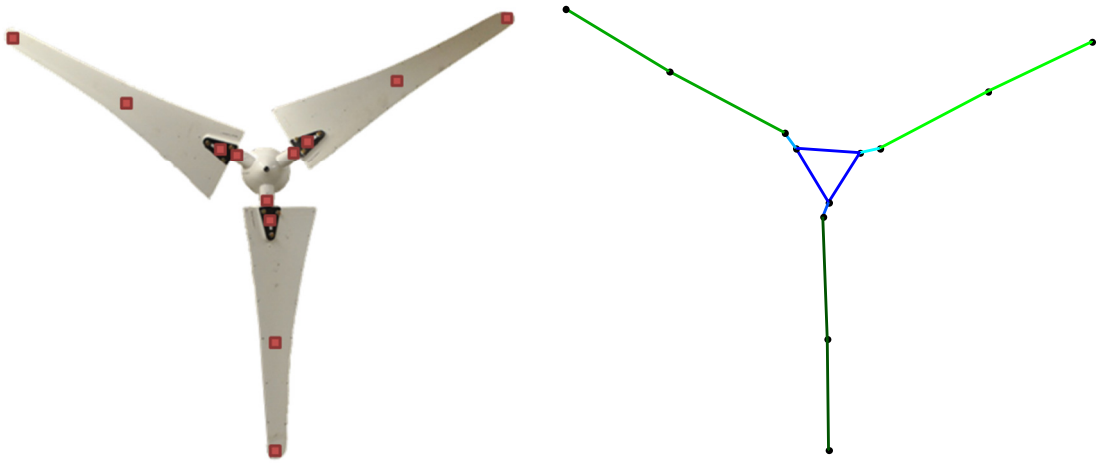

Figure 2.2.6: Instrumentation locations for the Hub and Blades

The structure was excited at drive points on the transmission simulator and near the midpoint of the blade. The blade tips did not work well as a drive point as the large deflection of the blade tip made it difficult not to double-hit the structure.

Because the hub was supported on soft springs, the rigid body modes were too low in frequency to measure via modal test with the current setup. The rigid body modes of the system needed to be constructed from mass properties. Mass properties from the hub were measured experimentally on a Space Electronics mass properties machine, and mass properties for the three blades were estimated from a new CAD geometry presented in [12]. Three blades were arranged as they would be in the assembly, and mass properties were calculated by the Solidworks modeling software shown in Figure 2.2.7. It was assumed that the blade's base (highlighted in blue in Figure 2.2.7) and the blade's span (shown in gray in Figure 2.2.7) had unique but uniform densities, and each density was tuned so that the total mass and center of gravity along the span were consistent with a simple balancing experiment. The calculated densities of each portion of the blade are given in Table 2.2.2.

Blade Span	940.5 kg/m^3
Blade Base	2664.5 kg/m^3

Table 2.2.2: Blade approximate densities.

The mass properties of the blades and the hub were combined using the parallel axis theorem. Rigid body modes shapes were created from the three principal translations and rotations, and scaled using the calculated mass properties.

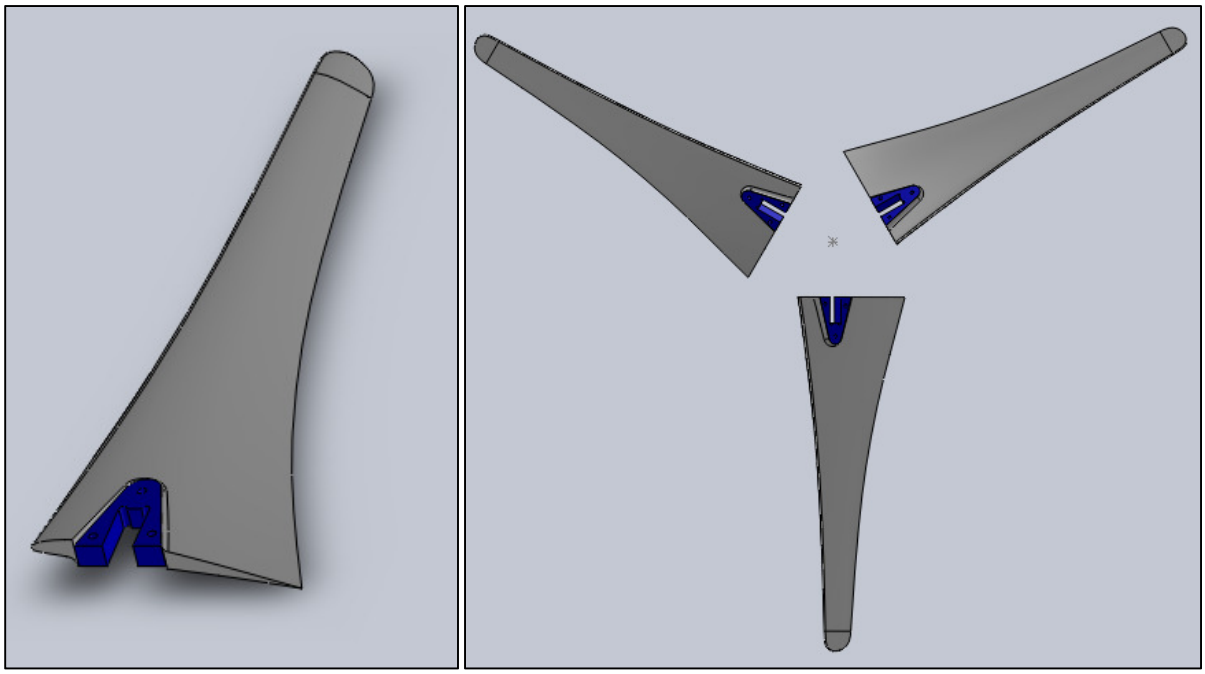

Figure 2.2.7: Blade solid models based on measured blade geometry.

Property	Hub	Three Blades	Entire Rotor
Mass	3.6 kg	2.6 kg	6.2 kg
$c_{g,z}$	-0.0615 m	-0.0673 m	-0.0637 m
I_{xx}	0.0150 kg-m^2	0.189 kg-m^2	0.204 kg-m^2
I_{yy}	0.0148 kg-m^2	0.189 kg-m^2	0.204 kg-m^2
I_{zz}	0.0276 kg-m^2	0.3769 kg-m^2	0.405 kg-m^2

Table 2.2.3: Mass Properties. Moments of inertia are measured from the center of mass of each object. Since all have rotational symmetry about z, all cross products of inertia are zero, and all c_g lie on the z-axis.

2.2.3.2. Results

The six analytically generated rigid body modes were combined with nine elastic modes extracted from the impact tests. These modes are enumerated in Table 2.2.4. Mode shapes from the test are displayed in Appendix B.

Mode	Frequency (Hz)	Damping Ratio (%)	Description
1	0.1 *	0	x-direction Translation
2	0.1 *	0	y-direction Translation
3	0.1 *	0	z-direction Translation
4	0.1 *	0	Rigid Body Yaw
5	0.1 *	0	Rigid Body Pitch
6	0.1 *	0	Rigid Body Roll
7	20.36	2.17	1st Bending, 3 Blades in Phase
8	27.27	1.75	1st Bending, 1 Blade out of Phase
9	28.97	1.84	1st Bending, 1 Blade out of Phase
10	53.19	3.27	2 Blade Edgewise Mode
11	62.14	1.81	2 Blade Edgewise Mode
12	68.38	1.76	2nd Bending, 3 Blades in Phase
13	95.31	2.14	2nd Bending, 1 Blade out of Phase
14	100.05	1.50	2nd Bending, 1 Blade out of Phase
15	153.09	2.49	3 Blade Edgewise Mode

Table 2.2.4: List of extracted modes from Blade and Hub test. (*) Note that the rigid body modes were given small positive frequencies to ensure that no negative mass or stiffness developed from the subtraction.

Due to the nature of the connections of this substructure, it behaved less linearly than the tower structure tested previously. The blades are attached to the hub via features that clamp the blade when tightened. These joints, relying primarily on friction, will slip if a large enough excitation is applied. Similar to the tower, when the structure was excited on the stiffer transmission simulator, the smaller response gave more linear results. Exciting at the

blades' midspan gave strong bending responses, but apparently more nonlinear response. The focus here was to fit the strongest resonances below 100 Hz (see Figure 2.2.8).

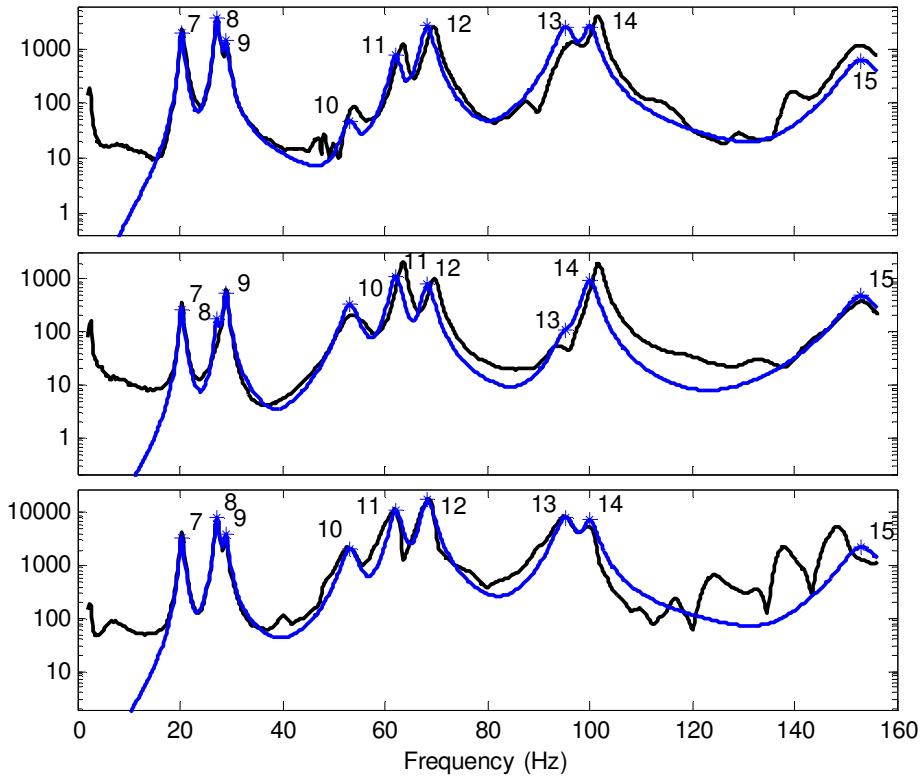

Figure 2.2.8: CMIFs of the Blade and Hub structure. References from top to bottom: z-direction on Transmission Simulator; y-direction on Transmission Simulator, edgewise modes are excited better; z-direction on blade, strong bending excitation, but nonlinear effects in high frequency range. Experimental data is black and the analytical fit is blue.

2.2.4. Substructuring Methodology

For this experiment, the transmission simulator contained 15 degrees of freedom, 5 on each blade anchor. Through a quick tap test, it was found that the first elastic mode of the transmission simulator had a natural frequency near 1200 Hz, which was far above the

frequency range of the test. Therefore, the transmission simulator was assumed to be rigid over the frequency band of interest. The transmission simulator model used in substructuring calculations contained only 6 rigid body modes—the three principal translations and rotations—created from the measured mass properties of the hub shown in Table 2.2.3.

The substructuring calculations then proceed. For the following, the subscript T represents the tower-and-hub structure; the subscript B represents the blades-and-hub structure; and the subscript TS represents the transmission simulator structure (hub).

$$\begin{bmatrix} \mathbf{I}_T & & 0 \\ & \mathbf{I}_B & \\ 0 & & -\mathbf{I}_{TS} \end{bmatrix} \begin{Bmatrix} \ddot{\mathbf{q}}_T \\ \ddot{\mathbf{q}}_B \\ \ddot{\mathbf{q}}_{TS} \end{Bmatrix}$$
$$+ \begin{bmatrix} \begin{bmatrix} \ddots & \\ & 2\zeta_T\omega_T \end{bmatrix} & & 0 \\ & \begin{bmatrix} \ddots & \\ & 2\zeta_B\omega_B \end{bmatrix} & \\ 0 & & -\begin{bmatrix} \ddots & \\ & 2\zeta_{TS}\omega_{TS} \end{bmatrix} \end{bmatrix} \begin{Bmatrix} \dot{\mathbf{q}}_T \\ \dot{\mathbf{q}}_B \\ \dot{\mathbf{q}}_{TS} \end{Bmatrix} \qquad (2.2.1)$$
$$+ \begin{bmatrix} \begin{bmatrix} \ddots & \\ & \omega_T^2 \end{bmatrix} & & 0 \\ & \begin{bmatrix} \ddots & \\ & \omega_B^2 \end{bmatrix} & \\ 0 & & -\begin{bmatrix} \ddots & \\ & \omega_{TS}^2 \end{bmatrix} \end{bmatrix} \begin{Bmatrix} \mathbf{q}_T \\ \mathbf{q}_B \\ \mathbf{q}_{TS} \end{Bmatrix} = \begin{Bmatrix} \boldsymbol{\Phi}_T^T \mathbf{F}_T \\ \boldsymbol{\Phi}_B^T \mathbf{F}_B \\ \boldsymbol{\Phi}_{TS}^T \mathbf{F}_{TS} \end{Bmatrix}$$

For this substructuring attempt, unlike the previous try, modal constraints will be used for both the subtraction of the transmission simulator and the coupling of the bladed hub to the tower. The modal constraints will be applied to the subset of degrees of freedom measured on the transmission simulator (i.e. the red squares on the hub in Figure 2.2.3 and Figure 2.2.6) again denoted by the subscript m. The constraint is illustrated in Figure 2.2.9.

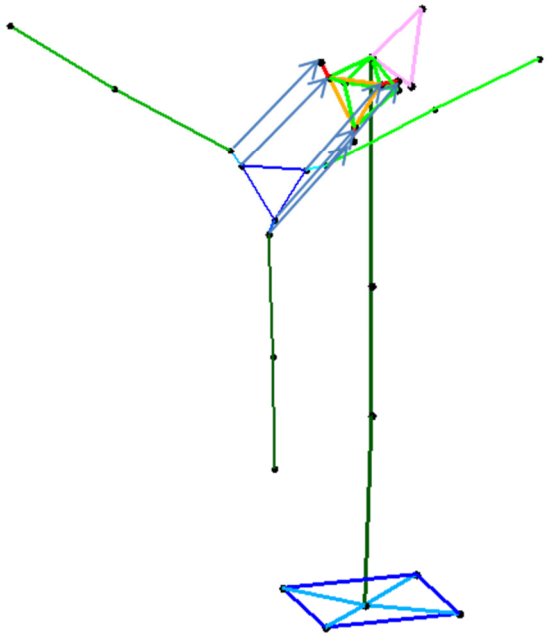

Figure 2.2.9: All measured points on the transmission simulator are used to formulate the least-squares constraint.

Like the first substructuring attempt, both substructures are constrained to the transmission simulator, as opposed to one another. The constraint equations look like

$$\begin{bmatrix} \boldsymbol{\Phi}_{TS,m}^{+}\boldsymbol{\Phi}_{T,m} & \mathbf{0} & -\mathbf{I} \\ \mathbf{0} & \boldsymbol{\Phi}_{TS,m}^{+}\boldsymbol{\Phi}_{B,m} & -\mathbf{I} \end{bmatrix} \begin{Bmatrix} \mathbf{q}_T \\ \mathbf{q}_B \\ \mathbf{q}_{TS} \end{Bmatrix} = \mathbf{B}\mathbf{q} = \mathbf{0} \qquad (2.2.2)$$

with which the remainder of the substructuring calculations can be performed (equations (1.1.5) through (1.1.7)). In this case, the 15 degrees of freedom on the transmission simulator are constrained in a least-squares sense by the 6 rigid body modes of the transmission simulator. This averages out the error in the experimental substructures.

2.2.5. Substructuring Results

Coupling the systems together as described in the previous section, a full turbine model is derived. This substructured model is now compared to the results from the truth test on the entire turbine. This truth test used accelerometers in exactly the same locations as on the substructures, allowing a point-by-point comparison of the substructured turbine and the measured turbine.

Substructured modes were again correlated to truth modes, but the method was varied slightly. Instead of sorting purely by MAC, a frequency-based weighting was also incorporated. In [10] it was seen that erroneous high frequency mode shapes or other spurious modes could have a similar shape to correct low frequency modes, so a large frequency error would be found because the MAC selects the wrong mode. By weighting by frequency error as well, this miscorrelation can often times be avoided. This was useful for mode 8 of the truth system in Figure 2.2.10. Based purely on MAC, substructured mode 13 would have been chosen, even though there is a substructured mode with a similar (though slightly worse) MAC near that frequency. The weight W_{ij} between the ith truth mode and the jth substructured mode is

$$W_{ij} = MAC\left(\boldsymbol{\Phi}_{Truth,i}, \boldsymbol{\Phi}_{Substr,j}\right) \cdot \left(1 - F \cdot \left|f_{Truth,i} - f_{Substr,j}\right|\right) \qquad (2.2.3)$$

where F is a weight applied to the frequency error, in this case, $F = 0.025$. The highest weight W_{ij} for the ith truth mode is then said to correspond to that mode. The truth modes and their substructured complements are shown in Table 2.2.5. The MAC between the two systems is shown in Figure 2.2.10.

Truth Mode	Frequency (Hz)	Substr Match	Frequency (Hz)	Error	Truth Damping	Substr Damping	Error	MAC
Mode 1	17.24	Mode 1	17.86	3.58%	1.12%	0.99%	-12.08%	0.92
Mode 2	17.70	Mode 2	18.06	2.05%	0.78%	1.12%	44.53%	0.98
Mode 3	18.71	Mode 3	19.10	2.10%	0.81%	1.24%	52.68%	0.93
Mode 4	20.06	Mode 4	19.85	-1.02%	0.87%	1.32%	51.83%	0.97
Mode 5	21.46	Mode 5	21.21	-1.16%	0.92%	1.22%	32.93%	0.93
Mode 6	30.06	Mode 6	29.66	-1.32%	1.79%	0.44%	-75.37%	0.98
Mode 7	37.31	Mode 7	38.15	2.24%	1.00%	0.77%	-22.71%	0.99
Mode 8	48.38	Mode 8	51.27	5.98%	1.70%	2.65%	56.15%	0.62
Mode 9	54.87	Mode 9	56.92	3.74%	3.15%	1.40%	-55.52%	0.70
Mode 10	60.68	Mode 10	61.50	1.34%	1.96%	1.76%	-10.16%	0.83
Mode 11	66.16	Mode 11	66.31	0.21%	1.47%	1.70%	15.72%	0.72
Mode 12	68.60	Mode 12	75.41	9.93%	0.82%	0.77%	-6.58%	0.59
Mode 13	84.44	Mode 13	88.10	4.33%	0.92%	1.54%	66.43%	0.85
Mode 14	95.26	Mode 14	95.50	0.24%	1.14%	1.24%	9.15%	0.88
Mode 15	106.85	Mode 15	104.62	-2.09%	0.86%	0.92%	6.16%	0.93
Mode 16	121.28	-	-	-	1.15%	-	-	-
Mode 17	140.80	-	-	-	1.19%	-	-	-
Mode 18	149.85	Mode 16	152.36	1.68%	1.44%	2.47%	70.95%	0.83

Table 2.2.5: Substructuring results compared to the truth modes.

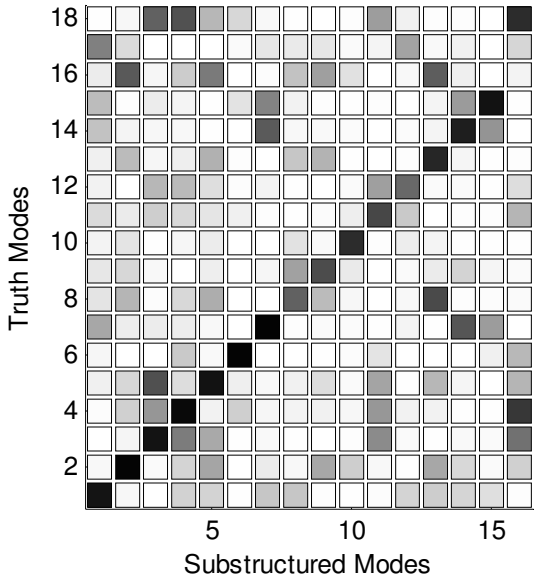

Figure 2.2.10: MAC between Truth and Substructured modes. Black = 1, White = 0.

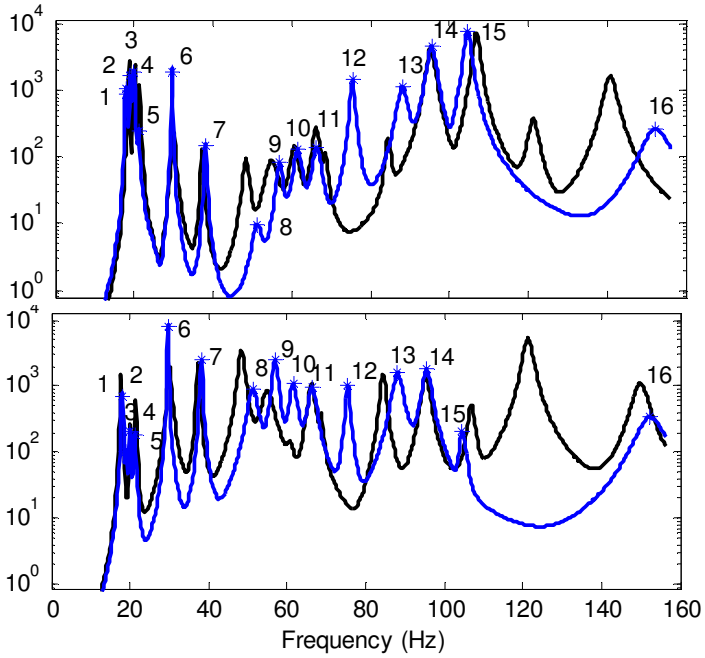

Figure 2.2.11: CMIFs from an *x*-direction tower reference (top) and a reference on the transmission simulator (bottom). Substructuring predictions are shown in blue.

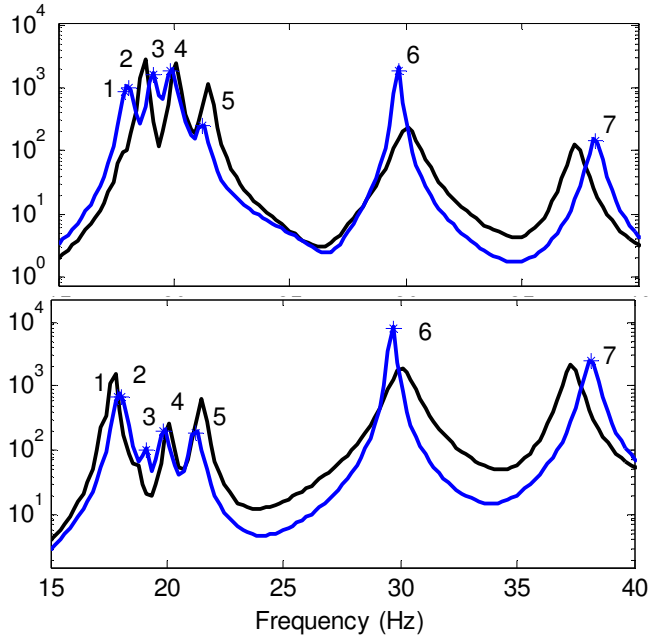

Figure 2.2.12: Zoom of Figure 2.2.11 showing the tight grouping of modes near 20 Hz. The CMIFs show an *x*-direction pole reference (top) and transmission simulator reference (bottom). Substructuring predictions are shown in blue.

Looking at Table 2.2.5, several trends are clear. The frequencies of the majority of the substructured modes are close to the truth model, within 5% error. Two notable examples are modes 8 and 12, each of which contributes significant error to the CMIFs in Figure 2.2.11. Mode 12 is significantly high and appears well separated from mode 11 in the substructured model, whereas it is very close to mode 11 in the truth model. Overall, the frequencies are accurate out to about 100 Hz. Above this range two high frequency truth modes at 121 Hz and 141 Hz were missed by the substructuring calculations. This can be seen clearly in the MAC of Figure 2.2.10 as the rows of the matrix that have low correlation to any of the columns. However, it is expected that the fidelity of the model would fall off in this range.

A comparison of the mode shapes shows good agreement as well. Over the majority of the frequency range, the MAC between the truth model and the substructured model is high. Even when the value of the MAC is low, the mode shapes bear a visual resemblance. Errors in the mode shapes yield scaling errors in the CMIFs of Figure 2.2.11, which are more pronounced in the region between 40 and 80 Hz, where the MACs tend to be low. These worst mode shapes are shown in Figure 2.2.14, compared to good mode shapes in Figure 2.2.13.

The substructured damping ratios are on the same order of magnitude as the measured damping ratios, but they are as much as 75% off. The effects of this can be seen in the CMIFs of Figure 2.2.12; mode 6 of the substructured model is significantly less damped than the corresponding measured model. There is a significant difference in the height of the two peaks even though the mode shapes are scaled similarly. Overall the damping ratios were worst aspect of the comparison, and were not predicted well at all. The turbine consists of

many bolted joints and press fits. Notably, the blades are held in place primarily by the friction generated by the two sides of the black clamp. The hub is also pressed onto the mock generator shaft. These joints are likely not modeled well by the viscous damping assumed in these calculations, so it is reasonable that these values would be in error.

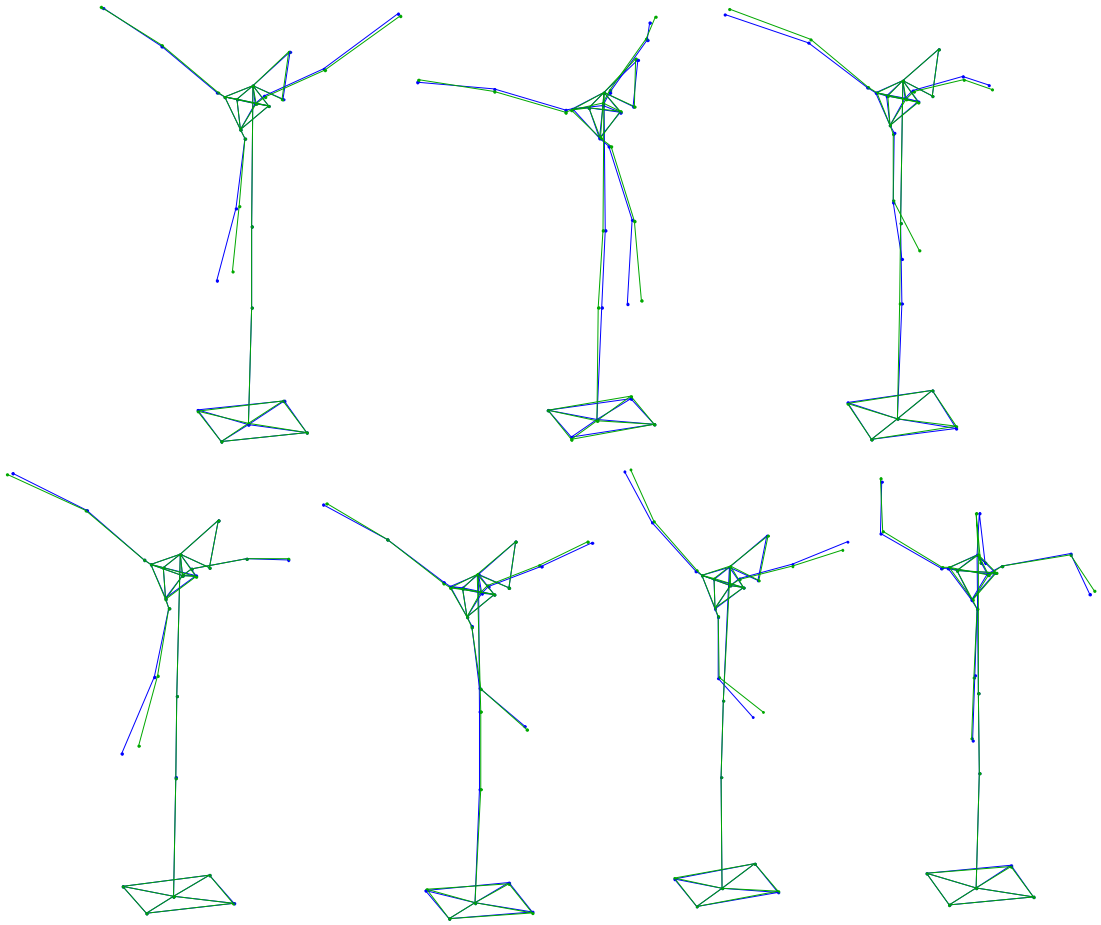

Figure 2.2.13: Mode shapes with high MAC between substructured and truth data. From top left to bottom right, elastic modes 1 through 7.

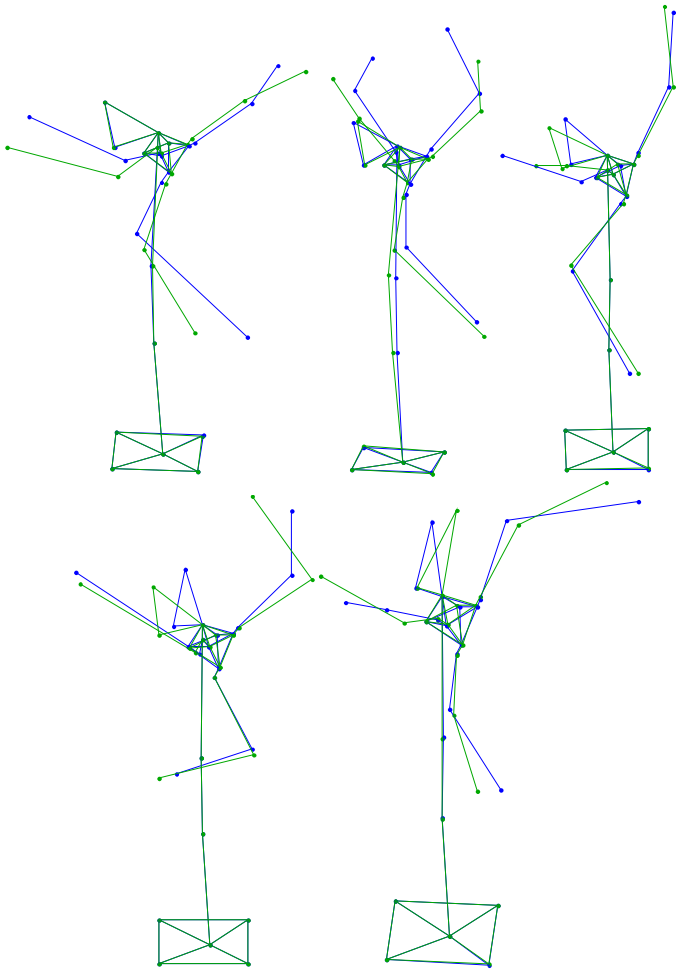

Figure 2.2.14: From top left to bottom right, elastic modes 8 through 12. These shapes had the worst correlation to the truth data. Truth data is shown in blue with substructured data overlaid in green.

2.2.6. Possible Error Sources

Although the results for most modes are quite good, there is still up to 10% error in the frequencies of the system and MACs as low as 0.6. There is always the potential that these differences are due to nonlinearities of the system. It was seen that for both the blades and the tower substructures that the magnitude of displacement could shift the frequencies of the system (note the peaks in Figure 2.2.5 and Figure 2.2.8). For this reason, modal data taken

from ‘soft’ drive points was viewed with suspicion, and often a different drive point would be selected to extract the mode as it was typically more linear. Nonlinearities could certainly cause the assembled system to behave slightly differently than a combination of the two substructures—for an equal force input, the deflections will be slightly different. Several other possible sources of error are considered here.

2.2.6.1. Accelerometer Mounting

Great care was taken in mounting the accelerometers so that they would be consistent throughout all the different measurements. Accelerometers were left in place between tests to ensure consistent mass-loading and orientation between tests. This should not be a significant source of error.

2.2.6.2. Rigid Body Mode Shape Scaling

Initially this effort utilized a very rough blade approximation as a triangular plate to estimate mass properties. It was seen that in this case, the first few elastic modes of the substructuring calculation were up to 15% off the truth data, which led to the creation of the more refined model appearing in this paper. To further investigate other modes that may be sensitive to the error, a brief sensitivity study was performed, which consisted of scaling the rotational inertia of the blades, and watching how the natural frequencies of each mode varied. The results are shown in Figure 2.2.15. Not surprisingly, the lower modes were more strongly affected by the moment of inertia. This agrees with an example in [13] where the low frequency modes contain large contributions from the rigid body mode shapes of the individual substructures. There are also three distinct peaks at modes 6, 9, and 12. These modes show a high sensitivity to scaling the blades’ inertia properties. It would seem that the majority of the

sensitive natural frequencies were accurate in this study, which suggests that the mass properties used in the calculation are accurate.

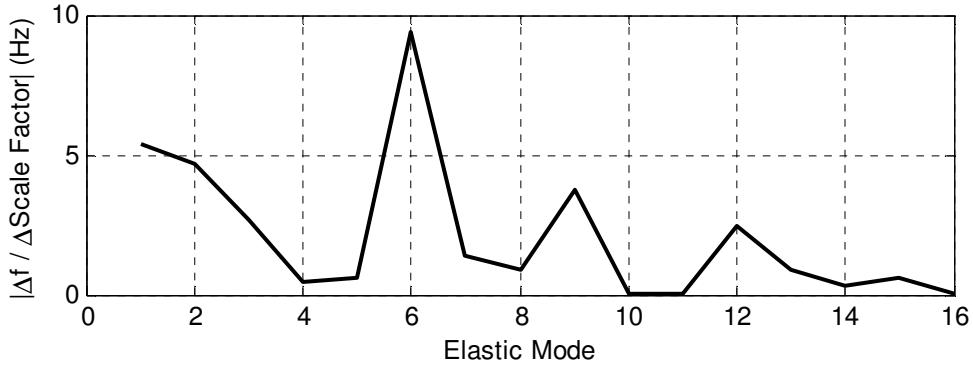

Figure 2.2.15: Sensitivity in the elastic modes' natural frequencies to scaling the blades' rotational inertia.

2.2.6.3. Modal Truncation

The frequency of interest of the test was up to approximately 100 Hz, so the test proceeded up to 156 Hz to try to capture some of the modes above the frequency band to include in substructuring calculations. However, in this extra range only one mode was found in each subsystem that could be reasonably extracted. It is reasonable that the substructured model should not be accurate above that frequency range if each substructure only contains one mode, though this will largely be problem dependent.

2.2.6.4. Constraint Satisfaction

One additional source for potential error which is unique to the transmission simulator method is the satisfaction of the constraint equations. In the transmission simulator method, these constraints are softened, and satisfied in a least-squares fashion. In this specific

example, the transmission simulator was assumed to be rigid in the frequency band of interest, since its first mode is near 1200 Hz. If the constraints are satisfied perfectly, the three transmission simulator models (one negative model and one from each substructure) will be moving in unison. Selected mode shapes of the substructured system are shown in Figure 2.2.16. The discrepancies in motion are obviously small compared to the overall motion of each mode shape, so there should not be significant error from the constraints.

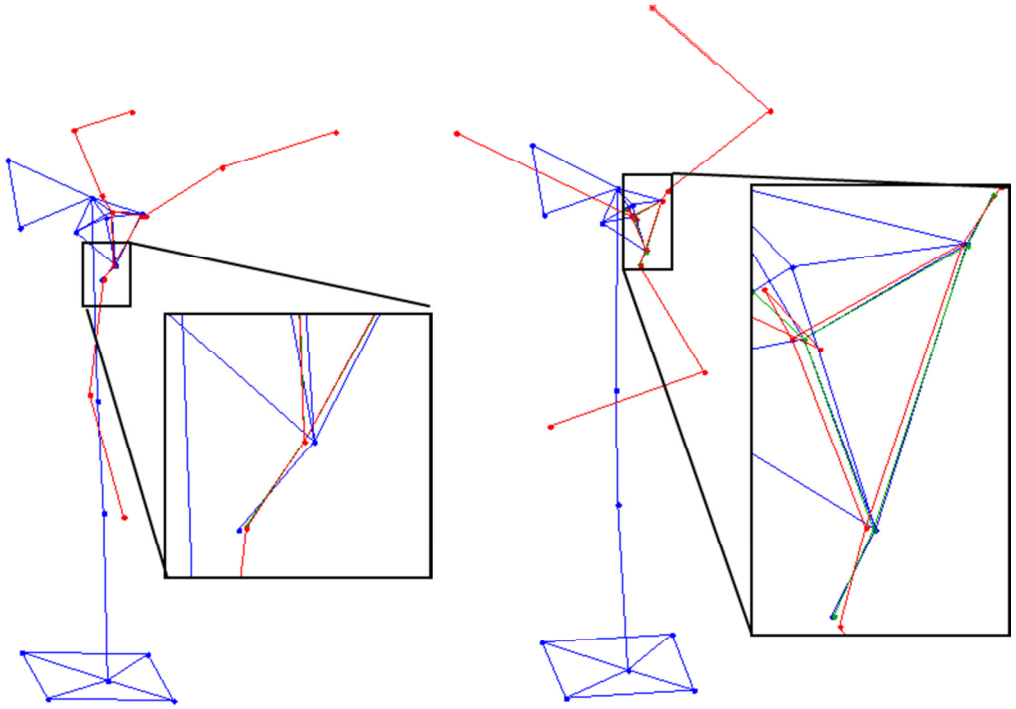

Figure 2.2.16: Selected mode shapes showing small errors in the transmission simulator constraints. Degrees of freedom are colored according to their original substructure. Blue: Tower, Red: Blades, Green: Transmission Simulator. Elastic modes 6 and 11 are shown.

2.3. Comparison between the Two Tests

Both wind turbine substructuring efforts attempted to substructure different components of the Ampair 600 Wind Turbine to accurately characterize the built up system. In the first attempt a blade was removed and then reconnected using substructuring techniques. In this attempt a transmission simulator was created to imitate the clamped joint, which mass-loaded the blade interface. In the second attempt, the entire hub (including blades) was removed from the nacelle to create one substructure, and it was also left on the tower (without blades) for the tower test. The transmission simulator for this test was simply the hub, which appears in both substructures. The hub obviously imitates the joint very well, since it is the joint that is used in the final system.

Though both substructuring techniques used the transmission simulator method to couple similar structures to form the same built-up structure, several differences exist between the attempts.

2.3.1. Excitation and Acquisition

Though both tests were multiple-input, multiple-output (MIMO) tests, the initial substructuring attempt had many more inputs than outputs (due to a limited number of test channels available), whereas the second test had many more accelerometers than input locations. The first test more closely represented a multiple-input, single-output (MISO) test and the second more closely represented a single-input, multiple-output (SIMO) test. Though both tests are equally valid theoretically, in practice the SIMO test was found to be more practical in getting good data.

The testing period for the MISO test was much longer, since the force inputs had to be applied successively, but in a SIMO test the accelerometers measure simultaneously. Since the relative time spent testing during a SIMO test is small, it is easy to perform testing iterations in which different aspects of a test (applying an exponential window, for example) can be changed. For the MISO tests performed here, where the testing for each component could last a few hours, it was less easy to go back and take new data, especially when dealing with time constraints imposed due to the shared nature of the turbine. Although both tests place in the span of approximately two weeks, only one iteration of data collection occurred in the first attempt, whereas every test in the second attempt had multiple iterations. Hammer inputs are also decidedly less consistent than an accelerometer measurement, which when glued to the structure always measures the motion of the same location and orientation with considerable accuracy.

2.3.2. Constraints

In the first test, point constraints were used to couple the substructures together. Even though the constraints acted on the transmission simulator which moved rigidly, experimental error still existed in the two-bladed turbine substructure. An error in one of the point constraint degrees of freedom could have a large impact on the results of the substructuring calculation. Even if the modal constraints had been used in this case, the average would still have been performed over only nine degrees of freedom relatively close together in space; small translational errors could result in large rotation errors. Using the bolts as impact points on which to apply constraints, though intuitive, was not particularly robust. One can imagine that impacting a bolt may cause slipping, which would make the behavior of these points

nonlinear and soft. Instead of measuring the deformation of the clamp holding the bolt, the movement of the bolt is measured instead.

The constraints of the second attempt were more able to average out experimental errors, since both structures were attached to the transmission simulator through least squares constraints. All impacts took place on solid portions of the turbine that shouldn't slip. It is clear from this example that modal constraints allow the analyst to avoid measuring the connection points directly (no shafts or bolts were instrumented), which were difficult to measure accurately in the first test.

2.3.3. Rigid Body Mode Accuracy

Between the first and second tests, a lot of work was done characterizing the blades' geometry. The Atomic Weapons Establishment (AWE) performed a laser scan [12] which accurately measured the geometry. Using this model, more robust rigid body mode shapes could be generated. A comparison between mass properties is shown in Table 2.3.1. The brief sensitivity study performed in Section 2.2.6.2 suggests that the mode shapes are scaled correctly in the second test. The differences in the mass properties are approximately 10% for the principal inertia values. Products of inertia have larger errors but they are much smaller than the principal inertia values.

When constructing rigid body modes, translations applied to each point are dependent on that point's location and orientation. If this is not precisely known, the constructed rigid body modes will be in error. The higher fidelity AWE model also helped to precisely determine accelerometer orientation so accurate rigid body motion could be assigned to each point.

Property	Rough Blade Geometry	AWE Blade Geometry	Difference
m	0.935	0.864	-8.32%
cg_y	0.554	0.552	-0.50%
I_{xx}	0.314	0.292	-7.50%
I_{xy}	-0.00266	-0.00547	51.26%
I_{xz}	-0.0000366	0.000279	113.13%
I_{yy}	0.00156	0.00170	8.36%
I_{yz}	0.000250	0.00310	91.94%
I_{zz}	0.316	0.294	-7.50%

Table 2.3.1: Differences in mass properties between the two blade models. Note that both are approximate mass properties based off solid model properties. Properties are measured about the coordinate system at the tip of the blade, as shown in Figure 2.3.1. The largest errors were see in the cross-products of inertia, but these were small compared to the principal values.

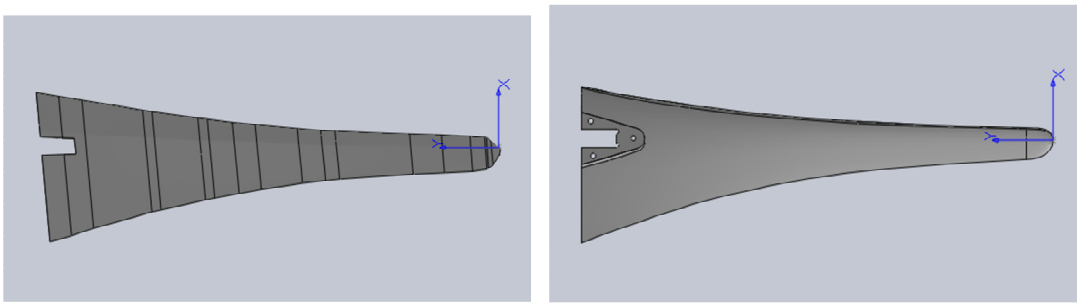

Figure 2.3.1: Blade geometries from the first substructuring attempt (left) and the second substructuring attempt (right).

The extent of which each of these differences contributed to poor substructuring results is unknown; it has been seen that seemingly insignificant errors in a test can cause drastic errors in substructuring predictions [14]. It is hard to identify potential issues in substructured models, so this provides motivation for creating the validation method that will be presented in Section 3.

3. Investigation of a Substructuring Validation Experiment

In the previous section, two substructuring attempts were performed, but only one was successful. It was easy to determine which was successful and which was not, since a full truth test could be performed on the built-up system. However, this is not always practical, for many reasons. For example, if the built-up structure is very large, then it may be hard to assemble for a test. Also, subcomponents that come from different vendors may be unavailable so the structure cannot be assembled. Some systems, such as satellites, will have different operating conditions (deployed on orbit) than testing conditions (stowed in launch configuration). Finally, it may be impossible to adequately instrument the truth test due to enclosures that become inaccessible when the system is assembled. But, even in these situations where a truth test is impractical, an analyst would still like some measurement of the fidelity of an experimental substructure model.

To accomplish this, a validation test is proposed. Allen and Kammer [14] proposed a validation procedure to investigate the adequacy of the modal basis used in substructuring calculations. In this procedure, a fixture is attached to the experimental substructure, and an additional modal test is performed to characterize the fixture/substructure assembly. Meanwhile, an analytical model of the validation fixture is coupled to the experimentally derived model of the substructure. The correlation between the test and the prediction using the experimentally derived subcomponent model is then assessed to obtain confidence in the experimental model of the substructure or reveal its deficiencies. In their paper, Allen and Kammer primarily focus on the issues surrounding modal truncation. This effort expands on

that work and addresses measurement uncertainty, specifically with regards to errors in the measured mode shapes.

The goal of a validation test is to infer whether the substructure model is adequate to provide accurate predictions in the application of interest. Typically this assembly cannot be tested or modeled analytically, so the substructuring predictions must be used to optimize the design or predict the structure's life. However, in this effort, the application of interest will be treated as known so the validation procedure can be evaluated. The validation procedure is deemed effective if the comparison between the validation test and prediction reflects the accuracy of the simulated application of interest.

3.1. Validation Experiment

To perform a validation experiment, one would first derive an experimentally-based substructure model using the transmission simulator method (Figure 3.1.1).

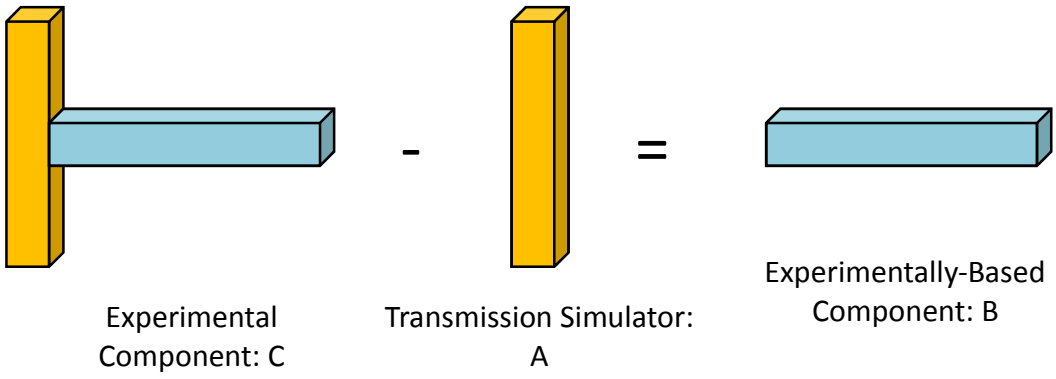

Figure 3.1.1: Schematic of the transmission simulator method for obtaining a modal model of a subcomponent of interest (component B).

Once the substructured model (system B from Figure 3.1.1) is has been obtained, a validation experiment is performed in which an easily-characterized structure is attached at the substructure's interface. The assembly is denoted system E in this study. The modal test on the actual assembly E produces a truth model, designated E_t. The natural frequencies and mode shapes obtained for E_t are then compared to the properties predicted by substructuring calculations using an analytical model of the validation fixture D. This assembly shall be denoted E_{sub}. The comparison between the modal parameters of E_t and E_{sub} provides a measure of the validity of the substructure model. The key assumption of this method, which will be evaluated here, is that if the substructure model is accurate, it should be accurate in both the validation test and the application of interest. A schematic of the validation experiment is shown in Figure 3.1.2.

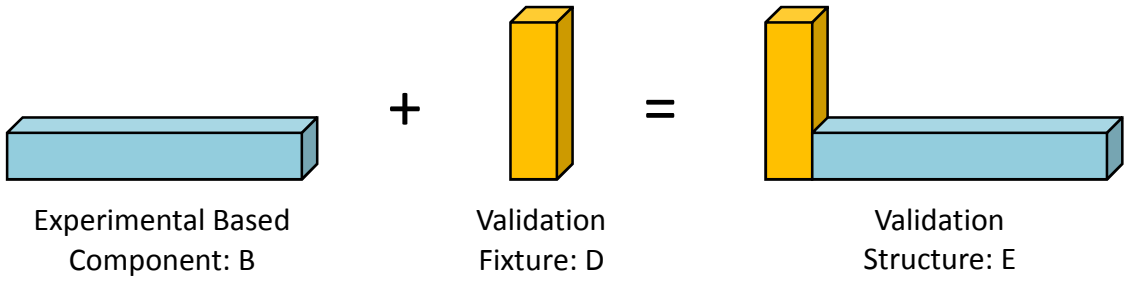

Figure 3.1.2: Schematic of the validation experiment. The validation fixture D is attached to the interface of component B.

3.2. Application of Interest

The substructure model is presumably desired to characterize the response of some assembly. Hence, the experimental model would next be joined to a more complicated structure and its modes would be found. For the purposes of this study, the assembly of interest is the system shown in Figure 3.2.1.

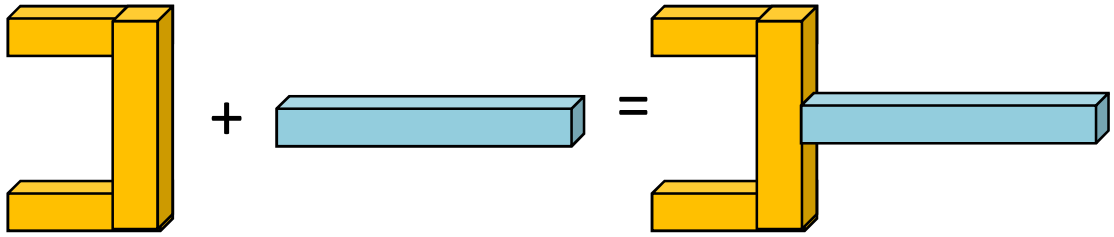

Figure 3.2.1: Schematic of the desired application.

3.3. Error Modeling

Since this paper seeks to investigate the effect of error on the validation experiments, error models will need to be developed. There are innumerable types of errors that may contaminate the results of a modal test. Several works have been presented which investigate the cause of errors in experiments [1],[13],[15], but no work was found which provided a definitive, general purpose model for the expected uncertainty in the natural frequencies, damping ratios, and mode shapes obtained from a modal test. Since a universally accepted noise model is not available, this work proposes three simple models that capture different ways in which noise might affect a measurement. In the following equations, $\mathbf{\Phi}_n$ are the noisy mode shapes of C, $\mathbf{\Phi}$ are the 'clean' mode shapes of C, and $\mathbf{N}$ is a matrix of the appropriate size containing normally-distributed random numbers of mean $\mu = 1$ and standard deviation σ. The natural frequencies are taken to be exact, since their uncertainty is known to be smaller than the uncertainties in the measured mode shapes.

The first noise model is a simple multiplicative model represented in equation (3.3.1). In this case, each degree of freedom in each mode is multiplied by a random number with mean 1 and standard deviation σ. This model produces noise-contaminated mode shapes that have

about the same percentage error whether the shape is large or small at a given point. This model reflects the fact that vibration measurements tend to have a large dynamic range so that measurements in certain frequency bands can often be accurate even when their levels are far lower than the dominant response. Errors due to electrical noise or analog-to-digital conversion have an additive, rather than multiplicative effect, suggesting the use of an additive noise model. However, with modern data acquisition equipment (e.g. 24 bit analog-to-digital converters) these effects tend to be small and hence an additive model of an appropriate level tends to have a negligible effect on the measurements, while an additive model with large noise tends to produce simulated measurements that are dramatically different from what is obtained in the laboratory (see, e.g. [7]). Here the noise matrix, **N**, has the size $N_{DOF} \times N_{modes}$, which is the same size as the mode shape matrix. The noise contaminated mode shape of the rth mode at the ith point is

$$\boldsymbol{\Phi}_{n,ir} = \boldsymbol{\Phi}_{ir}\mathbf{N}_{ir} \qquad (3.3.1)$$

The second noise model considered is a mode scale factor (MSF) model. This model is represented in Eq. (3.3.2), where each mode shape is scaled by a random number with mean 1 and standard deviation σ. This model applies the same scaling to each degree of freedom in a particular mode, but each mode has a different scale factor. This model reflects the fact that the overall scaling on measured mode shapes is directly connected to the accuracy with which the modal damping can be extracted. Modal damping ratios are sometimes found to have uncertainties as high as tens of percent, so this may be a dominant source of mode shape error. Here **N** has the size $N_{modes} \times 1$.

$$\boldsymbol{\Phi}_{n,ir} = \boldsymbol{\Phi}_{ir}\mathbf{N}_r \qquad (3.3.2)$$

The final error model considered is a simple Cross-Axis Sensitivity (CAS) model. This model follows similarly to reasoning presented in [16]. It assumes a Single-Input-Multiple-Output (SIMO) test in which two accelerometers are mounted perpendicularly at each measurement location to measure two displacement DOF (since the problem is planar). The accelerometers are assumed to have a slight cross-axis misalignment, but are calibrated correctly for one dimensional motion along their axis of interest. Then the relationship between the measured responses $\{\hat{x}\ \hat{y}\}^T$ and the actual responses $\{x\ y\}^T$ is

$$\begin{Bmatrix}\hat{x}\\ \hat{y}\end{Bmatrix} = \begin{bmatrix}1 & \tan(\alpha)\\ \tan(\beta) & 1\end{bmatrix}\begin{Bmatrix}x\\ y\end{Bmatrix} \quad \text{or} \quad \hat{\mathbf{x}} = \mathbf{S}\mathbf{x} \qquad (3.3.3)$$

where α and β are normally-distributed random misalignment angles of the horizontal (x-direction) and vertical (y-direction) accelerometers. Then for all the DOF in the model, equation (3.3.3) at each of the m measurement points can be combined, forming a transformation matrix between the measured DOF and the actual DOF, or in this case the measured mode shapes and the actual mode shapes:

$$\boldsymbol{\Phi}_n = \begin{bmatrix}\mathbf{S}_1 & 0 & \cdots & 0\\ 0 & \mathbf{S}_2 & \cdots & 0\\ \vdots & \vdots & \ddots & \vdots\\ 0 & 0 & \cdots & \mathbf{S}_m\end{bmatrix}\boldsymbol{\Phi} \qquad (3.3.4)$$

where each $\mathbf{S}_i$ is the 2×2 transformation matrix in equation (3.3.3).

3.4. Procedure

These concepts will be explored using the systems pictured in Figure 3.1.1 though Figure 3.2.1. The dimensions of the beam in system B are 0.35 m (12 in) long, 19 mm (0.75 in) high and 25.4 mm (1.0 in) wide, identical to the system in [14]. The transmission simulator is also identical to what was used in [14], with a length of 0.15 m (6.0 in) and the same cross section as the horizontal beam. All structures were modeled using 2 node beam elements with 3 degrees of freedom (DOF) per node. The transmission simulator (A) had 21 nodes, and the system of interest (B) had 30 nodes. The structures are all linearly elastic with a Young's Modulus of 206 GPa (30 x 10^6 lbf/in^2), Poisson's Ratio of 0.28, and density of 7860 kg/m^3 (0.284 lb/in^3).

Using the transmission simulator method, experimental tests are performed on system C, and then system A is subtracted from C to arrive at system B. For the case presented here, 7 elastic modes are used to model A , which includes up to the third bending mode of A. This was the highest mode that was found to be needed in [3]. A 'perfect' C model was created by coupling the full finite element models of B and A, resulting in a 150 DOF system. The MATLAB eigenvalue solver used in this investigation seemed to be giving erroneous rigid body mode shapes for systems of this size, so the rigid body mode shapes were constructed manually since they are known to contain two modes with pure translation in x and y and one with pure rotation about the center of mass. They were then mass-normalized to ensure proper scaling. This was found to aid the MATLAB the solvers in finding the natural frequencies and mode shapes in subsequent coupling and uncoupling calculations. The 'experimental' tests on C were then simulated using the following conditions:

1. Because rotations are difficult to accurately measure in the laboratory, these degrees of freedom were discarded. Rotational DOF used in the coupling come from the analytical model of the transmission simulator, as was done in [5].

2. The frequency band of interest was taken to be 0 to 15 kHz to mimic a prior study [5]. Hence, the modal test for C was presumed to capture all of the modes out to 20 kHz (a little less than twice the frequency range of interest), for a total of 16 modes, comprised of 3 rigid body and 13 elastic modes.

3. Because experimental measurements always contain a certain level of error, normally-distributed random error was introduced into the mode shapes of each of the modes of C using each of the three error models described in the Error Modeling section.

The validation test was modeled as noise free, so the modes of the validation structure, system E_t (which would normally be obtained in a modal test), were obtained by combining the full finite element model for B with the full model of the validation fixture.

A Monte-Carlo simulation was performed to evaluate the effect of errors in the 'measured' modes of C on the substructuring calculations. The calculations were repeated over 2500 trials with a different realization of the random noise error model in each trial, resulting in 2500 replicates for the modes of the validation structure, system E_{sub}. The results of these Monte-Carlo simulations are presented in the following subsections. For each noise model, the modes of E_{sub} were paired with those from E_t and the errors in their natural frequencies were calculated. The frequencies were evaluated to characterize their distribution and the

sensitivity of each of the modes to the errors was investigated. The process was then repeated with the assembly of interest in place of the validation fixture, to see how well the validation test reflects the application of interest.

3.5. Results

For each set of simulations, the trends of the mode shapes and natural frequencies of the system E_{sub} were investigated. The noise, especially in large standard deviation cases, tended to cause the modes to move around resulting in different orderings as compared to E_t. The Modal Assurance Criterion (MAC) was used to correlate each of the modes of E_{sub} with those of E_t. For each mode in the truth model, the corresponding mode in the noisy model was chosen based on the highest MAC weighted slightly by the error in natural frequency, as was done in previous modal comparisons (Equation (2.2.3)). For example, the MAC between the truth model and the simulated noise-contaminated modes of the assembly are shown in Figure 3.5.1 for two different trials. This automated procedure was necessary to allow 2500 trials to be processed, although in practice the modes would most likely be paired manually receiving more care and attention.

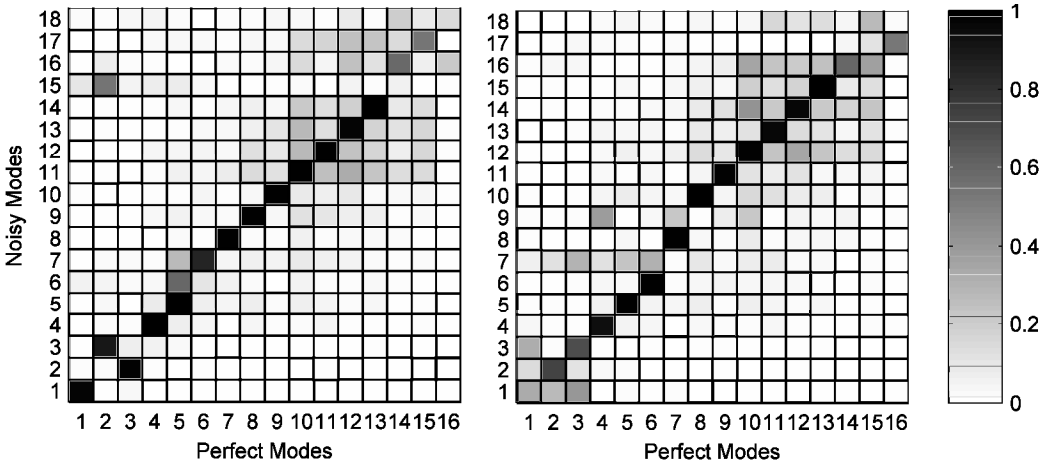

Figure 3.5.1: MAC plots of two trials showing spurious modes occurring at different places in the frequency band. The spurious modes are indicated by the rows of the matrix without a strong correlation to one of the columns.

It was seen in [14] that the subtraction of the transmission simulator from this system leads to the formation of two spurious modes nominally at the 695 and 1037 Hz in the B system. The spurious modes also influence the predictions of the E system's modes and they can be seen in the rows of Figure 3.5.1 that do not have a strong correlation to one of the columns. When noise was added, these modes moved around the frequency band. It was seen that these spurious modes could appear with mode shapes very similar to genuine modes, but with a much smaller scale, and this led to the MAC incorrectly selecting these spurious modes instead of the true ones. Hence, the differences in the natural frequencies were also considered, although with a small weighting relative to the MAC, in the algorithm that paired the modes. Note that the first three modes in both systems are the rigid body modes, and they may not be well characterized by the MAC because any linear combination of the three is also a valid rigid body mode shape.

3.5.1. Natural Frequency Distributions

The natural frequencies for each trial were collected to determine the effect the noise had on the system. For each natural frequency distribution, the sample mean, standard deviation, skew, and kurtosis were calculated. Though the natural frequencies were generated with normally distributed noise on the mode shapes, the distributions of the frequencies showed non-normal characteristics. In general, the distributions showed a higher kurtosis than a normal distribution. The excess kurtosis of the distribution was typically on the order of 10 to 100 (excess kurtosis is zero for a normal distribution). Distributions with a high kurtosis typically have sharper peaks and heavier tails than the normal distribution, or, in other words, there is a high likelihood of obtaining a value close to the mean, but also a higher than expected probability of obtaining outliers. The skew of the distributions were typically quite small, on the order of 10^{-3} or lower.

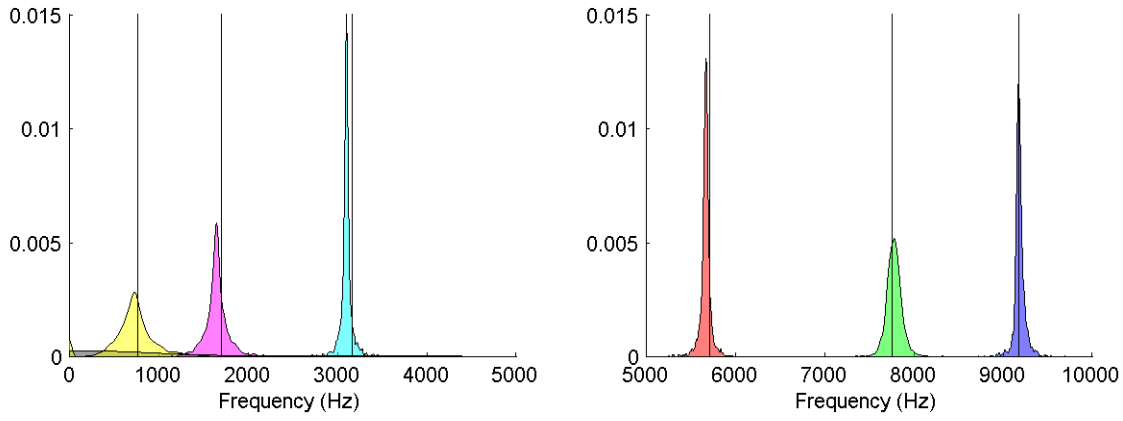

Figure 3.5.2: Sample probability density functions of the natural frequencies of E_{sub}. The distributions typically show larger kurtosis than a normal distribution, and some modes also show a slight skew.

Figure 3.5.2 shows estimates of the probability density functions of the natural frequencies of each of the modes, estimated using the kernel density estimator in [17], for the multiplicative noise model with standard deviation of 5%. This case was representative of the cases studied. For example, the excess kurtosis of the peaks shown in Figure 3.5.2 range from 13 to 173. From these plots it was clear that the modes were not affected equally by the noise. The lower modes are observed to have the widest distribution as a percentage of their mean value.

3.5.2. Modal Scale Factor Error Model

The first error model considered is the scale factor error. The mean and standard deviation of the natural frequencies of E_{sub} are shown in Table 3.5.1 for various levels of noise. Table 3.5.2 shows analogous results for the application of interest. One should note that, for a normally distributed parameter, 95% of the values will fall between ±2 standard deviations and 99.7% will fall within ±3 standard deviations. As observed previously, the natural frequencies are not normally distributed; the sample means and standard deviations listed in the table for each mode are not parameters defining a normal distribution, but are instead simply metrics that describe properties of more complicated probability density functions. However, this still gives a good indication of the range of values that were observed; the highest error value that is likely to be observed will be 2 to 3 times larger than the standard deviation indicated.

Upon first glance at the validation test results, it is clear that the natural frequencies above 20000 Hz—where the C system modes were experimentally truncated—are not accurately estimated, which makes intuitive sense. An analyst performing a single validation test is

likely to see large errors in those higher frequency modes, which would indicate the upper frequency limit of the substructure model. Note that the application table has been truncated, with frequencies near and past 20 kHz not shown. However, the application mirrored the validation test in that after 20,000 Hz, the natural frequencies of the model were no longer accurate.

The natural frequencies are quite good over the rest of the range of interest; however, mode 4, and to a lesser extent modes 5 and 6, seem to show an increased sensitivity to the damping error. Even up to 20% mode shape standard deviation, the noisy subcomponent model accurately predicts the natural frequencies of the validation structure. Hence, an analyst is likely to ascertain that this subcomponent model is acceptable even though there are considerable errors in the modal scale factors. This is as desired, since the following table (Table 3.5.2) shows that the model is quite adequate in the application of interest even with relatively large errors in the modal scale factor. Similarly, the analyst may infer an increased level of error in the lower modes due to the apparent sensitivity of the lower modes in the validation test.

	Truth Model	Mode Shape Standard Deviation = 5%		Mode Shape Standard Deviation = 10%		Mode Shape Standard Deviation = 20%		Mode Shape Standard Deviation = 50%	
	Freq (Hz)	Freq Mean (Hz)	Standard Deviation	Freq Mean (Hz)	Standard Deviation	Freq Mean (Hz)	Standard Deviation	Freq Mean (Hz)	Standard Deviation
4	768.5	754.1	2.95%	739.2	7.76%	723.0	10.82%	715.4	15.88%
5	1699.1	1653.1	1.36%	1640.1	3.49%	1613.5	6.46%	1555.2	18.01%
6	3155.8	3099.1	0.98%	3101.2	2.18%	3098.5	4.03%	3090.8	8.38%
7	5710.8	5666.9	0.94%	5672.6	1.62%	5666.0	2.96%	5637.9	5.87%
8	7752.6	7768.2	0.68%	7762.6	1.32%	7745.1	3.37%	7651.9	6.44%
9	9167.7	9163.5	1.46%	9157.1	1.81%	9117.9	3.60%	9080.4	9.66%
10	12813.4	12825.1	0.95%	12762.1	1.84%	12621.2	4.80%	12269.2	14.14%
11	14534.8	14441.1	1.58%	14469.7	1.69%	14487.6	4.42%	14514.9	10.03%
12	17500.3	17452.2	1.02%	17373.6	2.02%	17279.4	7.29%	18073.7	18.25%
13	19691.8	19809.5	2.98%	19774.1	2.86%	19794.7	5.49%	19979.6	7.50%
14	24704.2	30613.8	15.13%	29948.9	19.20%	27197.6	23.25%	22699.9	24.95%
15	25206.7	30430.6	13.43%	29784.4	16.79%	27894.8	21.72%	25225.4	26.81%
16	30035.6	29212.2	10.92%	29690.4	13.33%	30274.0	16.24%	31154.5	18.27%

Table 3.5.1: Validation test natural frequency distributions over four error levels for the modal scale factor error model. The first mode and to a lesser extent the next two modes show an increased sensitivity. The rest of the frequencies are fairly accurate even for high levels of error. The natural frequencies above 20 kHz are not accurate, which is expected because the C system was truncated at this level.

	Truth Model	5% Mode Shape Standard Deviation		10% Mode Shape Standard Deviation		20% Mode Shape Standard Deviation		50% Mode Shape Standard Deviation	
	Freq (Hz)	Freq Mean (Hz)	Standard Deviation	Freq Mean (Hz)	Standard Deviation	Freq Mean (Hz)	Standard Deviation	Freq Mean (Hz)	Standard Deviation
4	413.2	397.4	7.22%	397.3	12.91%	408.9	20.48%	441.8	35.49%
5	996.9	997.6	0.98%	996.4	2.13%	996.5	3.64%	997.4	6.77%
6	1182.9	1155.3	3.31%	1153.1	6.26%	1143.5	11.12%	1113.6	22.56%
7	2277.9	2237.2	1.58%	2232.3	2.40%	2220.8	3.83%	2188.5	7.21%
8	2717.2	2730.6	2.08%	2742.9	3.61%	2761.2	6.01%	2817.6	10.95%
9	2955.4	2911.1	1.40%	2914.7	3.21%	2919.9	5.29%	2906.2	9.24%
10	5636.5	5585.4	1.07%	5591.4	1.80%	5593.2	2.84%	5568.0	5.51%
11	7201.3	7225.2	0.29%	7223.7	0.95%	7219.9	3.00%	7156.5	6.75%
12	8991.5	9010.6	0.99%	9001.5	1.31%	8972.5	2.57%	8838.0	7.36%
13	10671.2	10451.7	1.58%	10438.3	2.29%	10391.1	3.63%	10268.3	7.46%
14	10840.7	10850.4	0.13%	10853.4	0.27%	10857.6	0.61%	10871.8	1.05%
15	13384.4	13512.3	0.57%	13533.9	1.58%	13568.2	4.21%	13677.3	8.68%
16	13609.5	13683.6	2.96%	13688.1	2.66%	13706.9	3.44%	13799.6	5.88%

Table 3.5.2: Application natural frequency distribution over four error levels for the modal scale factor error model. Note that the table is truncated well before 20 kHz, but the results were accurate out to that level and then became far less accurate.

3.5.3. Multiplicative Error Model

The multiplicative error model was analyzed similarly to the modal scale factor model, with results shown in Table 3.5.3 and Table 3.5.4. The trends seen in this case are very similar to those observed in the modal scale factor model. The error levels are once again small over most of the frequency band of interest, except for the first few elastic modes. However, although the trends are similar, they are much more severe for this noise model. Compared to the MSF error, the substructuring appears to be much more sensitive to errors of this type for similar levels of random noise. If this type of noise is present in an experiment, it must be kept to a relatively small level or the substructuring model will be in error. On the other hand, the validation test does indicate which modes are likely to have the largest errors in the application of interest, and it does give a good indication fo the level of error for all of the modes, demonstrating the usefulness of the validation test. Some of the modes have much larger errors than others, so one cannot estimate the error in the application of interest by simply averaging the validation test errors. Such an approach would overestimate the error in some modes and greatly underestimate it in others.

	Truth Model	**Mode Shape Standard Deviation = 1%**		**Mode Shape Standard Deviation = 5%**		**Mode Shape Standard Deviation = 10%**		**Mode Shape Standard Deviation = 20%**	
	Freq (Hz)	Freq Mean (Hz)	Standard Deviation	Freq Mean (Hz)	Standard Deviation	Freq Mean (Hz)	Standard Deviation	Freq Mean (Hz)	Standard Deviation
4	768.5	764.3	13.51%	711.1	39.03%	643.2	61.88%	608.7	82.55%
5	1699.1	1661.0	2.99%	1655.4	9.86%	1649.6	17.49%	1622.7	29.31%
6	3155.8	3099.3	1.49%	3099.6	3.37%	3095.1	5.10%	3090.1	7.35%
7	5710.8	5668.5	0.72%	5668.6	1.40%	5672.8	2.16%	5674.0	3.25%
8	7752.6	7764.5	0.42%	7774.0	1.44%	7778.7	2.41%	7762.9	4.34%
9	9167.7	9163.8	0.35%	9177.6	1.02%	9186.4	1.51%	9189.2	2.43%
10	12813.4	12858.1	0.74%	12922.2	2.09%	12964.9	2.93%	12979.9	4.17%
11	14534.8	14495.9	0.82%	14547.1	2.16%	14615.8	3.03%	14693.4	4.01%
12	17500.3	17489.6	0.40%	17620.6	2.38%	17727.8	4.05%	17826.0	6.08%
13	19691.8	19852.7	0.96%	19927.1	2.92%	19908.3	3.13%	19928.5	3.68%
14	24704.2	30042.3	15.75%	29650.7	12.11%	29646.3	15.55%	28151.0	20.33%
15	25206.7	31150.1	13.17%	30164.6	12.76%	30425.6	15.75%	29702.7	20.75%
16	30035.6	27970.8	4.25%	28525.9	8.41%	28603.7	9.04%	29095.8	11.37%

Table 3.5.3: Validation Test Natural Frequency Distribution for the Multiplicative Error Model. Note more severe error levels in the multiplicative model for similar levels of noise. The first modes show a large spread even for small error levels.

	Truth Model	**Mode Shape Standard Deviation = 1%**		**Mode Shape Standard Deviation = 5%**		**Mode Shape Standard Deviation = 10%**		**Mode Shape Standard Deviation = 20%**	
	Freq (Hz)	Freq Mean (Hz)	Standard Deviation	Freq Mean (Hz)	Standard Deviation	Freq Mean (Hz)	Standard Deviation	Freq Mean (Hz)	Standard Deviation
4	413.2	402.4	15.07%	377.7	33.87%	370.4	50.69%	384.3	60.01%
5	996.9	996.5	0.89%	992.8	2.30%	988.8	3.76%	981.9	5.62%
6	1182.9	1163.1	6.19%	1141.5	17.35%	1093.7	29.07%	1005.5	46.38%
7	2277.9	2244.7	1.68%	2241.8	4.03%	2233.3	5.53%	2212.3	7.71%
8	2717.2	2720.4	0.70%	2721.3	2.56%	2721.0	3.95%	2718.9	6.18%
9	2955.4	2912.5	1.44%	2920.8	3.97%	2928.5	6.20%	2923.1	9.04%
10	5636.5	5588.6	0.25%	5591.4	1.09%	5592.5	1.91%	5597.4	2.95%
11	7201.3	7220.1	0.52%	7230.1	1.65%	7238.8	2.92%	7239.3	5.26%
12	8991.5	9006.1	0.29%	9018.0	1.00%	9023.3	1.44%	9023.9	2.26%
13	10671.2	10498.1	1.20%	10497.3	1.76%	10509.2	2.14%	10536.9	2.82%
14	10840.7	10847.9	0.08%	10851.2	0.18%	10854.4	0.28%	10856.8	0.40%
15	13384.4	13527.7	0.78%	13547.9	1.70%	13602.4	2.36%	13676.6	3.43%
16	13609.5	13697.5	1.43%	13756.6	3.04%	13786.9	3.16%	13834.4	3.77%

Table 3.5.4: Application natural frequency distribution over four error levels for the multiplicative error model. Trends are generally the same as in the modal scale factor error model. A high sensitivity of modes 4 and 6 is observed. Accurate natural frequencies end at 20 kHz.

3.5.4. Cross Axis Sensitivity Error Model

The cross-axis sensitivity model results are shown in Table 3.5.5. They show slightly higher disruption of natural frequencies of the assembled system than the modal scale factor error model, but not as much as the multiplicative model. Once again mode 4 seems to exhibit the highest sensitivity, but the sensitivity seems to spread more evenly across the first 3 elastic modes for this noise model than it did for the others. The relationship between the error levels in the validation test and application of interest are examined in more detail in a subsequent section. Noise levels in the 4th and 6th mode were around of 10% standard deviation for the highest error level, matching the validation test quite well.

	Truth Model	**Misalignment Standard Deviation = 1 Degree**		**Misalignment Standard Deviation = 5 Degrees**		**Misalignment Standard Deviation = 10 Degrees**		**Misalignment Standard Deviation = 20 Degrees**	
	Freq (Hz)	Freq Mean (Hz)	Standard Deviation	Freq Mean (Hz)	Standard Deviation	Freq Mean (Hz)	Standard Deviation	Freq Mean (Hz)	Standard Deviation
4	768.5	728.6	4.06%	700.8	7.45%	695.2	9.54%	688.2	12.01%
5	1699.1	1648.0	1.59%	1644.3	3.09%	1644.7	5.61%	1645.4	10.11%
6	3155.8	3133.0	2.16%	3120.1	5.68%	3090.0	6.58%	3022.1	6.89%
7	5710.8	5672.3	0.32%	5696.2	1.71%	5693.0	2.73%	5623.1	3.82%
8	7752.6	7758.4	0.30%	7754.5	0.60%	7743.6	1.10%	7680.1	4.34%
9	9167.7	9157.1	0.21%	9165.8	0.64%	9162.2	1.17%	9143.7	2.29%
10	12813.4	12815.7	0.42%	12807.8	0.89%	12787.0	1.60%	12744.7	3.12%
11	14534.8	14446.5	0.62%	14444.8	0.72%	14448.3	1.12%	14460.2	2.38%
12	17500.3	17456.2	0.27%	17444.2	0.62%	17418.2	1.26%	17310.5	3.96%
13	19691.8	19772.2	1.31%	19705.0	1.41%	19679.2	1.37%	19689.3	2.62%
14	24704.2	28409.0	13.06%	28252.4	7.88%	28132.1	9.20%	28121.9	15.56%
15	25206.7	29146.5	11.77%	28871.5	10.59%	29015.3	12.34%	29239.9	17.26%
16	30035.6	27937.4	5.94%	30317.4	14.59%	31511.1	16.13%	32381.9	16.25%

Table 3.5.5: Validation natural frequency distribution over four error levels for the cross-axis sensitivity error model.

	Truth Model	Misalignment Standard Deviation = 1 Degree		Misalignment Standard Deviation = 5 Degrees		Misalignment Standard Deviation = 10 Degrees		Misalignment Standard Deviation = 20 Degrees	
	Freq (Hz)	Freq Mean (Hz)	Standard Deviation	Freq Mean (Hz)	Standard Deviation	Freq Mean (Hz)	Standard Deviation	Freq Mean (Hz)	Standard Deviation
4	413.2	395.6	2.29%	391.0	3.84%	388.9	5.93%	386.5	11.44%
5	996.9	997.0	0.03%	996.5	0.17%	994.9	0.54%	988.9	1.48%
6	1182.9	1121.4	4.34%	1097.5	11.65%	1101.9	13.80%	1085.3	13.61%
7	2277.9	2282.3	4.64%	2226.6	8.98%	2167.5	9.76%	2081.9	9.17%
8	2717.2	2721.5	0.02%	2723.2	0.29%	2725.3	1.03%	2734.8	4.31%
9	2955.4	2920.8	0.89%	2922.4	2.53%	2914.7	2.88%	2888.9	3.11%
10	5636.5	5588.1	0.14%	5593.1	0.50%	5591.8	0.89%	5565.7	1.40%
11	7201.3	7214.9	0.37%	7211.2	0.60%	7209.1	1.18%	7162.3	4.64%
12	8991.5	8998.1	0.20%	8996.4	0.57%	8989.2	0.93%	8978.0	1.92%
13	10671.2	10478.2	0.51%	10468.7	0.80%	10462.0	1.27%	10457.8	2.01%
14	10840.7	10845.3	0.02%	10845.2	0.05%	10845.5	0.08%	10846.2	0.25%
15	13384.4	13475.3	0.44%	13460.7	0.42%	13439.8	0.85%	13433.1	1.89%
16	13609.5	13616.3	0.96%	13592.1	0.75%	13591.2	1.01%	13561.1	1.82%

Table 3.5.6: Application natural frequency distribution over four error levels for the cross-axis sensitivity error model.

3.5.5. Sensitivity Trends

For all three of the noise models studied, the first elastic modes were more sensitive to error than the rest of the modes in the frequency band, and this occurs both in the validation test and the simulated application of interest. The sensitive modes (typically mode 4 in the validation test and modes 4 and 6 in the application) all contain the B system in a first-bending-type configuration (Figure 3.5.3). The analyst, seeing that this specific mode is sensitive in the validation test, could infer that similar modes in the application of interest might be sensitive to noise and therefore be in error. This might lead the analyst to change the way the experiment is performed to ensure the accuracy of extracting this mode.

Another trend is that the application predictions are much better for the 5th mode near 1000 Hz even though the modes nearest to it are quite sensitive to errors. This mode consists primarily of motion of the application of interest (, and the errors in the experimental model do not contribute significantly to that mode shape.

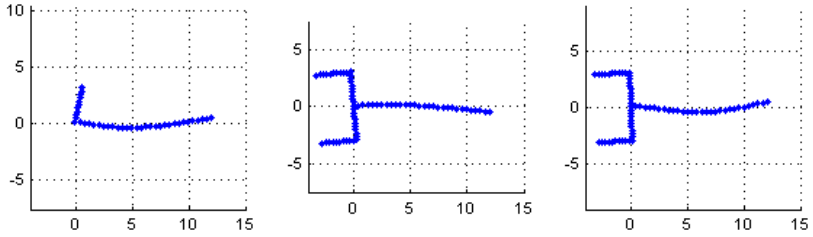

Figure 3.5.3: Most sensitive mode shapes. From left to right: Validation mode 4, Application mode 4, and Application mode 6.

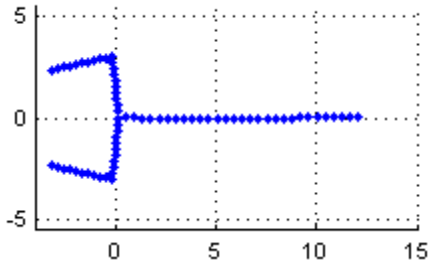

Figure 3.5.4: 5th mode shape of the application structure. There is very little motion of the experimentally-based component in this mode, so it is not very sensitive to errors in that component.

3.5.6. Correlation between Validation Test and Application

The bulk test data shows a good correlation between the validation experiment and the application. However, the analyst would not wish to perform thousands of validation experiments to determine the accuracy of the system of interest as was done in this effort. In practice, an analyst can probably only perform one or two tests, and ideally this would lead to a good measure of the validity of the experimentally derived substructure model.

As shown above, the modes of each system were not affected equally by error. Specifically, these systems showed an increase in sensitivity of the first few modes and low sensitivity

over the rest of the spectrum below 20 kHz. However, it is still desirable to have some form of metric with which to rate the validation results and extrapolate to the application of interest, and this may largely be application specific. One could imagine scenarios in which specific modes or frequency ranges are more important to match well, or perhaps the worst case error is of greatest interest. In this simulated application, all modes are assumed to be of equal importance and so an average of errors in the natural frequencies is used. It should be made clear, however, that this value should not be used as an estimate for the error of any specific mode of the application of interest, because the validation test clearly indicated that the first few modes were more sensitive. This value should only be comparing the overall performance (in terms of minimizing error) of the substructure model.

For this investigation, the average percent error of the elastic natural frequencies below 20 kHz was found for the validation test and the application, and these results are shown in Figure 3.5.5 through Figure 3.5.7. Each figure includes all of the trials from each level of error. The validation test is plotted in red, and appears as an increasing line since the trials were sorted based on their average error. The corresponding average application error is shown with a blue dot and shows some scatter, indicating, for example, that even when the average error in the validation test was only 1%, the average error in the application test could be as low as 0.2% or as high as 7%, depending on the specific pattern of noise that one happened to obtain. On the other hand, the results show that when the average error in the validation test was 5%, the error in the application test was also very likely to be quite large.

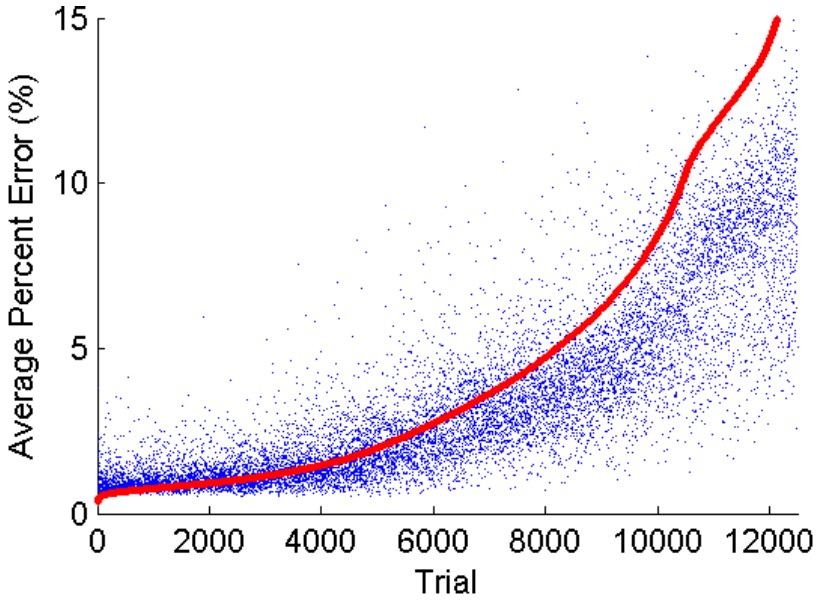

Figure 3.5.5: Average percent error in natural frequencies between 0 and 20 kHz for multiplicative error model; trials sorted by the average error in the validation test.

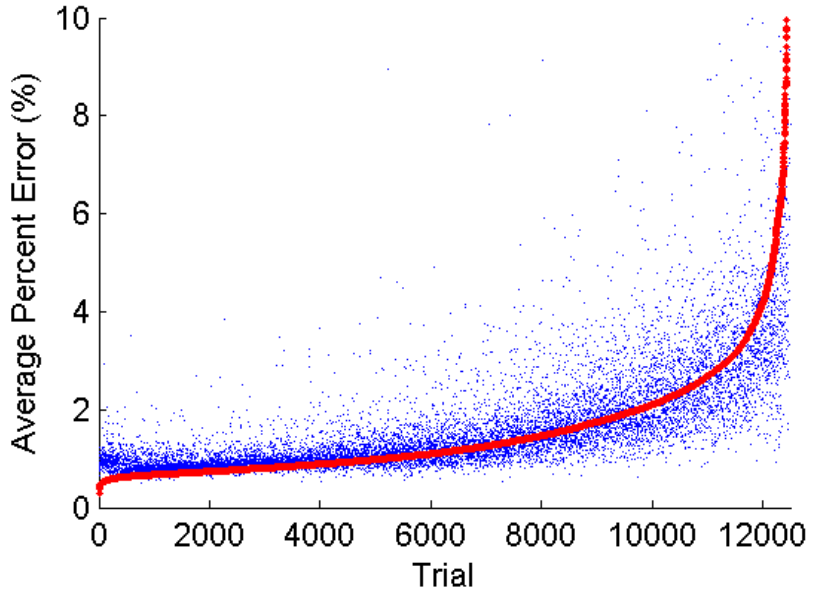

Figure 3.5.6: Average percent error in natural frequencies between 0 and 20 kHz for modal scale factor error model; trials sorted by validation error level.

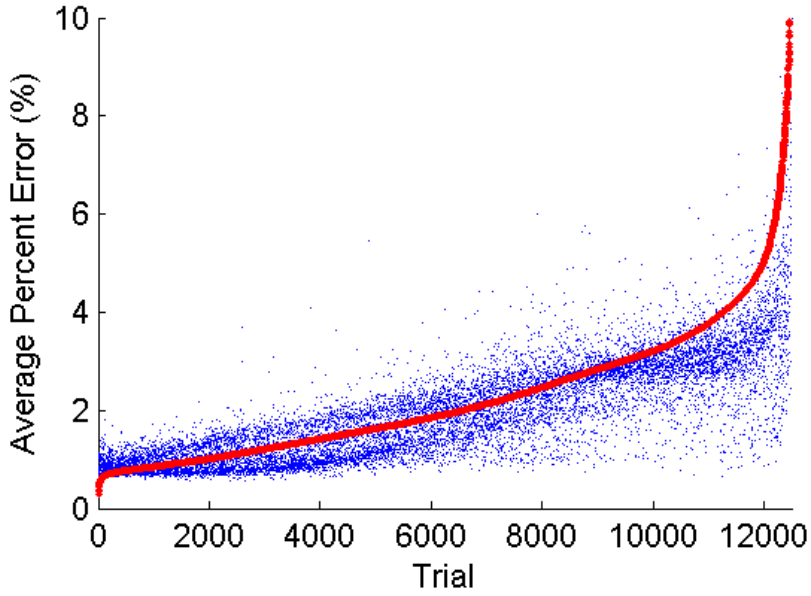

Figure 3.5.7: Average percent error for cross-axis sensitivity error model; trials sorted by validation error level.

The MSF and cross-axis sensitivity noise models, shown in Figure 3.5.6 and Figure 3.5.7, show similar trends, although the correlation between the validation test and the application of interest is even stronger. For example, for the cross-axis sensitivity noise model an average error of 2% in the validation test produces between 1 and 3% error in the application of interest. This suggests that if either of these noise sources is dominant then one should be able to obtain a very good estimate of the average error in the application of interest from the validation test. Unfortunately, it seems there are a few cases, especially in the multiplicative noise model, where the validation test error is an order of magnitude below the application of interest; even though they are rare, they are still a reality of this method, so the analyst must still use good judgment in analyzing the results of the application structure.

3.5.7. Spurious Modes

In this investigation, up to 3 spurious modes appeared in the frequency band of interest. These modes were found to be very sensitive to noise. For low error levels, the modes were just a nuisance insofar as the genuine modes had to be sorted from the spurious modes. For higher error levels, these modes seemed to interfere more with the genuine modes. For some trials, a vibration-absorber effect was seen in which a real mode was split into two modes at different frequencies.

It was seen that a number of the modes of the experimental C system were modes purely of the transmission simulator (Figure 3.5.8). When the transmission simulator was subtracted, the physical meaning of these modes was also subtracted; however, the coordinate still existed. But since the shape has very little motion on the B structure, it contributes very little to FRFs of the built up system.

In the presence of noise, this can change dramatically. Due to the noise, the analytical transmission simulator model does not perfectly cancel out the experimental transmission simulator, so some physical meaning is left behind. This, coupled with noise (and therefore motion) on component B, will make the spurious modes appear on the FRF and interact with other modes.

Instead of trying to mitigate the effects of the spurious modes, it is better to design an experiment in which these modes will not appear. The key is to design system C so that there are no mode shapes containing only motion of the transmission simulator. In this case, this

could be done by removing the symmetry of the system by moving the connection point along the transmission simulator or shortening or lengthening it on either side.

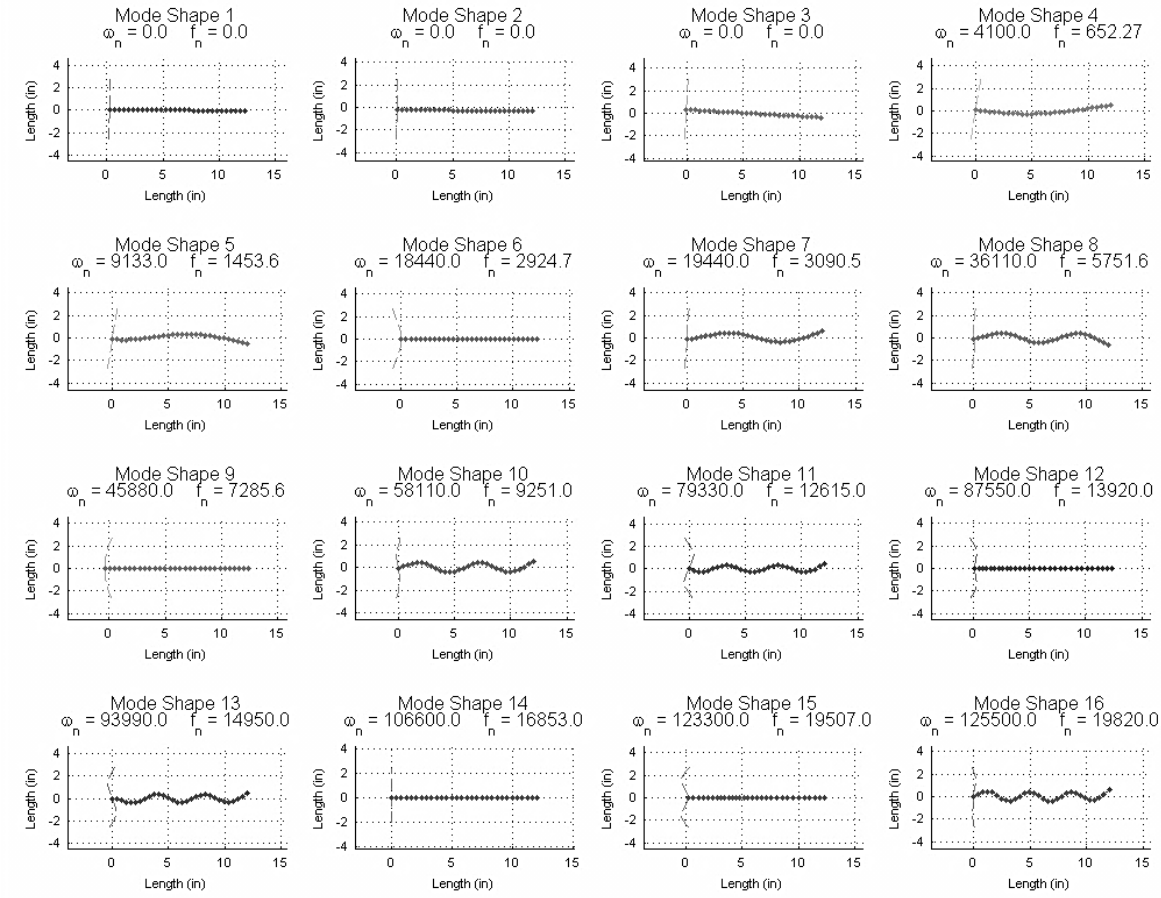

Figure 3.5.8: Mode shapes of the C system. Note modes 6, 9, and 14 have very little motion on the B system (heavy dotted line) and consist primarily of motion on the transmission simulator (light dotted line).

3.6.Conclusions

This work has investigated the effects of experimental errors on a validation experiment. The Modal tests were simulated by adding random noise to a model comprised of only low frequency modes (due to modal truncation). The contaminated model was then used to

predict the natural frequencies that would be obtained in the validation test and the comparison between the prediction and validation test was used to assess the accuracy of the substructure model. To get a grasp of the overall effect that the noise has, varying levels of noise were added, and the distributions of the modal parameters of the built-up system were compared to the true values. Only one system was studied in this work and the trends observed here may not hold for every system. However, the phenomena observed and lessons learned are hoped to be generally applicable.

Good results were obtained for most of the frequency band of interest, even when the noise level was quite high. This suggests that low levels of error won't completely derail one's efforts to obtain a valid substructure model. However, an interesting sensitivity was discovered for the lower elastic modes of this system; the modes were certainly not affected equally by the simulated experimental errors. The natural frequencies' distributions appeared slightly non-normal with increased kurtosis.

The validation test was also found to predict the results in the hypothetical application of interest quite well; a very strong correlation was observed between the average errors in the natural frequencies in validation test and those in the application of interest. However, one must use caution when attempting to place error bars on the predicted natural frequencies since the simulations clearly showed that certain modes could be many times more sensitive than the average. Severe outliers were also found in some trials in which the application error did not seem to correlate with the validation test. The vast majority of the time, the validation experiment has shown to be a good (and if implemented correctly, cost-effective) metric for assessing the validity of a substructure model.

4. Generator/Engine Substructuring Application

The results of the validation test were encouraging, so a more difficult case was attempted. A generator manufacturer was interested in using substructuring to characterize different combinations of engines and generators. Each engine/generator combination will have different characteristics, which could possibly result in a resonance near the operating frequency, but it is not practical to test every possible engine/generator combination. It would be better to analytically couple different models together to find any unfortunate dynamic characteristics. The generator, which is basically a coil of wire in a cylindrical enclosure may be easier to model analytically than an engine with all of its different components—valves, shafts, and pistons. It may be much less expensive to develop an experimental engine model which can be used with any analytical generator model.

The objective of this effort is to accurately predict the first bending modes of the engine/generator system. These modes are known to have the largest deflections and contribute most to the fatigue failure of the system. These will be the most important modes to avoid during the operation of the generator.

4.1. Test Models

Although the end goal is to do experimental-to-analytical substructuring with this system, the important lessons taken from this effort will be learned from the investigation of the interface constraints and truncation issues. It was therefore decided to first pursue this goal in a purely analytical sense, using finite element models instead of experimental substructures. There are several advantages to this. By doing this, the analyst can be sure that poor results are due to a flaw in the substructuring setup instead of simply taking bad data. This would also offer

the analyst the ability to simplify the model and zero in on poor behavior if the substructuring results were not good. Finally, this gives the analyst the accurate truth results so the validation test results can be compared to the application test results.

An engine finite element model for use in this study was graciously donated by the Kohler Company; however the mesh was too refined to successfully run in a realistic amount of time on a desktop computer. It was also found that these models contained a large number of local modes due to the large number of intricate features on the engine (e.g. the fins on the heat exchangers). These modes consist of very little motion of the global system, and therefore would not be found in an experiment since the small intricate features would likely not be instrumented. To ease the computational burden of these large models with many extra modes, new models were created which were more sparsely meshed and defeatured where possible. The crank shaft and pistons were also removed. Two generator models were also created for this analysis given the assumption that the dynamic models of the generators were little more than capped cylinders with a thicker annular region to represent the coils.

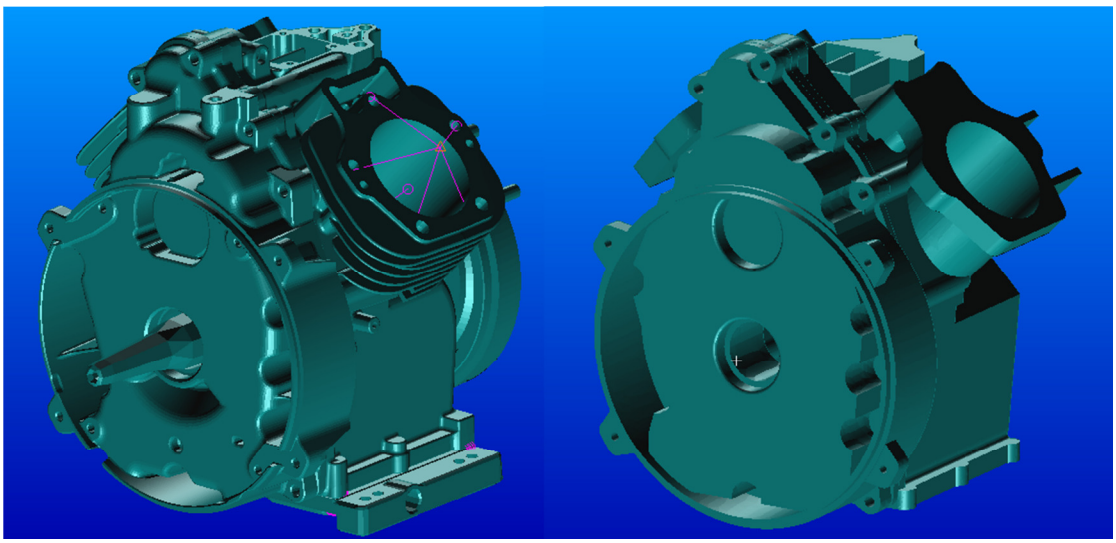

Figure 4.1.1: Kohler supplied engine FE model (left); recreated engine FE model (right)

4.2. Substructuring Overview

Due to the complexity of the interfaces between individual components (14 bolts around the closure plate and contact on the entire interface), a simple point-by-point connection scheme would be tedious to set up and require many measurement points to approximate a continuous interface (and many would likely be redundant). In connecting the closure plate to the engine, it may be appropriate to use point constraints on the bolt locations, but in a practical test (which this effort attempts to emulate) these would be difficult to measure; due to the presence of the bolt and the complicated geometry surrounding it, a good surface to mount the accelerometer is not easily found. The transmission simulator method would be much better in this situation, and so it will be used.

4.2.1. Transmission Simulator Method Considerations

In the transmission simulator method, motions of the points on the transmission simulator are constrained in a least-squares sense to the motions of the points on other structures. For easiest implementation, it is helpful to have similar geometry between the structures so the points in the same place can be constrained directly. For this reason, it is desirable to include in the transmission simulator at least some portion of the structure which is consistent across each built-up structure. For instance, the wind turbine substructuring attempt in Section 2.2 used the hub of the turbine as the transmission simulator, and this was common to each substructure.

Similar to using the hub, the interface between the tower and the blades of the wind turbine, as the transmission simulator, this effort used the engine closure plate, which is the interface between the generator and the engine. One of the key benefits of the transmission simulator

is that it mass-loads the interface of the engine. However, it wasn't clear the closure plate would mass-load the interface enough to capture the bending information necessary to describe the first elastic modes of the engine/generator system, so a simplified mock generator was attached to the front plate to increase the mass and make the interface more accurately represent what is found in the actual system.

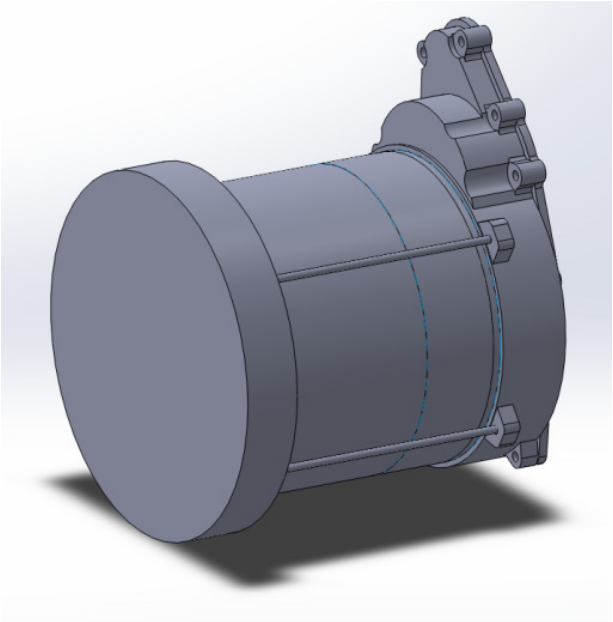

Figure 4.2.1: Closure plate attached to the mock generator.

The mock generator consisted of the same interface as the other generators used in this study, but keeping in mind the ideal transmission simulator properties (inexpensive to produce, easy to model analytically) the mock generator was shortened and given a large mass on the end. In practice, this mass would be a large block of metal, which is easy to model, where the real generators would be complex components with various materials.

4.2.2. Substructure Models

As described in the previous section, the front plate will be included with the mock generator in the transmission simulator, as well as in each generator model. Using the terminology from previous sections, system C will be the substructure on which the experimental test is performed and in this case contains the engine, closure plate, and mock generator. The transmission simulator (system A), consisting of the closure plate and the mock generator, will be subtracted from system C to create the experimentally-based component B, which consists of the engine.

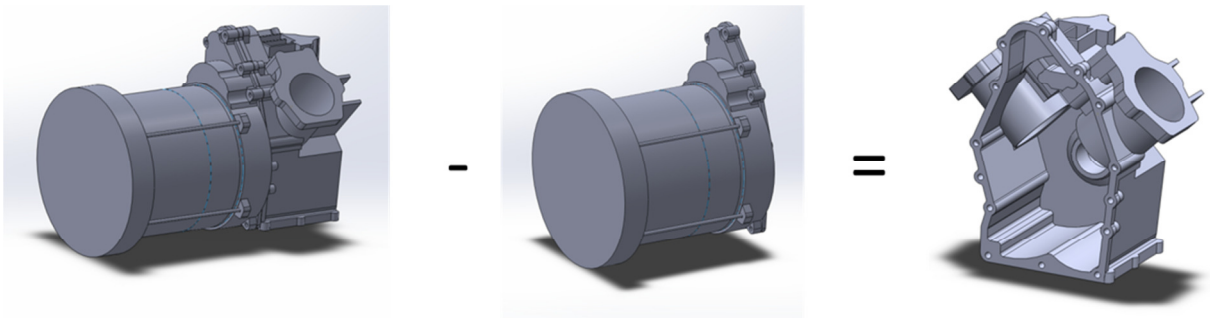

Figure 4.2.2: Schematic of the substructuring procedure, in which System A (middle) is subtracted from System C (left) to give just the engine component, System B (right).

The validation test then proceeds similarly to Section 3.1. The validation experiment should ideally be inexpensive and accurately modeled. Given that the motivation is based on attaching several different analytical generator models to the engine, it can be safely assumed that the manufacturer has several generators that are accurately modeled. Then, instead of creating a separate fixture for the validation test, one of the generators of interest can be used. This one test can then be used to validate the experimental substructure model which can be used to predict the response for all the other generators, rather than testing each one. Following similar nomenclature to the previous sections, the experimentally-based

component B (engine) is attached to a validation fixture D (closure plate and validation generator) to form the validation assembly E. A modal test is performed on this built up assembly to get truth data against which the substructured model can be compared.

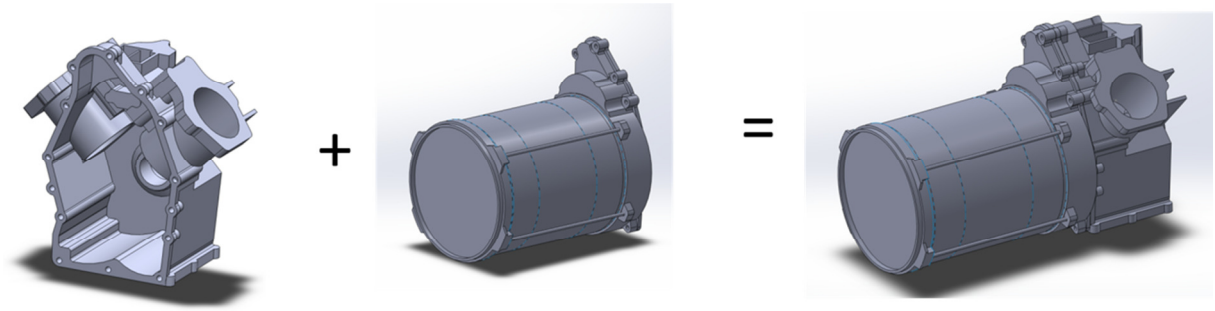

Figure 4.2.3: Schematic of the substructuring procedure, in which System B (left) is coupled to System D (middle) to create the validation assembly E (right).

The application of interest in this scenario is substructure B (engine) attached to different generators. Here a longer generator with more coils is investigated, which simulates a variant on the generator that would produce power. This application generator along with the closure plate (System F) will be coupled to system B to form the application system G.

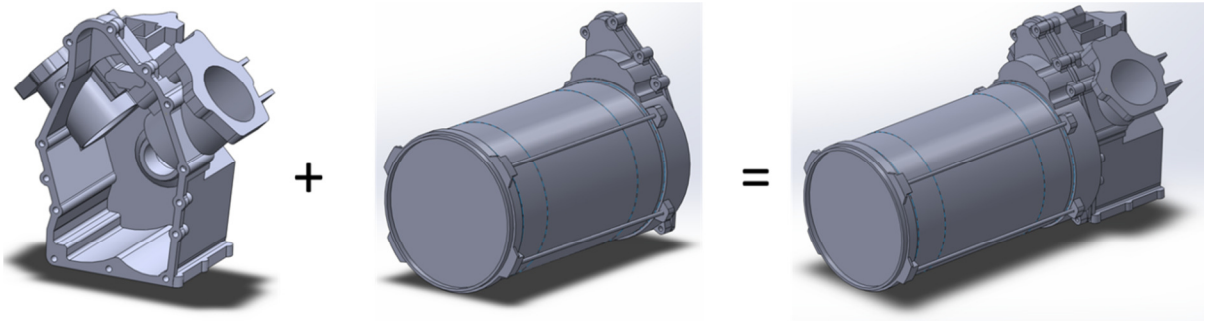

Figure 4.2.4: Schematic of the substructuring procedure in which System B (left) is coupled to System F (middle) to create the application assembly G (right).

4.3. Experimental Simulation

All the finite element models (A, C, D, E, F, and G) were solved for the first 250 modes in NASTRAN, which gave modes up to approximately 10,000 Hz. However, as this effort attempts to imitate an experiment, several considerations need to be taken into account.

Realistically, 250 modes would never be extracted from a modal test, and the frequency band of interest would not be near 10,000 Hz, so modal truncation would need to be considered. The full mode shape matrices would need to be reduced to some sensor set of degrees of freedom which would be much smaller. Finally, local modes (for example, bending of the rods that secure the generator) would be missed because these features would likely not be instrumented.

4.3.1. Sensor Degrees of Freedom

The finite element models give results at each node, but to mimic experiments this spatial resolution needed to be reduced to a relatively small set of sensor degrees of freedom. To provide better visualization, often experimentalists will use triaxial accelerometers even though separate uniaxial accelerometers may be a more efficient use of channel resources. This effort therefore utilized triaxial accelerometers. An optimal sensor location algorithm utilizing effective independence [18] was used to place accelerometers. This algorithm requires a target set of modes as well as a seed set of accelerometers to which additional accelerometers are added.

The triaxial effective independence algorithm operates on a set of target modes of the system of interest. These target modes were manually selected to be global modes below 3000 Hz in

each system. Had all modes below 3000 Hz been used, the algorithm would group triaxial accelerometers on the portions of the geometry undergoing local motions (see Figure 4.3.1). In an actual test, these local motions would not be of interest and these features would not be instrumented.

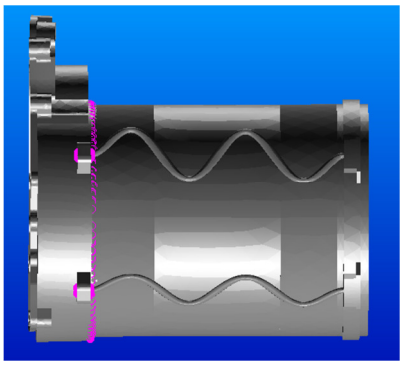

Figure 4.3.1: This mode shape almost exclusively consists of motion in the bolts which secure the generator to the closure plate.

The algorithm was started using a random seed accelerometer on the closure plate, and accelerometers were added to the closure plate based on maximizing the determinant of the information matrix as described in [18], using a candidate set of accelerometers consisting of the surface nodes of the plate and target modes taken from the mode shapes of system A. Twenty triaxial accelerometers were added in this fashion. Then using the same target mode set, ten triaxial accelerometers were added to candidate nodes on the surface of the mock generator using the existing plate triaxes as the seed set of accelerometers.

Accelerometers were then placed onto the engine system using the mode shapes of system C using the set of accelerometers that had been placed on the system A as the seed set.

A similar procedure was used to place accelerometers on the application and validation generators in systems D and F. The target modes were chosen as global modes below 3000 Hz, and the seed set was the set of accelerometers already placed on the plate. By keeping consistent points on the closure plate between tests, these points could easily be used to form the modal constraints in the transmission simulator method.

4.3.2. Modal Truncation

As the first elastic modes were found near 900 Hz, modes up to three times that amount were kept to ensure an adequate modal basis for substructuring. In addition to discarding modes based on frequency, modes were also discarded based on their shape. Several modes were local modes consisting of bending of the attachment rods (see Figure 4.3.1). Since the motion of the entire structure is small on most of these modes, they would likely not appear on an FRF of the structure. To investigate which mode should be captured by the test, the norm of the numerator of the FRF matrix $\Phi_r \Phi_r^T$ was found for each mode r using the degrees of freedom selected in the previous section. For this test, it was seen that a majority of these local modes fell below a value of 0.5, and so the modes below this threshold were discarded. Plots of the truncations are shown in Figure 4.3.2. The vertical dashed line signifies the cutoff for the frequency truncation at 3000 Hz, and the horizontal dashed line signifies the threshold at which the modes were discarded by the shape metric.

After performing the truncation based on shape, it should be noted that some local modes still exist in the model. These local modes also have a significant motion of the rest of the structure. These modes will not be very distinguishable from one another due to

instrumentation choices, but they still contain important dynamic information and therefore should not be discarded.

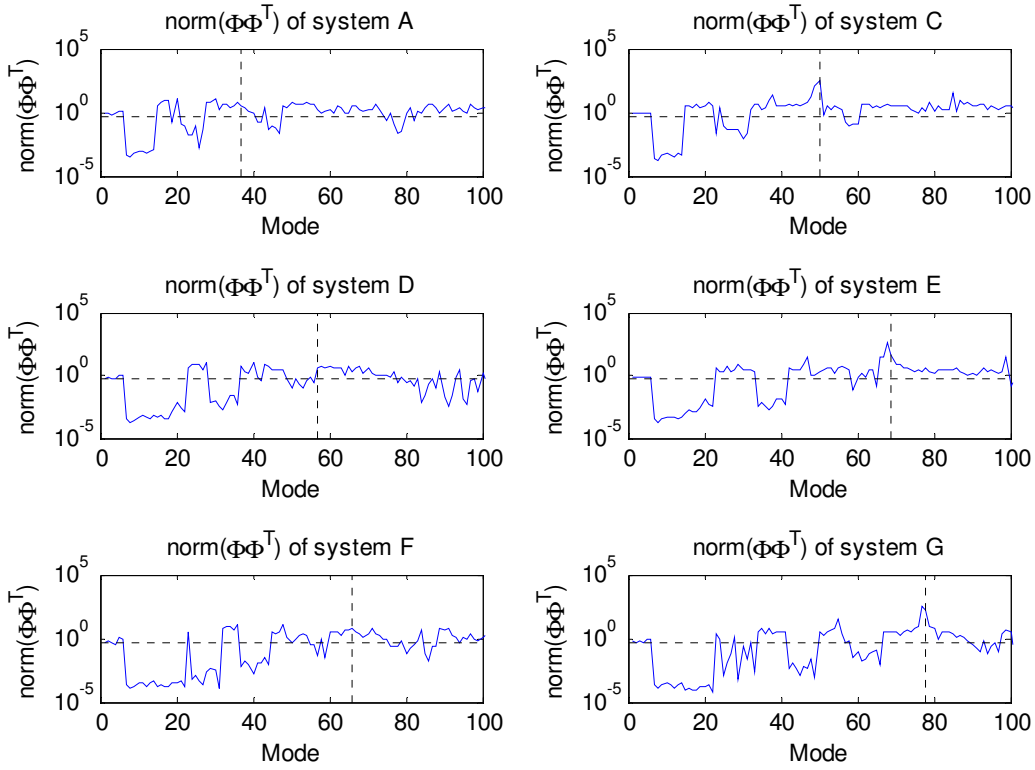

Figure 4.3.2: Truncation of modes based on the $\mathbf{norm(\Phi\Phi^T) > 0.5}$ metric and frequency less than 3000 Hz. Only the modes in the upper left quadrant of each plot were kept.

4.4. Substructure Model Results

The models of systems A, C, D, and F would be used for substructuring calculations, and system E would be compared to the substructured system C-A+D. System G would typically not be known; however, in this case we do know the results. If the results truly were in question, a modal test could be performed on this structure since it is small enough, but this

is what we are trying to avoid. A complete list of each system's natural frequencies is given in Appendix C.

4.4.1. System C

Subsystem C is the starting model from which the Transmission Simulator is subtracted. 6 rigid body modes and 28 elastic modes were extracted below the frequency cutoff of 3000 Hz.

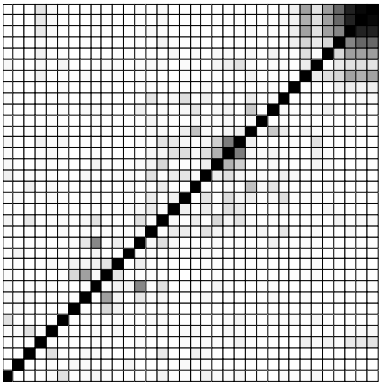

Figure 4.4.1: MAC of System C. All mode shapes are independent on the sensor set except for the very high frequency modes.

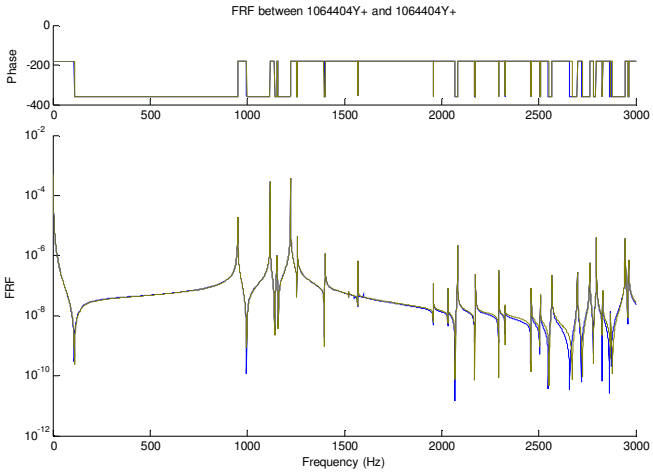

Figure 4.4.2: Drive point FRF reconstructed using the truncated mode set (green) and the original set (blue). 2% damping assumed.

The MAC of system C (Figure 4.4.1) shows three or four of the highest modes are not independent from one another. This is due to a series of closely spaced local modes which also contain an adequate amount of motion on the global system that they are dynamically important. The local motions are not instrumented sufficiently to distinguish these motions from one another.

4.4.2. System A

System A consists of the mock generator and closure plate, and is subtracted from system C to create the experimentally-based component B. 6 rigid body modes and 15 elastic modes were extracted below 3000 Hz for this system.

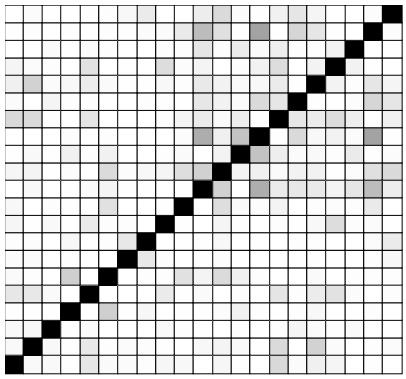

Figure 4.4.3: MAC of System A. All mode shapes are fairly independent.

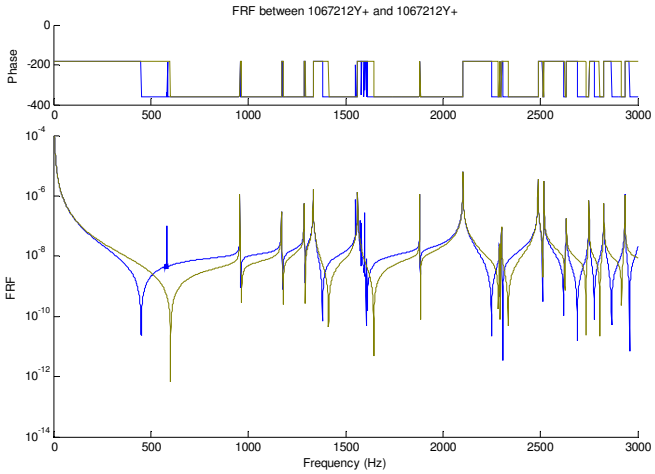

Figure 4.4.4: Drive point FRF reconstructed using the truncated mode set (green) and the original set (blue). 2% damping assumed.

Though the mode shapes are independent, the discarding of weakly excited modes has caused noticeable changes to the system FRFs (Figure 4.4.4). The anti-resonance in the 500 Hz range has shifted substantially, and a few peaks are missed. However, the strongest peaks are captured which have the greatest influence on the system.

4.4.3. System D

System D is the system which will be added to system C-A to create the validation assembly. Using the previously mentioned criteria, the model of System D consists of 6 rigid body modes and 20 elastic modes that were extracted below 3000 Hz.

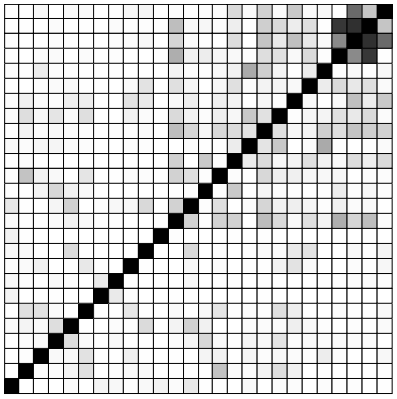

Figure 4.4.5: MAC of System D.

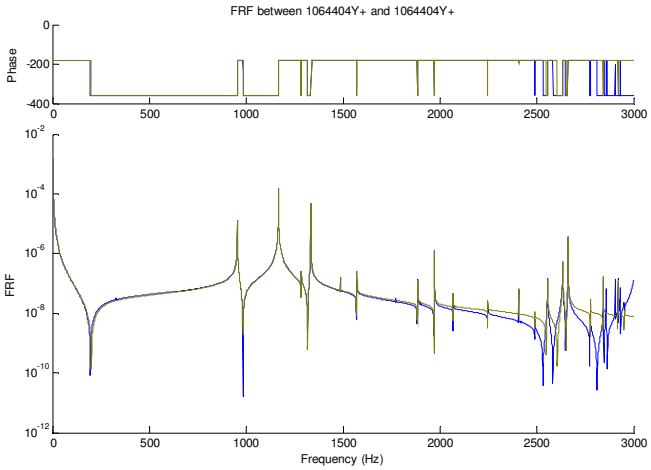

Figure 4.4.6: Drive point FRF showing the truncated mode set (green) and the original mode set (blue).

Like System C, System D has some high frequency modes that are not quite independent according to the MAC, as the instrumentation does not adequately distinguish between the local modes. Still, the modes contain enough global motion to meet the shape criterion, so they were not discarded.

4.4.4. System F

System F is added to System C-A to create the application model. System F consists of 6 rigid body modes and 23 elastic modes.

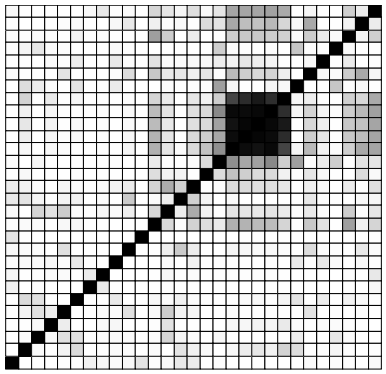

Figure 4.4.7: MAC of System F. A large block of local modes is very distinct.

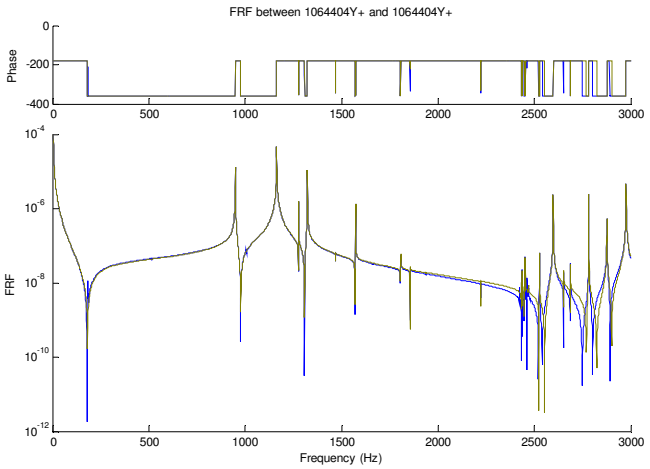

Figure 4.4.8: Drive point FRF showing the truncated mode set (green) and the original mode set (blue).

System F also contains a large number of local modes, of which a few are captured since they consist of enough global motion. These modes have very similar shapes, as evidenced by the MAC plot in Figure 4.4.7, which shows that modes 18-23 have similar shapes as measured by the sensor set. In the FRF, these modes appear closely spaced just under 2500 Hz, and it appears that only a few of the local modes are captured.

4.5. Constraints

To perform the substructuring, free modes of the transmission simulator were used to define modal constraints between the two systems. Since all of the degrees of freedom on the transmission simulator exist on system C, each measured point on the transmission simulator was used to form the subtraction constraint which coupled the negative transmission simulator model to system C, and the partition of the mode shape matrix corresponding to these points is labeled with the subscript m in (4.5.1).

In coupling the D or F systems to the experimental model, not all of the degrees of freedom of the transmission simulator could be used. Measurement points on the mock generator portion of the transmission simulator do not exists on the generator models; only the plate measurement points are shared. For this set of constraints, only these plate degrees of freedom, designated by the subscript p in (4.5.2), were used to formulate the constraints. It is important to use a coordinate set that completely captures the motion of the modes in A so $\boldsymbol{\Phi}_{A,p}$ is full column rank, so one cannot arbitrarily exclude sensors from this constraint formulation. But since the majority of the motion in each mode of A is contained in the plate, this sensor truncation does not cause ill-conditioning in the constraints.

The full constraint equations to couple systems C, D, and A are then

$$\begin{bmatrix} \boldsymbol{\Phi}_{A,m}^{+}\boldsymbol{\Phi}_{C,m} & \mathbf{0} & -\mathbf{I} \\ \mathbf{0} & \boldsymbol{\Phi}_{A,p}^{+}\boldsymbol{\Phi}_{D,p} & -\mathbf{I} \end{bmatrix} \begin{Bmatrix} \mathbf{q}_C \\ \mathbf{q}_D \\ \mathbf{q}_A \end{Bmatrix} = \mathbf{B}\mathbf{q} = \mathbf{0} \qquad (4.5.1)$$

showing that both substructures are coupled to the transmission simulator degrees of freedom, but each with a different set of points. Similarly the constraints to couple systems C, F, and A are

$$\begin{bmatrix} \boldsymbol{\Phi}_{A,m}^{+}\boldsymbol{\Phi}_{C,m} & \mathbf{0} & -\mathbf{I} \\ \mathbf{0} & \boldsymbol{\Phi}_{A,p}^{+}\boldsymbol{\Phi}_{F,p} & -\mathbf{I} \end{bmatrix} \begin{Bmatrix} \mathbf{q}_C \\ \mathbf{q}_F \\ \mathbf{q}_A \end{Bmatrix} = \mathbf{B}\mathbf{q} = \mathbf{0} \qquad (4.5.2)$$

4.6. Substructuring Results

For both the validation and the application test, the substructured prediction matched the truth tests very well. In each case, a strong diagonal was seen in the MAC matrix and the

frequencies match very well. Damping was not considered since the models were derived from a finite element model with no explicitly modeled damping.

4.6.1. Validation Test Results

Comparisons of predicted natural frequencies and mode shapes for the elastic modes of the validation test are shown in Table 4.6.1, Figure 4.6.1, and Figure 4.6.2. The frequencies of the substructured modes are a very close match to the frequencies of the truth model. The mode shapes don't compare as well, as judged by the MAC.

The MAC plot in Figure 4.6.2 shows a strong diagonal, but eventually breaks down. The high frequency portion of the truth model consisted of several similarly-shaped, closely-spaced modes, so the sorting algorithm from equation (2.2.3) selected the same substructured mode for many of the truth modes.

The correlation between the predictions and truth test show good results up to approximately 2500 Hz with just a few poorly correlated modes in that range. Still, for a first attempt at substructuring this complex and modally dense system, the results are quite good even though many modes were thrown out since they wouldn't be captured by the sensors.

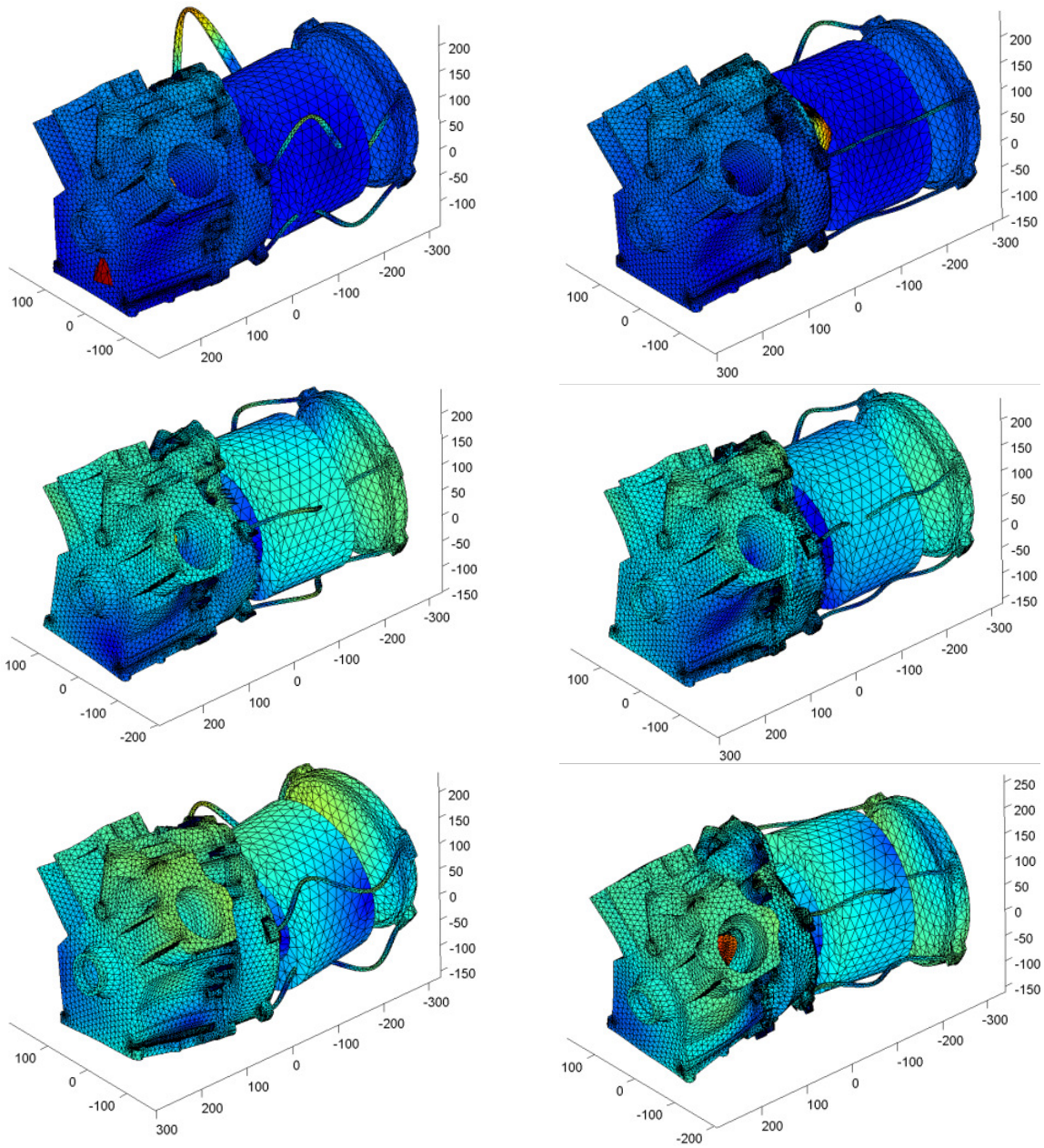

Figure 4.6.1: First three elastic mode shapes of the validation assembly E=C-A+D for the truth test (left) and substructured model (right). Top: 1st Elastic Mode – Small generator up-down bending, large closure plate motion. Middle: 2nd Elastic Mode – Large generator up-down motion. Bottom: 3rd Elastic mode – Large generator left-to-right motion. Local motions of the rods that attach the generator do not match as well as global motion of the engine and generator.

Truth Mode	Frequency (Hz)	Substr Mode	Frequency (Hz)	Error	MAC
Mode 7	950.2	Mode 7	948	-0.26%	99.40%
Mode 8	1084	Mode 8	1071	-1.16%	81.10%
Mode 9	1109	Mode 9	1106	-0.28%	72.90%
Mode 10	1212	Mode 10	1213	0.10%	98.10%
Mode 11	1252	Mode 11	1224	-2.24%	92.40%
Mode 12	1327	Mode 12	1330	0.24%	96.60%
Mode 13	1380	Mode 13	1379	-0.07%	98.90%
Mode 14	1473	Mode 14	1472	-0.05%	93.30%
Mode 15	1514	Mode 15	1523	0.60%	61.50%
Mode 16	1538	Mode 16	1542	0.25%	71.20%
Mode 17	1640	Mode 17	1650	0.57%	94.70%
Mode 18	1943	Mode 18	1916	-1.44%	90.80%
Mode 19	1998	Mode 20	1998	-0.02%	85.30%
Mode 20	2005	Mode 19	1987	-0.87%	52.90%
Mode 21	2106	Mode 21	2098	-0.40%	91.50%
Mode 22	2260	Mode 22	2196	-2.80%	84.60%
Mode 23	2326	Mode 23	2322	-0.21%	98.70%
Mode 24	2401	Mode 24	2377	-0.99%	40.50%
Mode 25	2406	Mode 26	2503	4.03%	31.50%
Mode 26	2440	Mode 25	2427	-0.55%	51.20%
Mode 27	2547	Mode 27	2565	0.71%	83.00%
Mode 28	2561	Mode 26	2503	-2.25%	52.50%
Mode 29	2635	Mode 30	2657	0.85%	39.20%
Mode 30	2672	Mode 30	2657	-0.56%	17.20%
Mode 31	2729	Mode 31	2755	0.95%	30.70%
Mode 32	2768	Mode 32	2772	0.13%	76.70%
Mode 33	2809	Mode 33	2842	1.17%	27.80%
Mode 34	2817	Mode 33	2842	0.88%	15.90%
Mode 35	2870	Mode 35	2885	0.50%	85.70%
Mode 36	2882	Mode 35	2885	0.10%	85.30%
Mode 37	2901	Mode 35	2885	-0.57%	86.80%
Mode 38	2903	Mode 37	2953	1.70%	83.40%
Mode 39	2909	Mode 37	2953	1.51%	89.10%
Mode 40	2928	Mode 37	2953	0.86%	97.70%
Mode 41	2931	Mode 37	2953	0.75%	97.90%
Mode 42	2960	Mode 37	2953	-0.24%	99.90%
Mode 43	2966	Mode 38	2974	0.26%	94.00%

Table 4.6.1: Validation Substructuring Results. The worst frequency error is less than 5%. Mode shapes show less fidelity as judged by the MAC. Even when the MAC is low (see mode 9, the 3rd elastic mode), the mode shapes still show a strong visual resemblance (see 3rd row of Figure 4.6.1).

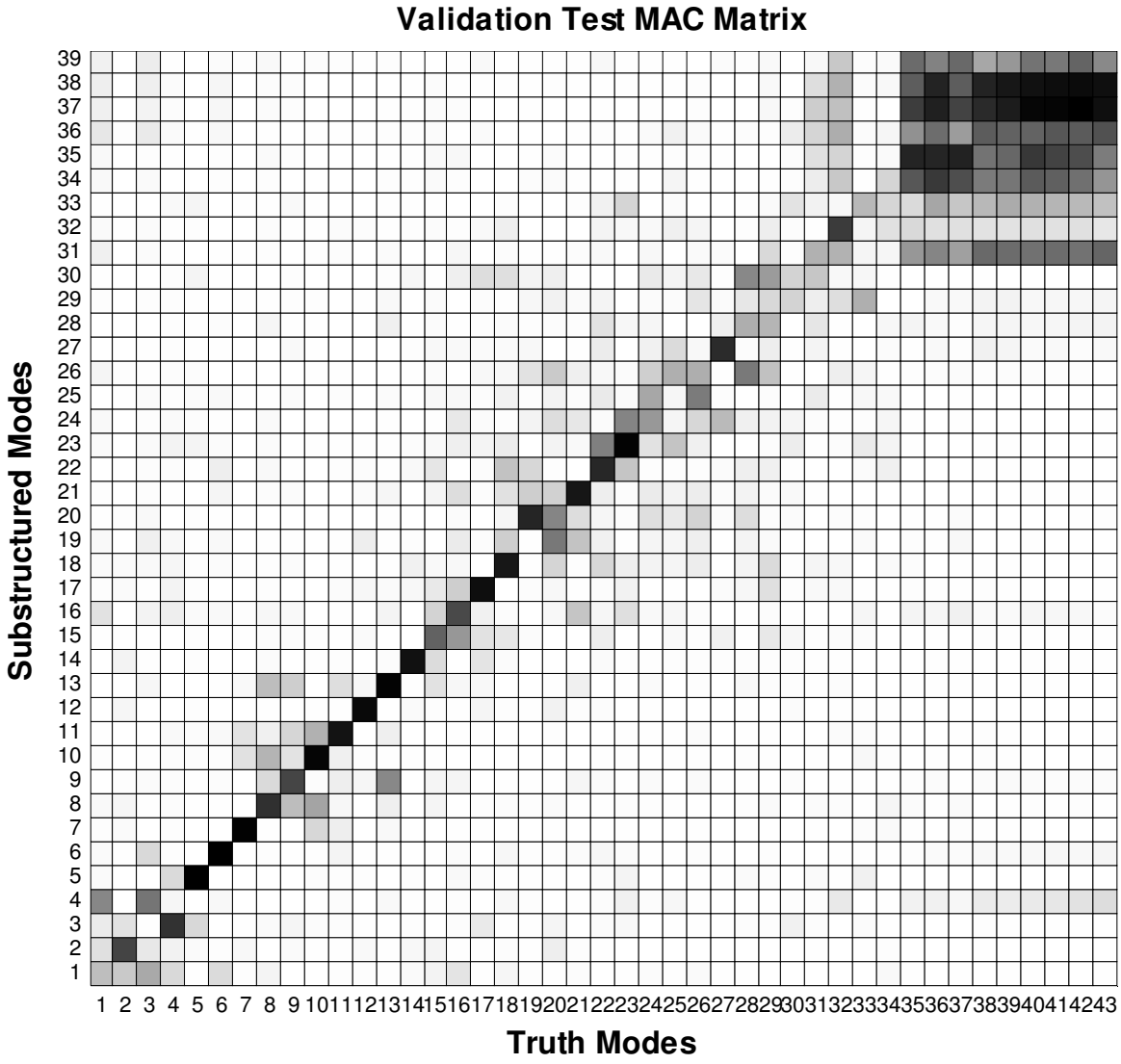

Figure 4.6.2: MAC comparison between truth modes (columns) and substructured modes (rows) of the Validation Test

4.6.2. Application Results

The application test results are shown in Table 4.6.2, Figure 4.6.3, and Figure 4.6.4. The results are also good up to just below 2500 Hz, with very good frequency matches and a few poor mode shape matches. After this range, the results break down significantly.

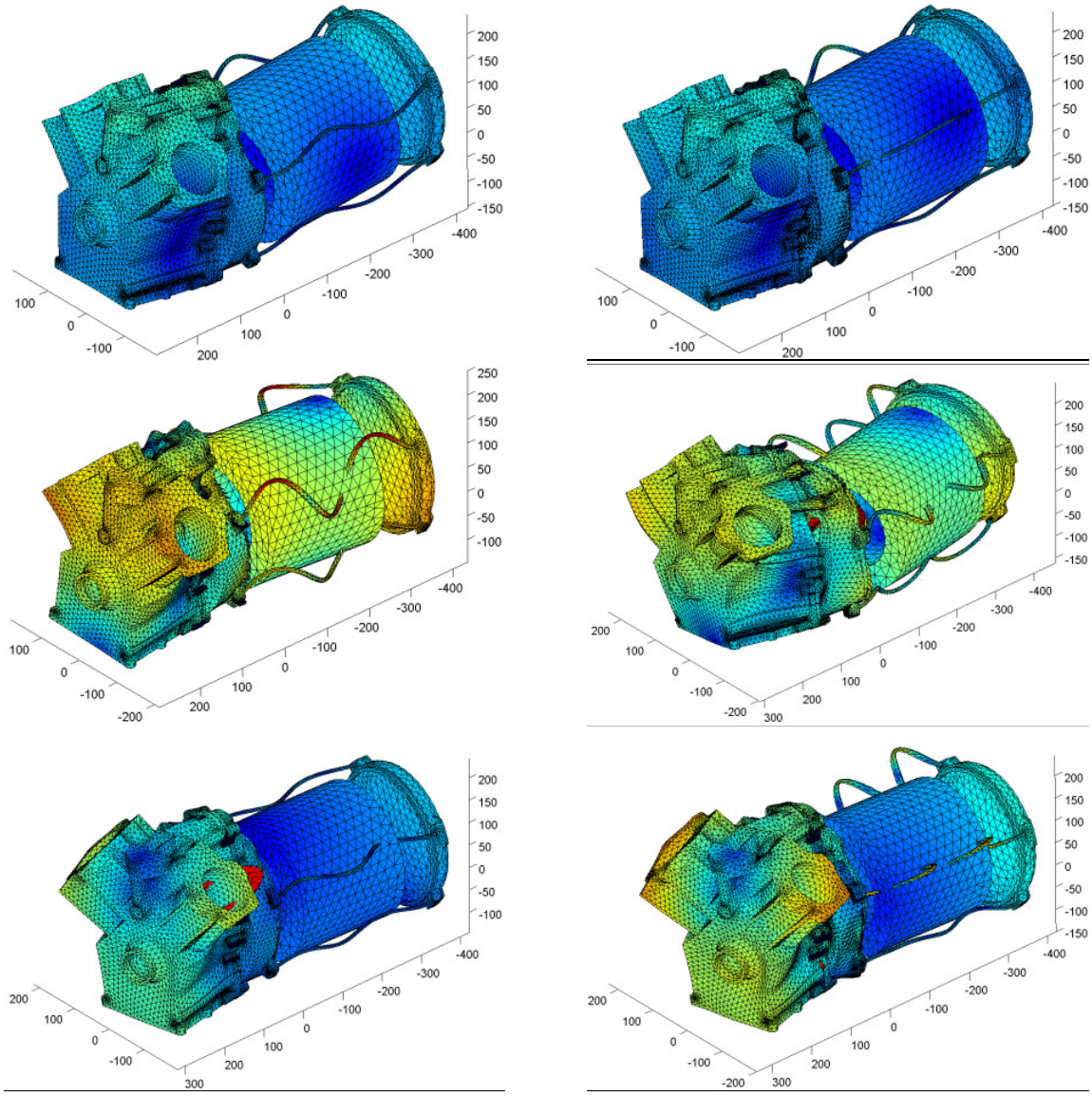

Figure 4.6.3: Elastic mode shapes of the application G=C-A+F truth test (left) and substructured prediction (right). Top: 1st Elastic mode – Large generator up-down bending. Middle: 2nd Elastic mode – Large generator left-right bending. Bottom: 4th elastic mode – Large generator left-right bending with large closure plate motion. The 3rd elastic mode consists primarily of motion on the bolts that attach the generator to the closure plate, so it is not shown here.

Truth Mode	Frequency (Hz)	Substr Mode	Frequency (Hz)	Error	MAC
Mode 7	925.7	Mode 8	927.0	0.1%	96.9%
Mode 8	959.0	Mode 9	976.7	1.9%	86.4%
Mode 9	1003	Mode 10	1022	2.0%	95.2%
Mode 10	1178	Mode 11	1190	1.0%	71.4%
Mode 11	1201	Mode 11	1190	-0.9%	80.5%
Mode 12	1295	Mode 13	1321	1.9%	97.2%
Mode 13	1349	Mode 14	1351	0.2%	98.7%
Mode 14	1428	Mode 15	1441	0.9%	91.6%
Mode 15	1457	Mode 16	1470	0.9%	68.9%
Mode 16	1490	Mode 17	1487	-0.2%	73.8%
Mode 17	1560	Mode 18	1572	0.8%	97.8%
Mode 18	1902	Mode 19	1887	-0.8%	95.0%
Mode 19	1933	Mode 20	1943	0.5%	86.4%
Mode 20	1977	Mode 21	1979	0.1%	93.1%
Mode 21	2075	Mode 22	2065	-0.5%	91.9%
Mode 22	2233	Mode 23	2127	-4.7%	65.2%
Mode 23	2326	Mode 24	2307	-0.8%	94.1%
Mode 24	2390	Mode 26	2412	0.9%	48.8%
Mode 25	2415	Mode 27	2432	0.7%	66.1%
Mode 26	2430	Mode 26	2412	-0.8%	42.2%
Mode 27	2537	Mode 32	2533	-0.2%	84.3%
Mode 28	2547	Mode 31	2471	-3.0%	37.0%
Mode 29	2605	Mode 33	2596	-0.3%	65.6%
Mode 30	2641	Mode 35	2636	-0.2%	41.9%
Mode 31	2710	Mode 36	2669	-1.5%	52.4%
Mode 32	2729	Mode 35	2636	-3.4%	26.3%
Mode 33	2771	Mode 37	2740	-1.1%	59.7%
Mode 34	2802	Mode 38	2782	-0.7%	38.4%
Mode 35	2846	Mode 39	2815	-1.1%	58.3%
Mode 36	2881	Mode 40	2883	0.1%	76.7%
Mode 37	2953	Mode 42	2957	0.1%	99.7%
Mode 38	2966	Mode 42	2957	-0.3%	98.5%

Table 4.6.2: Application Substructuring Results. Results are very similar to the validation test. The worst frequency error is only 5%, but the mode shapes have more error as judged by the MAC. Again, even poor MAC correlations (see truth mode 10, the 4th elastic mode) show strong visual resemblance (see bottom row of Figure 4.6.3).

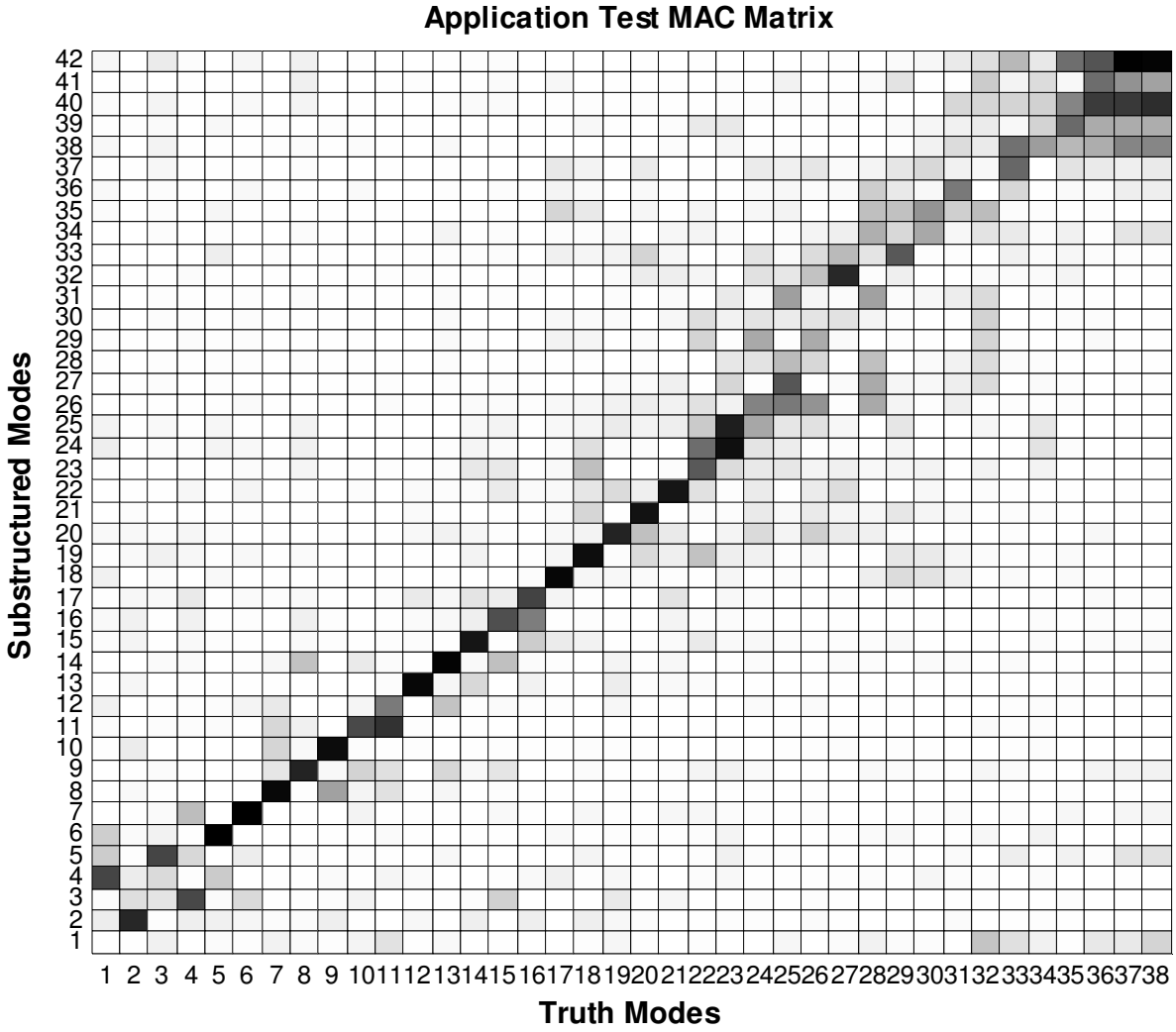

Figure 4.6.4: MAC comparison between the truth modes (columns) and substructured modes (rows) of the application test.

In both application and validation cases, the substructuring results were very good, but more importantly for this work, the application and validation tests matched each other very well. Ideally, the validation test results should mirror the application results, to give the analyst a good idea of the frequency range that his or her model is valid for, and also the approximate magnitude of errors that exist, and these two tests mirror each other exceedingly well. Both

show very good agreement in frequencies and slightly worse agreement in the mode shapes. Both tests also show the fidelity of the model deteriorates after approximately 2500 Hz.

4.7. Testing Variations

A short investigation was performed to see the effect that using different numbers of modes in each subsystem had on the results. For all MAC plots in the following sections, note that the first six rows and columns are rigid body modes and may appear as linear combinations of one another. The MAC correlation will typically not be good for rigid body modes.

4.7.1. Investigating the Number of Constraint Modes

In the substructuring examples of section 2, the transmission simulator was assumed to be rigid over the frequency band of interest; only six rigid body modes of the transmission simulator were used to create the subtracted model. In this test, the transmission simulator had a large number of modes in the frequency band of interest, but recent work [11] has shown that even in a system with complex motion of the transmission simulator, fairly good results can be achieved using a rigid model of the transmission simulator; the averaging that takes place in the modal constraints can actually achieve a good fit to the truth data. These systems will also be examined to see how many modes are needed in the transmission simulator model to achieve good results.

The substructuring calculations were repeated with each using a different number of modes in the transmission simulator model (and consequently number of constraint equations). Using only six rigid body modes, very poor results were achieved. The MAC between the

two systems shows very poor correlation between the mode shapes and frequencies are in error. Approximately 20 modes were needed before the majority of modes correlated well.

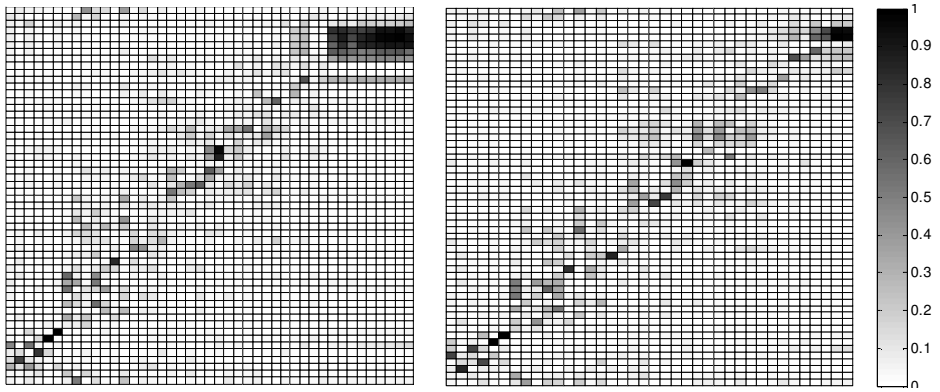

Figure 4.7.1: MAC plots of the validation (left) and application (right) using 6 modal constraints. Correlation is poor.

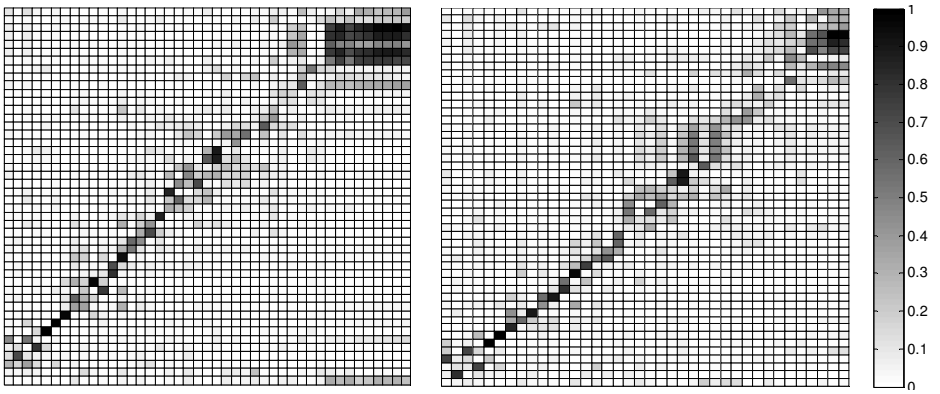

Figure 4.7.2: MAC plots of the validation (left) and application (right) using 14 modal constraints. A stronger diagonal exists but correlations are still poor.

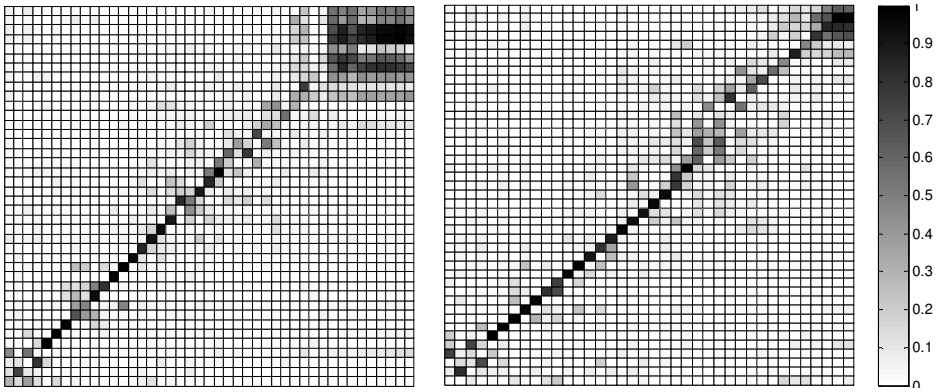

Figure 4.7.3: MAC plots of the validation (left) and application (right) using 20 modal constraints. A strong diagonal represents good correlation.

The validation and application test match each other very well in each case studied. This suggests that the validation test can be used to determine how many constraints should be used in the application of interest.

4.7.2. Investigating the Truncation Frequency

Another parameter of the experiment is the truncation frequency. Extracting modes can be a labor intensive process, so if only the first few elastic modes of the system are of interest, it may not be worth extracting modes all the way up to 3000 Hz. This investigation varies the frequency limit of the test from 3000 Hz (3x the natural frequencies of the first elastic modes) down to 1000 Hz (approximately at the level of the first elastic modes). Results are shown in Figure 4.7.4 and Figure 4.7.5.

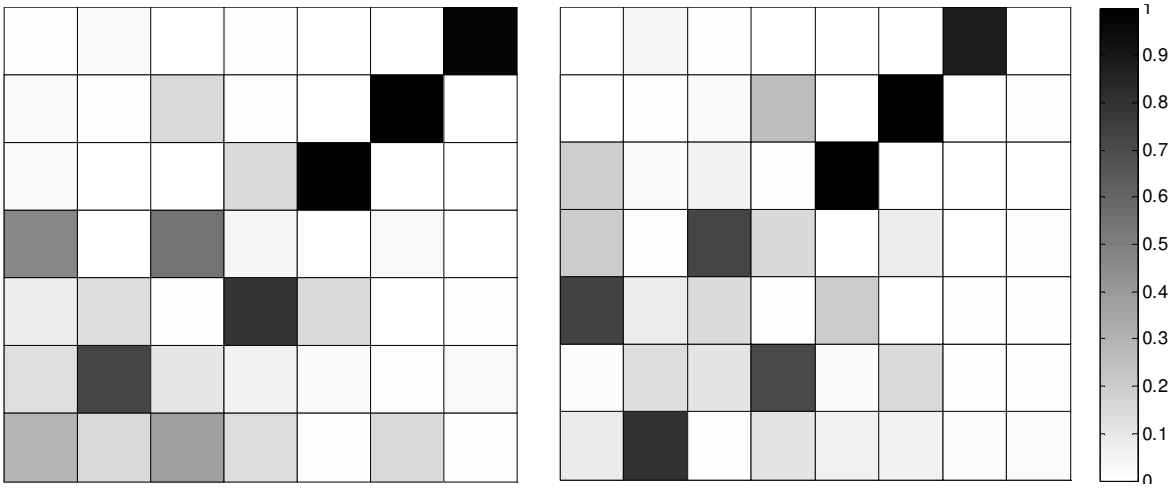

Figure 4.7.4: MAC plots of validation (left) and application (right) with all systems truncated at 1000 Hz. The first elastic mode of each test was captured surprisingly well (the first six modes are rigid body modes). The second elastic mode of the application test (near 960 Hz) was missed. The second elastic mode of the validation test is out of band (near 1080 Hz).

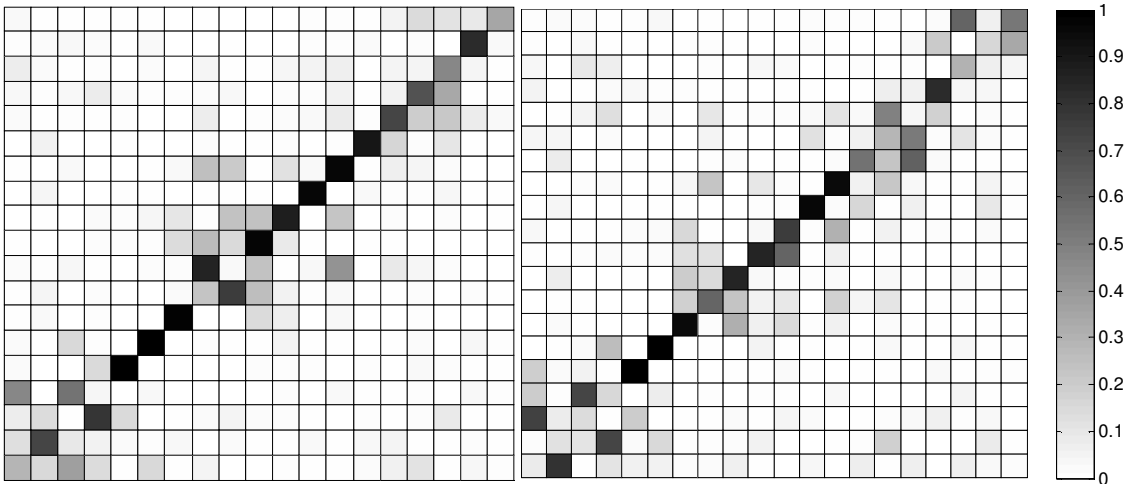

Figure 4.7.5: MAC plots of validation (left) and application (right) with all systems truncated at 2000 Hz. With a few exceptions, good results are obtained up to 1500 Hz.

Surprisingly good results were obtained for approximately 75% of the frequency band. Frequencies were much more accurate than mode shapes. Even in the case where the models

were truncated at 1000 Hz, only 1.6% error was found between the substructured and truth frequencies.

4.8. Discussion

This effort successfully simulated experimental substructuring of an engine and generator system by applying the experimental constraints of modal truncation and limited sensor placement. By placing sensors optimally, an efficient use of sensors was achieved. 20 triaxial accelerometers were placed on the plate and engine, and 10 were placed on each generator. Some modes consisting of motion primarily on localized geometry were discarded as they would not show up strongly on an FRF of the system and therefore would not be extracted accurately.

Good results were achieved for the first few elastic modes. It was found that for a particular frequency band of interest, all of the transmission simulator mode shapes that exist in that band should be used for the constraint. By truncating the number of modes in the transmission simulator, it was found that the least-squares transmission simulator constraints were not satisfied as well, so there were errors in the subtraction. This limited the frequency range of the substructuring predictions, as shown in Figure 4.7.1 through Figure 4.7.3.

Most importantly, it appears that the validation test is a good way to judge substructuring predictions in the application of interest, even for this complicated system. The validation test followed the application predictions very well. In the investigation of different substructuring parameters, both application and validation tests followed similar trends.

Errors in frequencies and mode shapes were consistent, and the frequencies at which the tests lost fidelity were similar.

5. Conclusions

Several tests and investigations were performed to further investigate the fidelity of experimental-to-analytical substructuring. Simply by attempting substructuring calculations with experimental models, one begins to see what works well and what doesn't work. Several sensitivities and important considerations were discovered or reinforced.

The test setup can play a large role in the robustness of a substructuring attempt. By carefully choosing where to draw the boundaries between the two substructures, the method can be made more robust. In the wind turbine examples, two different joints were chosen for the interface where substructuring would occur. In the first test, the joint consisted of three bolts over a small area. In the second test, the joint between the two models was spread over a larger space. The transmission simulator was able to average motion over a much larger area, so more robust constraints were created.

Rigid body mode accuracy was very important for accurate substructuring predictions. Due to their low frequencies, they often cannot be measured and must be constructed analytically. Accurate mass properties are important for constructing rigid body modes, so these should either be measured with a mass properties machine or calculated from a good model. When rigid body modes can be measured, they are often at the lower limit of the accelerometer sensitivity, so they appear noisy. It was found in the tower test in Section 2.2.2 that better

results could be obtained by fitting perfect rigid body modes of the three principal translations and rotations to the measured, noisy modes to smooth out these errors.

As the two wind turbine tests show, one can still get poor results with the transmission simulator method, but it wasn't clear in either test which was good or bad until the results were compared to the truth data. If no truth test is available, one cannot be sure how good the results are. This thesis used the concept of a validation test to evaluate substructuring predictions in the face of experimental error. Different error models were used to apply random error to the experiment. The frequency distributions of the substructuring predictions collected in this study had high kurtosis, so outliers were common even though the majority of the tests were well-behaved. In general, modes that were more sensitive in the validation test were also found to be more sensitive in the application test. On a trial-by-trial basis, the application test accuracy was well predicted by the validation test, except in the case of outliers which rarely can show a severe divergence. The validation test therefore gives a reasonable level of confidence to the substructured model, but results should still be viewed with suspicion and evaluated with solid engineering judgment in case the test is one of the rare outliers.

The validation concept was further tested by applying it to an engine/generator system. This application had a much more complicated interface and was modally dense. Similar to the successful wind turbine test, the natural 'joint' to include in each subsystem was the closure plate, which is the component that connects the generator to the engine. But, with a much more complex joint, extra effort was expended to ensure that the shapes of the closure plate would be adequate to capture the motion of the closure plate attached to a generator and the

engine. The transmission simulator was mass loaded with a mock-generator that mimicked the interface of an actual generator. And, by containing the actual geometry of the closure plate in the transmission simulator, as opposed to some reduced or defeatured plate, a very natural modal constraint could be applied without the need for interpolation of mode shapes to points that don't exist on a different structure.

Very good results were obtained using the transmission simulator method with the generator and engine. A brief investigation into the number of modes contained in each substructure showed the accuracy was fairly resistant to truncation issues, which gives confidence in models derived from careful modal tests. Additional confidence was also gained in the performance of a validation test, which accurately predicted application results in all cases studied.

Throughout this work, different ways to make the substructuring process more cost-effective were also explored. By making the transmission simulator an actual piece of the experimental hardware that already exists in the substructure, the cost of procurement of a transmission simulator is reduced. If the transmission simulator can be assumed to be rigid over the band of interest, the cost of creating an accurate model can also be reduced. Similar trends can be shown for the validation experiment. By choosing an alternative application fixture as a validation fixture (e.g. validating with a different generator, as was done in this work), there will likely already be an accurate model of the fixture, so the effort to create one does not need to be duplicated. The cost of procurement of the validation fixture is also reduced since the hardware likely exists.

The work contained in this thesis shows that experimental substructuring can be viable if a little extra effort is put forth to carefully apply the transmission simulator method, and confidence can be obtained in the substructured model by performing a simple validation test. Although it is not yet possible to quantify the accuracy of the substructuring predictions using the validation test, this thesis has shown a strong qualitative link which should give the user a great deal confidence in the results of a substructuring prediction.

6. References

[1] D. De Klerk, D. J. Rixen, and S. N. Voormeeren. "General Framework for Dynamic Substructuring: History, Review and Classification of Techniques," *AIAA Journal*, Vol. 46, No. 5, pp. 1169-1181, 2008.

[2] R. L. Mayes and M. Arviso, "Design Studies for the Transmission Simulator Method of Experimental Dynamic Substructuring," *International Seminar on Modal Analysis (ISMA 2010)* Lueven, Belgium, 2010.

[3] M. S. Allen, D. C. Kammer, and R. L. Mayes, "Metrics for Diagnosing Negative Mass and Stiffness when Uncoupling Experimental and Analytical Substructures," *29th International Modal Analysis Conference (IMAC XXIX)* Jacksonville, Florida, 2011.

[4] R. L. Mayes, M. S. Allen, and D. C. Kammer, "Correcting Indefinite Mass Matrices with the Transmission Simulator Method of Substructuring," *30th International Modal Analysis Conference (IMAC XXX)* Jacksonville, Florida, 2012.

[5] M. S. Allen, R. L. Mayes, and E. J. Bergman, "Experimental Modal Substructuring to Couple and Uncouple Substructures with Flexible Fixtures and Multi-point Connections," *Journal of Sound and Vibration*, vol. 329, pp. 4891-4906, 2010.

[6] R. L. Mayes, "An Introduction to the SEM Substructures Focus Group Test Bed – The Ampair 600 Wind Turbine," *Proceedings of the 30th International Modal Analysis Conference (IMAC XXX)* Jacksonville, Florida, 2012.

[7] M. S. Allen and J. H. Ginsberg, "A Global, Single-Input-Multiple-Output (SIMO) Implementation of the Algorithm of Mode Isolation and Applications to Analytical and Experimental Data," Mechanical Systems and Signal Processing, vol. 20, pp. 1090-1111, 2006.

[8] J. Harvie and P. Avitable, "Comparison of Some Wind Turbine Blade Tests in Various Configurations," *Proceedings of the 30th International Modal Analysis Conference (IMAC XXX)* Jacksonville, Florida, 2012.

[9] D. P. Hensley and R. L. Mayes, "Extending SMAC to Multiple References," *Proceedings of the 24th International Modal Analysis Conference (IMAC XXX)* Jacksonville, Florida, 2012.

[10] D. P. Rohe and M. S. Allen, “Investigation into the Effect of Mode Shape Errors on Validation Experiments for Experimental-Analytical Substructuring”, *Proceedings of the ASME 2012 Int’l Design Engineering Technical Conferences & Computers and Information in Engineering Conference*, Chicago, Illinois, 2012.

[11] R. L. Mayes and D. P. Rohe, “Coupling Experimental and Analytical Substructures with a Continuous Connection Using the Transmission Simulator Method,” *Proceedings of the 31st International Modal Analysis Conference (IMAC XXXI)* Garden Grove, California, 2013.

[12] N. Moshin and D. Macknelly, “Modal Assessment of Wind Turbine Blade in Preparation of Experimental Substructuring,” *Proceedings of the 30th International Modal Analysis Conference (IMAC XXX)* Jacksonville, Florida, 2012.

[13] M. S. Allen, D. C. Kammer, and R. L. Mayes, “Uncertainty in Experimental/Analytical Substructuring Predictions: A Review with Illustrative Examples,” *Proceedings of the international Conference on Noise and Vibration Engineering*, Leuven, Belgium, 2010.

[14] M. S. Allen and D. C. Kammer, “Simple Experiments to Validate Modal Substructure Models,” *Proceedings of the 30th International Modal Analysis Conference (IMAC XXX)* Jacksonville, Florida, 2012.

[15] D. de Klerk, “How Bias Errors Affect Experimental Dynamic Substructuring,” *Proceedings of the 28th International Modal Analysis Conference (IMAC XXVIII)* Jacksonville, Florida, 2012.

[16] M. Mains and H. Vold, “Investigation of the Effects of Transducer Cross-Sensitivity and Misalignment Error on Modal Vector Correlation,” *Proceedings of the 13th International Modal Analysis Conference (IMAC XIII)* Nashville, Tennessee, 1995.

[17] B. W. Silverman, *Density Estimation for Statistics and Data Analysis*, London: Chapman and Hall, 1986.

[18] D. C. Kammer, “Sensor Set Expansion for Modal Vibration Testing,” *Mechanical Systems and Signal Processing*, vol. 19, pp. 700-713, 2005.

APPENDIX A: EXTRACTED MODES FROM TURBINE TEST 1

This appendix shows all elastic mode shapes extracted from test data for the substructuring attempt to couple a single blade to a turbine missing one blade.

Elastic Modes of the Blade and Transmission Simulator

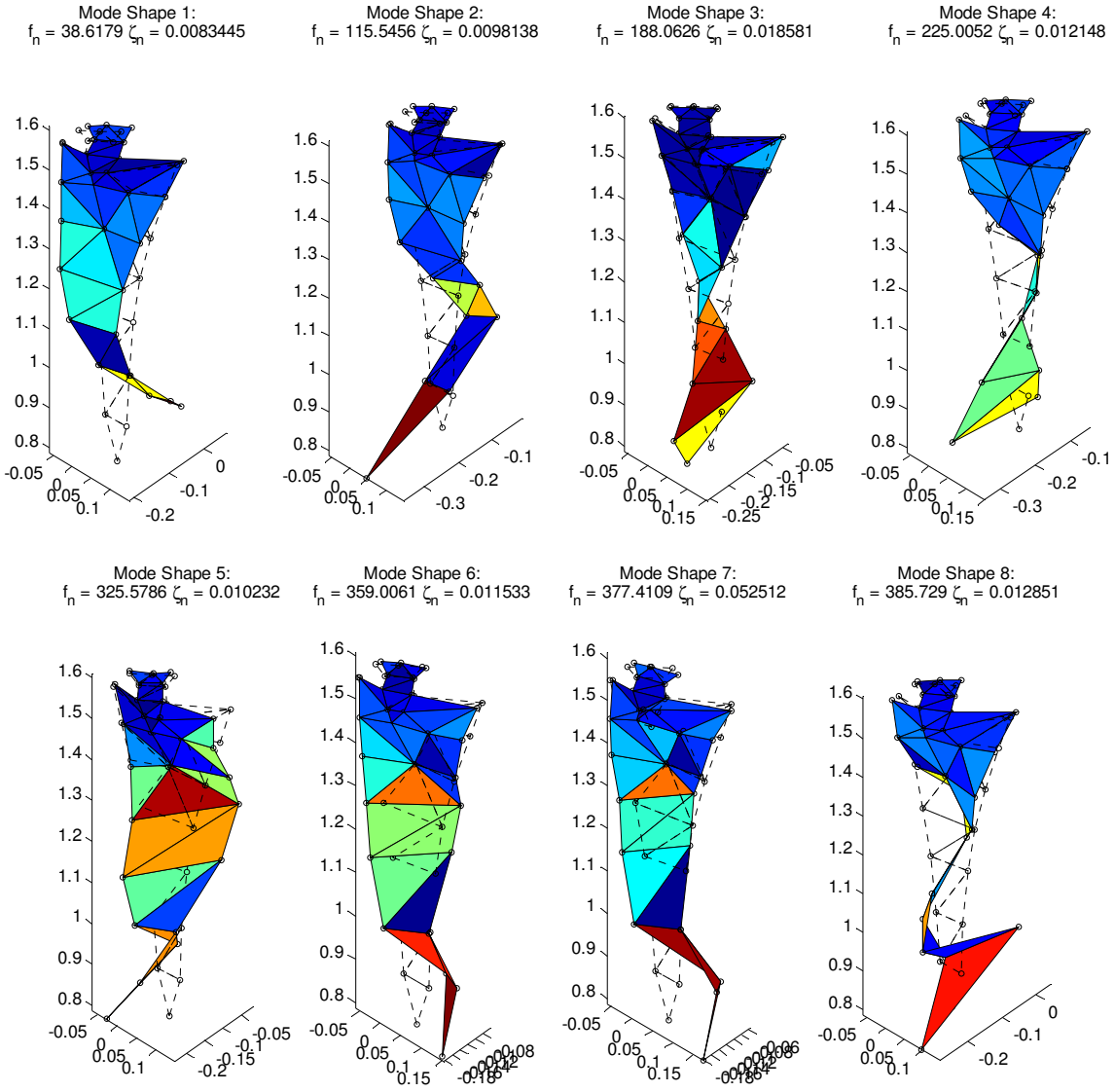

Elastic Modes of the Two-Bladed Turbine:

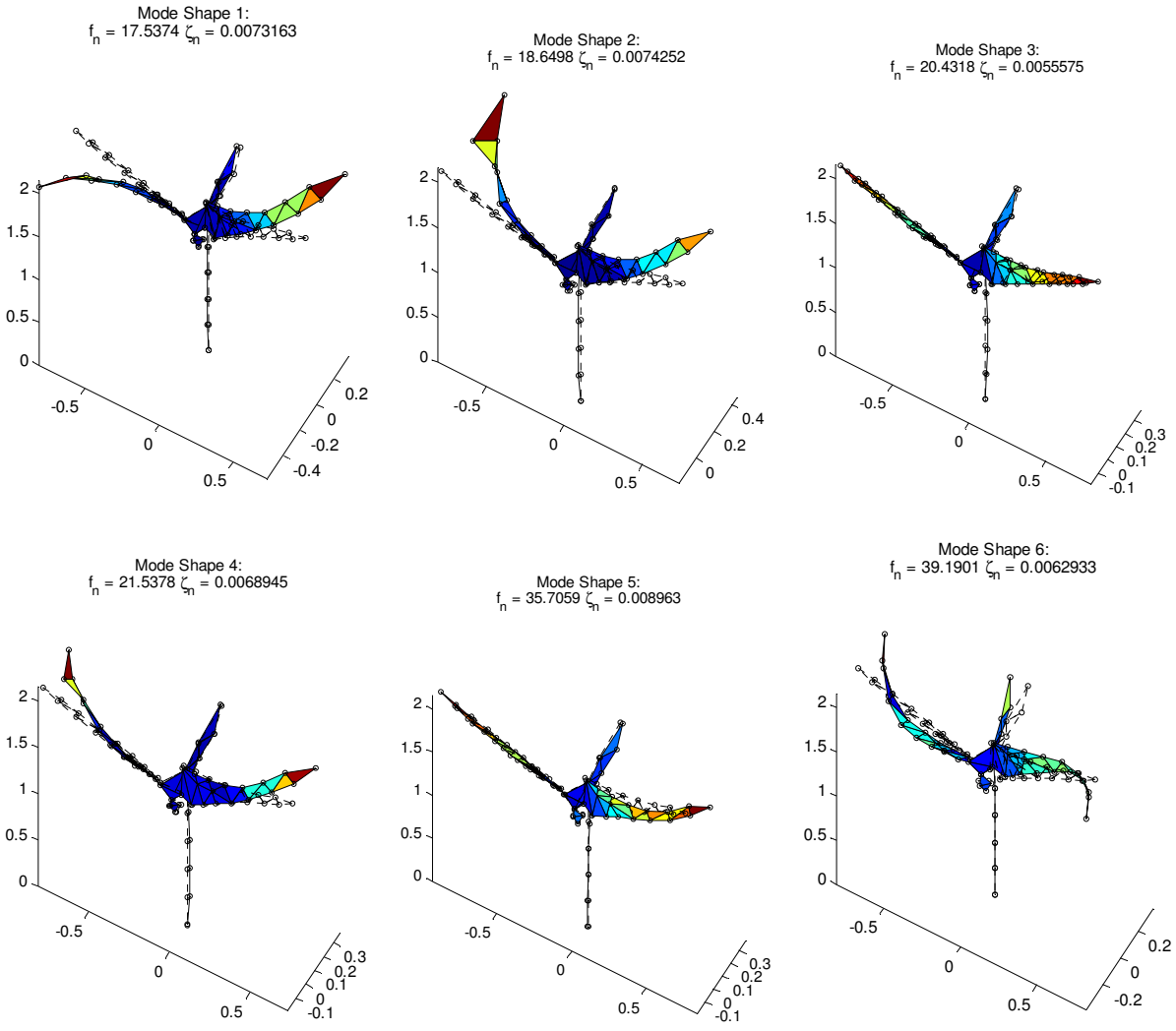

Mode Shape 7:
f_n = 58.2692 ζ_n = 0.01302

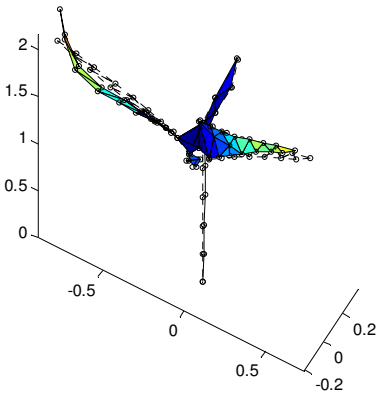

Mode Shape 8:
f_n = 61.6573 ζ_n = 0.015249

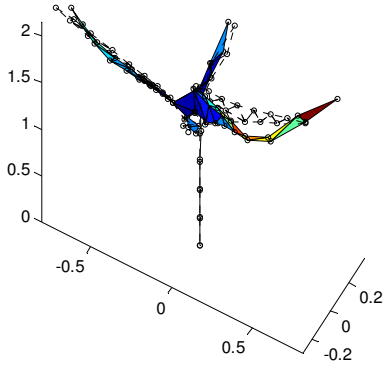

Mode Shape 9:
f_n = 73.3938 ζ_n = 0.0089323

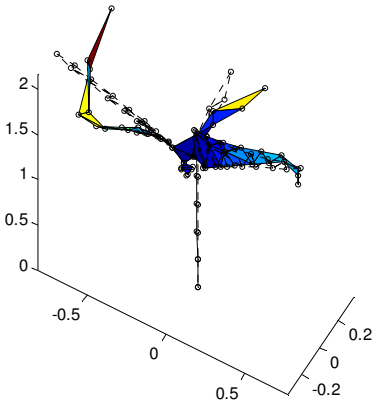

Mode Shape 10:
f_n = 81.3528 ζ_n = 0.01085

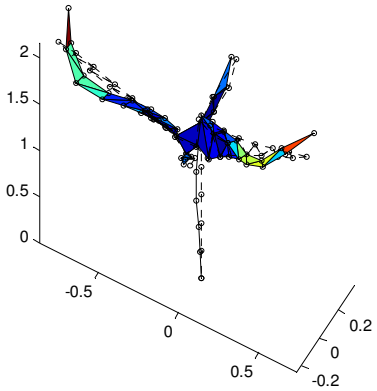

Mode Shape 11:
f_n = 99.6815 ζ_n = 0.011822

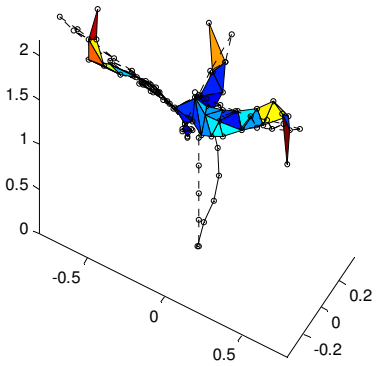

Mode Shape 12:
f_n = 100.0106 ζ_n = 0.0078916

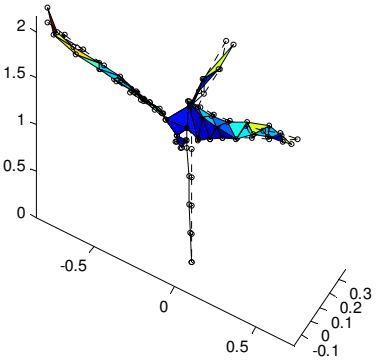

Mode Shape 13:
f_n = 108.7799 ζ_n = 0.0090221

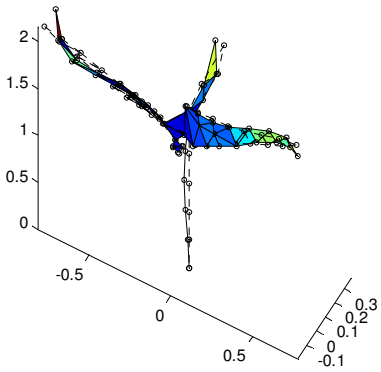

Mode Shape 14:
f_n = 132.9651 ζ_n = 0.010691

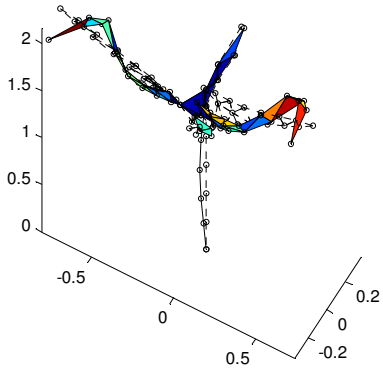

Mode Shape 15:
f_n = 147.9966 ζ_n = 0.0070186

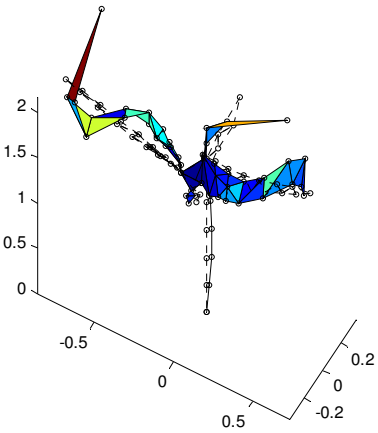

Mode Shape 16:
f_n = 167.9031 ζ_n = 0.015493

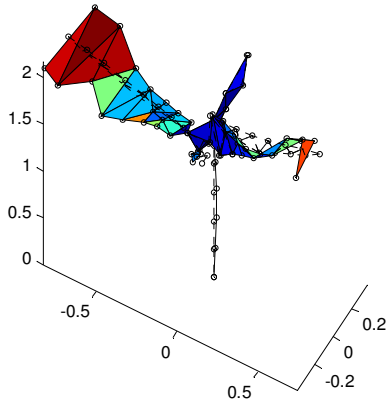

Mode Shape 17:
f_n = 179.6605 ζ_n = 0.015522

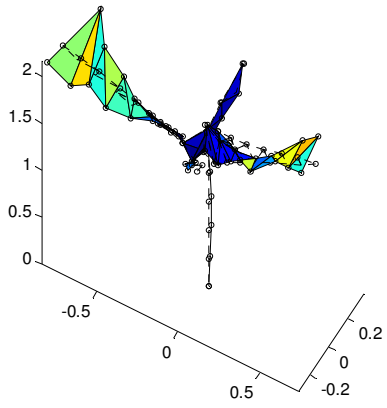

Mode Shape 18:
f_n = 201.2709 ζ_n = 0.0046436

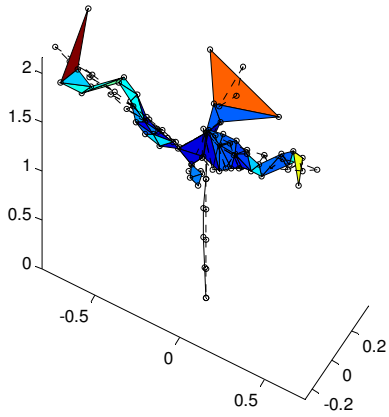

Mode Shape 19:
f_n = 202.9165 ζ_n = 0.010814

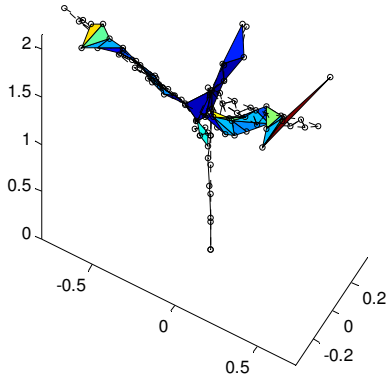

Mode Shape 20:
f_n = 217.4723 ζ_n = 0.0087274

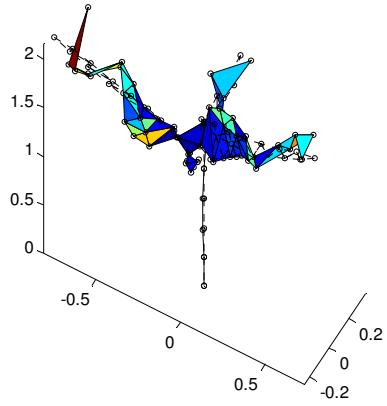

Mode Shape 21:
f_n = 235.8734 ζ_n = 0.0099543

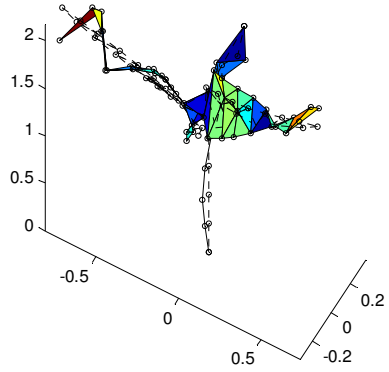

Mode Shape 22:
f_n = 242.2549 ζ_n = 0.0035291

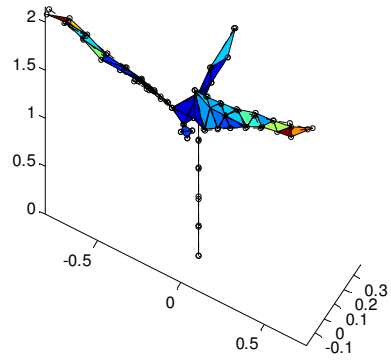

APPENDIX B: EXTRACTED MODES FROM TURBINE TEST 2

This appendix shows all modes extracted from test data for the substructuring attempt to couple a bladed hub to a bladeless tower.

Bladeless Tower Test:

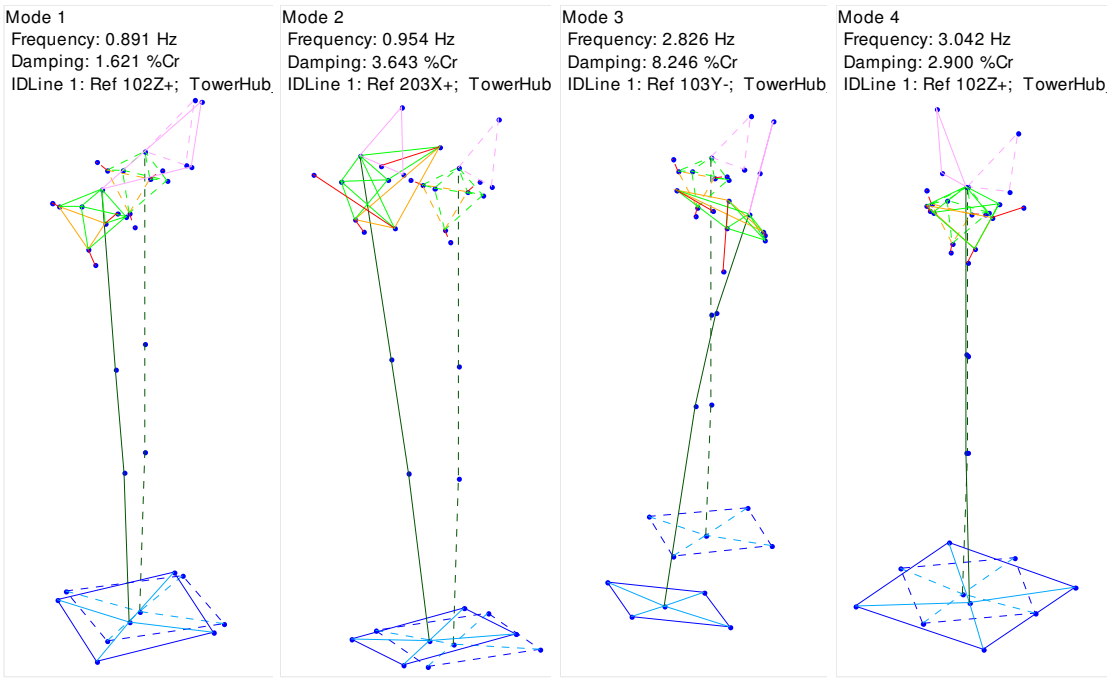

Mode 5
Frequency: 3.252 Hz
Damping: 6.578 %Cr
IDLine 1: Ref 102Z+; TowerHub

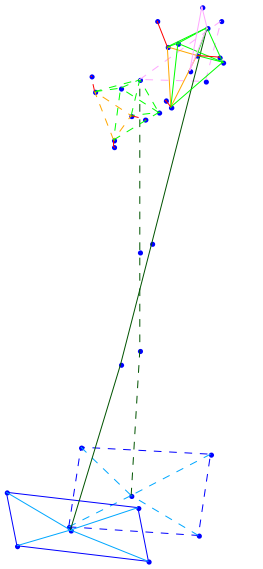

Mode 6
Frequency: 3.934 Hz
Damping: 6.696 %Cr
IDLine 1: Ref 203X+; TowerHub

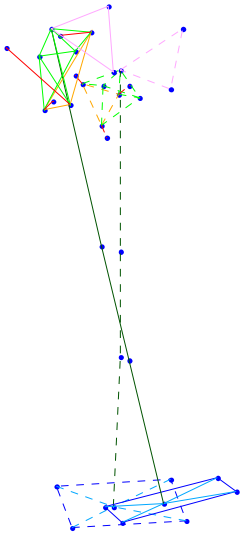

Mode 7
Frequency: 20.528 Hz
Damping: 1.012 %Cr
IDLine 1: Ref 203Z+; TowerHub

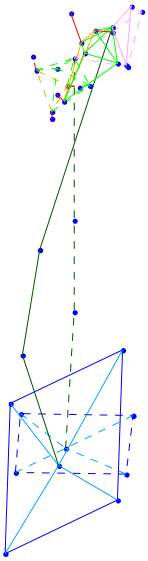

Mode 8
Frequency: 20.548 Hz
Damping: 0.950 %Cr
IDLine 1: Ref 203X+; TowerHub

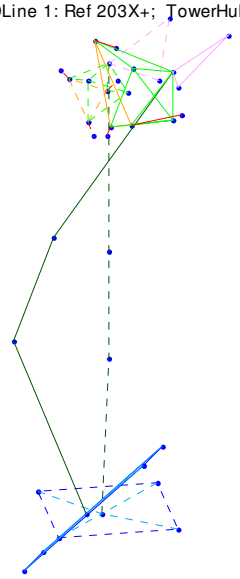

Mode 9
Frequency: 46.842 Hz
Damping: 0.253 %Cr
IDLine 1: Ref 502X+; TowerHub

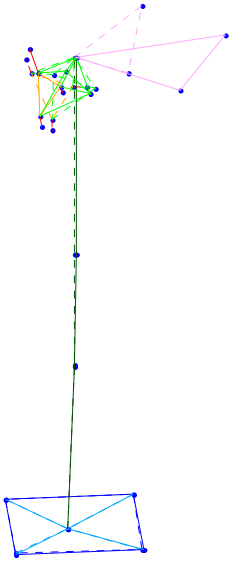

Mode 10
Frequency: 73.893 Hz
Damping: 0.702 %Cr
IDLine 1: Ref 203Z+; TowerHub

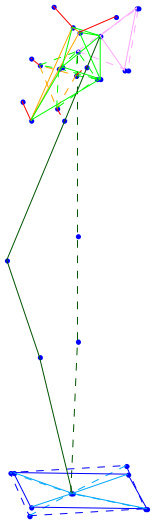

Mode 11
Frequency: 84.591 Hz
Damping: 0.708 %Cr
IDLine 1: Ref 203X+; TowerHub

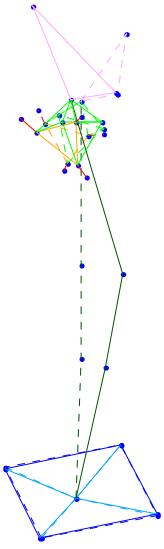

Mode 12
Frequency: 96.752 Hz
Damping: 0.303 %Cr
IDLine 1: Ref 502X+; TowerHub

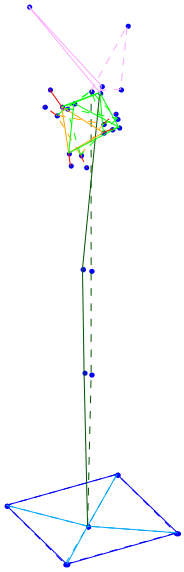

Mode 13
Frequency: 148.874 Hz
Damping: 1.502 %Cr
IDLine 1: Generated from reference 203X+

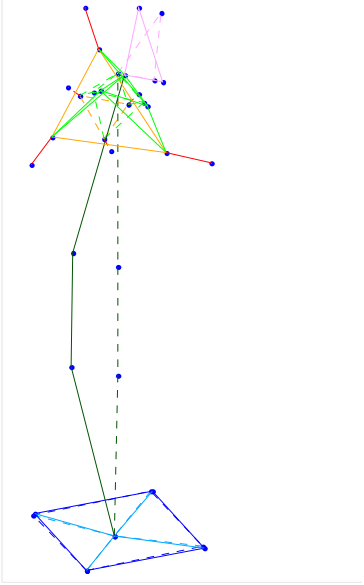

Bladed Hub Test:

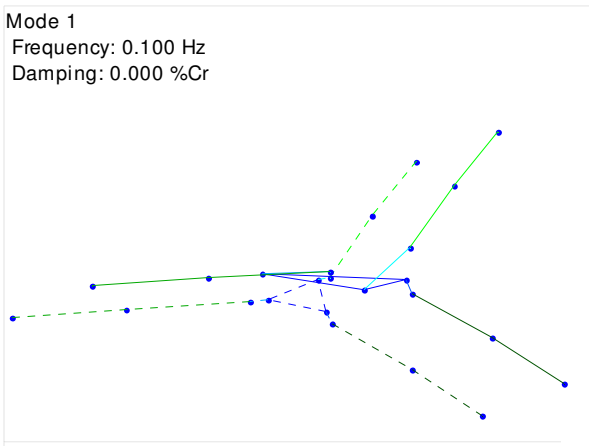

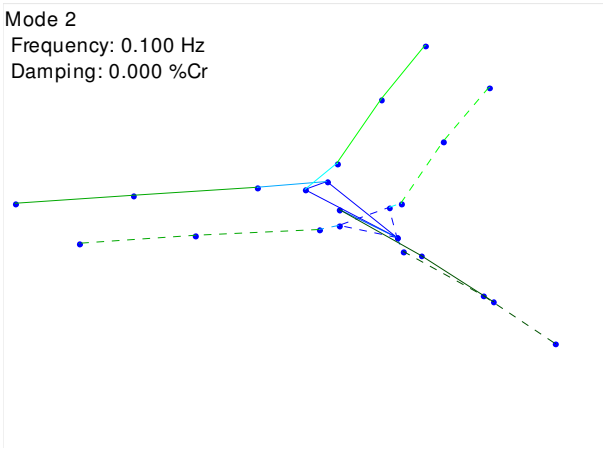

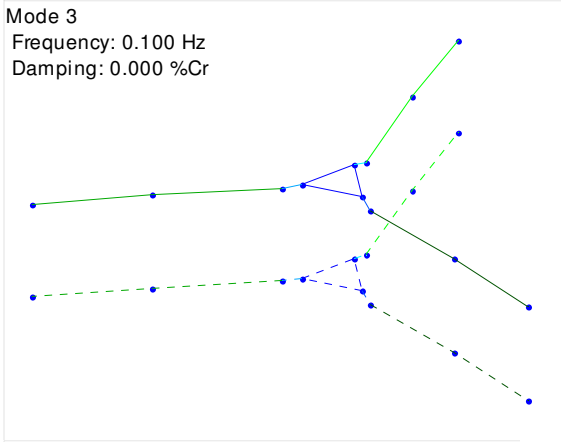

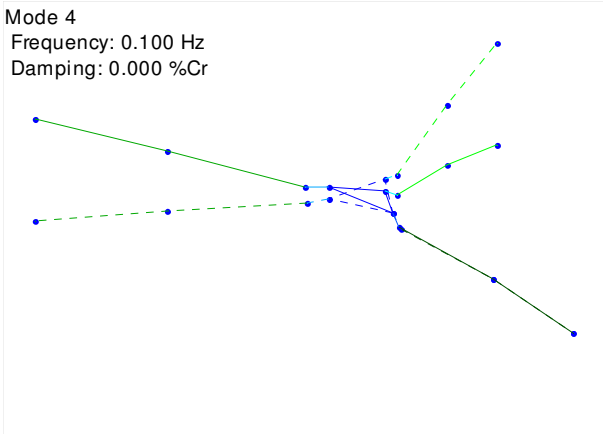

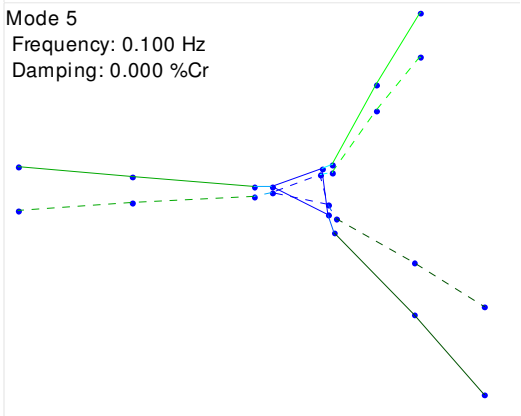

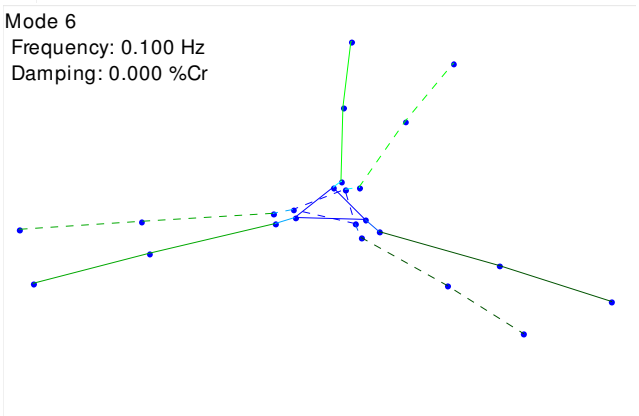

Mode 7
Frequency: 20.358 Hz
Damping: 2.172 %Cr
IDLine 1: Ref 606Z-; BladeHub_Run12_606Z-_7-27-2012.mat;

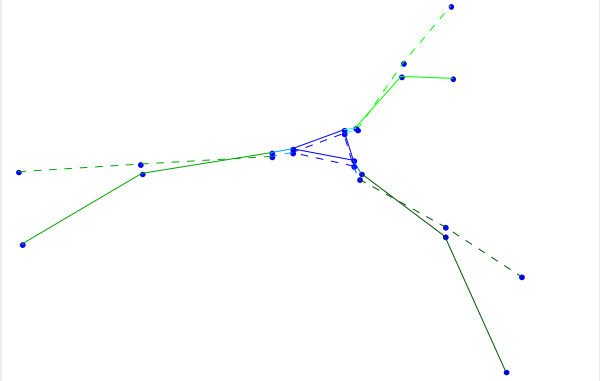

Mode 8
Frequency: 27.269 Hz
Damping: 1.752 %Cr
IDLine 1: Ref 602Z-; BladeHub_Run10_602Z-_7-27-2012.mat;

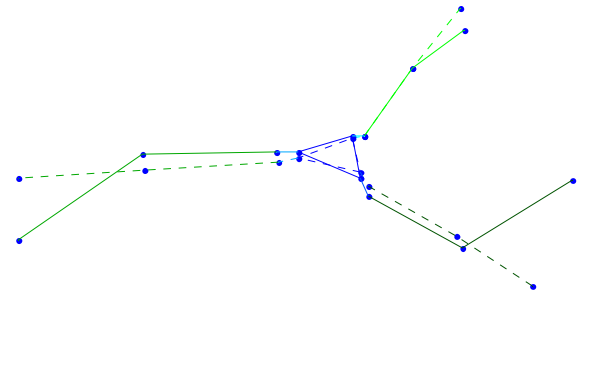

Mode 9
Frequency: 28.971 Hz
Damping: 1.842 %Cr
IDLine 1: Ref 604Z-; BladeHub_Run11_604Z-_7-27-2012.mat;

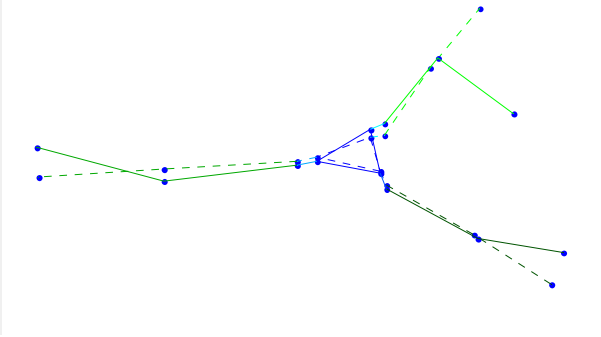

Mode 10
Frequency: 53.195 Hz
Damping: 3.275 %Cr
IDLine 1: Ref 604Y+; BladeHub_Run14_604Y+_7-27-2012.mat;

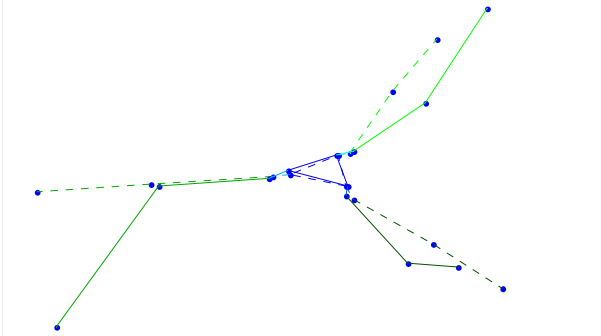

Mode 11
Frequency: 62.140 Hz
Damping: 1.815 %Cr
IDLine 1: Ref 602Z-; BladeHub_Run10_602Z-_7-27-2012.mat;

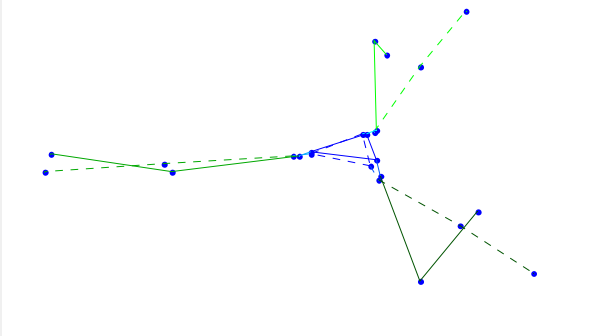

Mode 12
Frequency: 68.376 Hz
Damping: 1.761 %Cr
IDLine 1: Ref 606Z-; BladeHub_Run12_606Z-_7-27-2012.mat

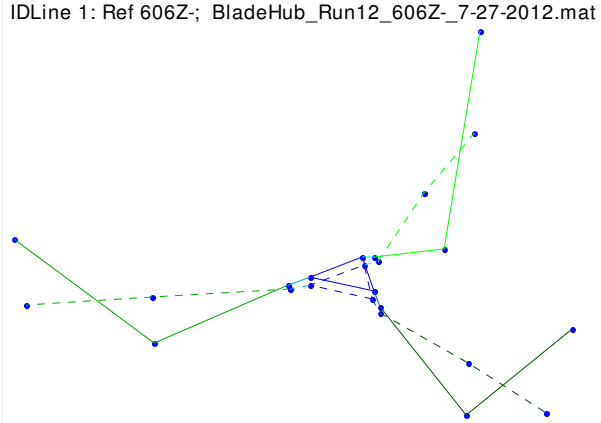

Mode 13
Frequency: 95.312 Hz
Damping: 2.144 %Cr
IDLine 1: Ref 602Z-; BladeHub_Run10_602Z-_7-27-2012.mat;

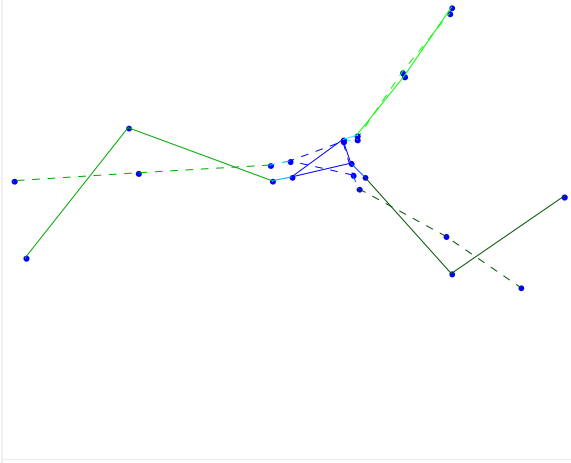

Mode 14
Frequency: 100.054 Hz
Damping: 1.500 %Cr
IDLine 1: Ref 606Z-; BladeHub_Run12_606Z-_7-27-2012.mat

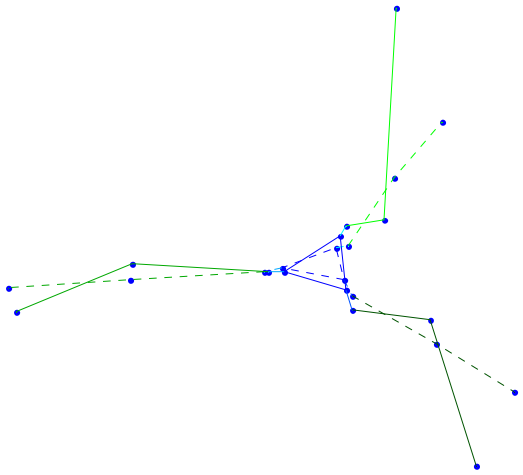

Mode 15
Frequency: 153.090 Hz
Damping: 2.487 %Cr
IDLine 1: Generated from reference 401Y-

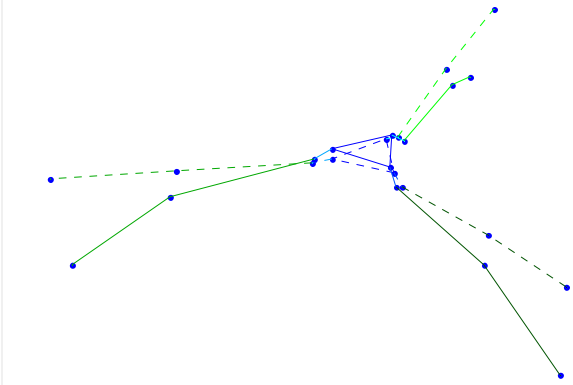

APPENDIX C: NATURAL FREQUENCIES OF THE GENERATOR SUBSTRUCTURES

This appendix lists the elastic natural frequencies of each system used in substructuring calculations. The first six elastic modes of each system are shown.

System A Frequencies	
Mode 7	958.0393
Mode 8	1170.307
Mode 9	1286.804
Mode 10	1333.689
Mode 11	1561.697
Mode 12	1881.035
Mode 13	2102.692
Mode 14	2290.604
Mode 15	2300.68
Mode 16	2488.312
Mode 17	2519.094
Mode 18	2633.457
Mode 19	2750.18
Mode 20	2825.679
Mode 21	2934.132

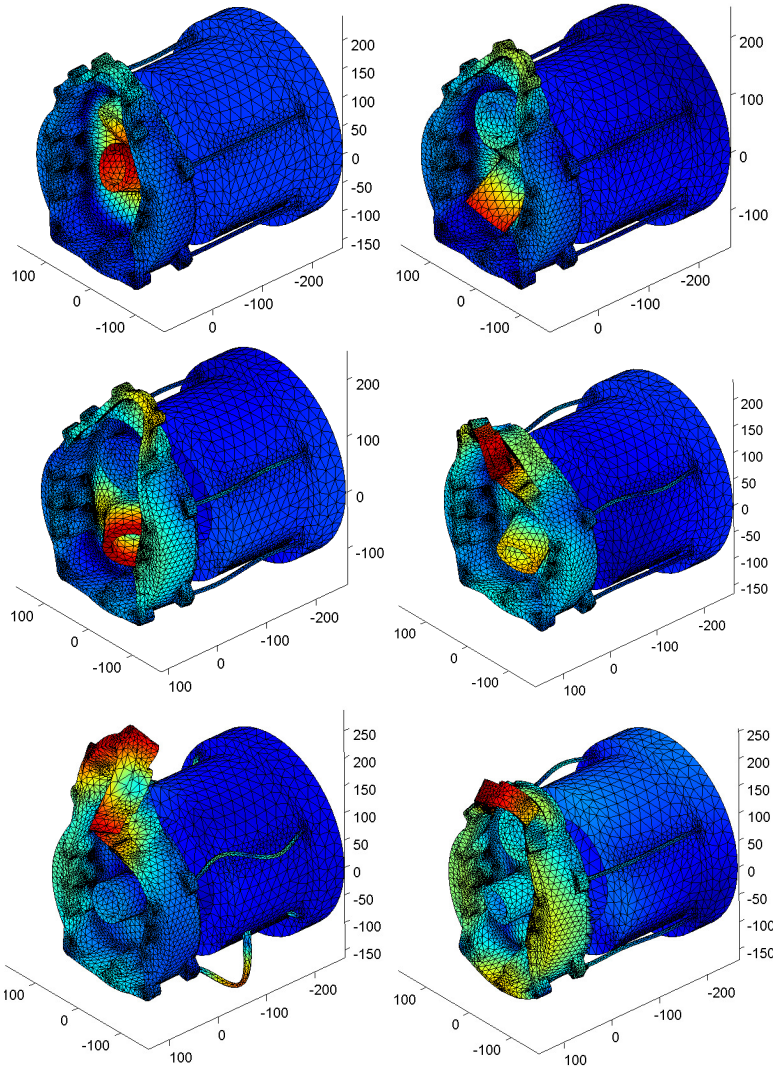

System C Frequencies	
Mode 7	950.7534
Mode 8	1116.986
Mode 9	1152.482
Mode 10	1223.029
Mode 11	1257.715
Mode 12	1344.796
Mode 13	1401.292
Mode 14	1521.488
Mode 15	1569.035
Mode 16	1768.224
Mode 17	1957.813
Mode 18	2032.912
Mode 19	2080.928
Mode 20	2174.226
Mode 21	2294.905
Mode 22	2326.496
Mode 23	2462.23
Mode 24	2507.599
Mode 25	2567.372
Mode 26	2623.225
Mode 27	2698.74
Mode 28	2762.349
Mode 29	2796.95
Mode 30	2827.731
Mode 31	2869.31
Mode 32	2941.103
Mode 33	2946.149
Mode 34	2962.536

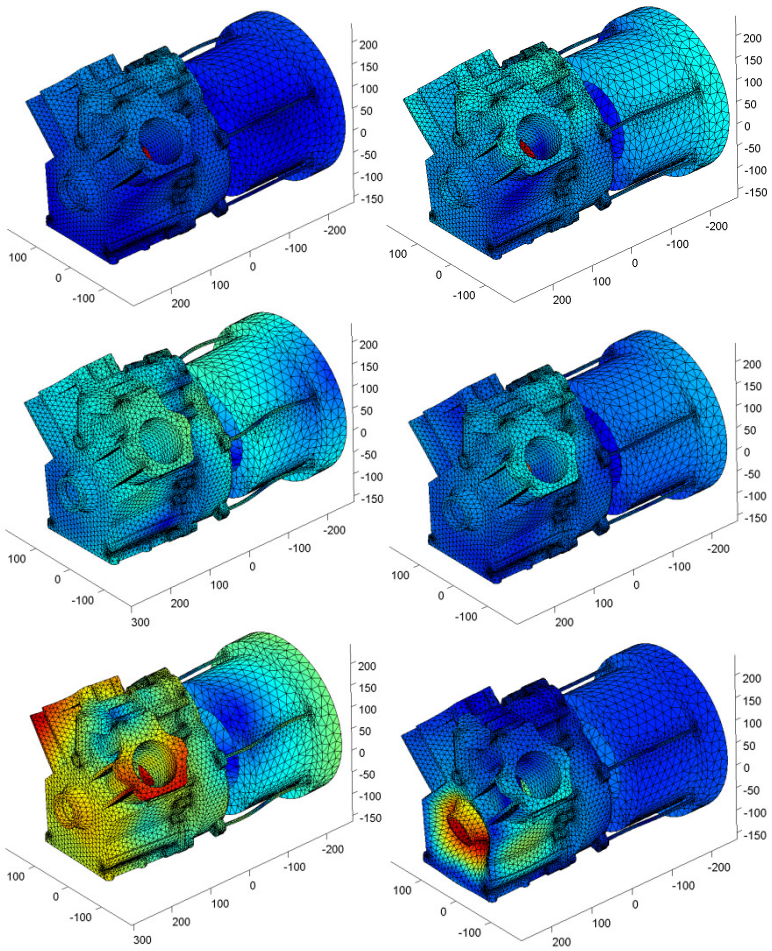

System D Frequencies	
Mode 7	954.2239
Mode 8	1166.893
Mode 9	1283.547
Mode 10	1332.963
Mode 11	1485.934
Mode 12	1570.28
Mode 13	1885.206
Mode 14	1972.954
Mode 15	2067.717
Mode 16	2246.474
Mode 17	2405.986
Mode 18	2489.46
Mode 19	2556.316
Mode 20	2632.675
Mode 21	2661.95
Mode 22	2775.684
Mode 23	2842.915
Mode 24	2884.234
Mode 25	2919.044
Mode 26	2952.463

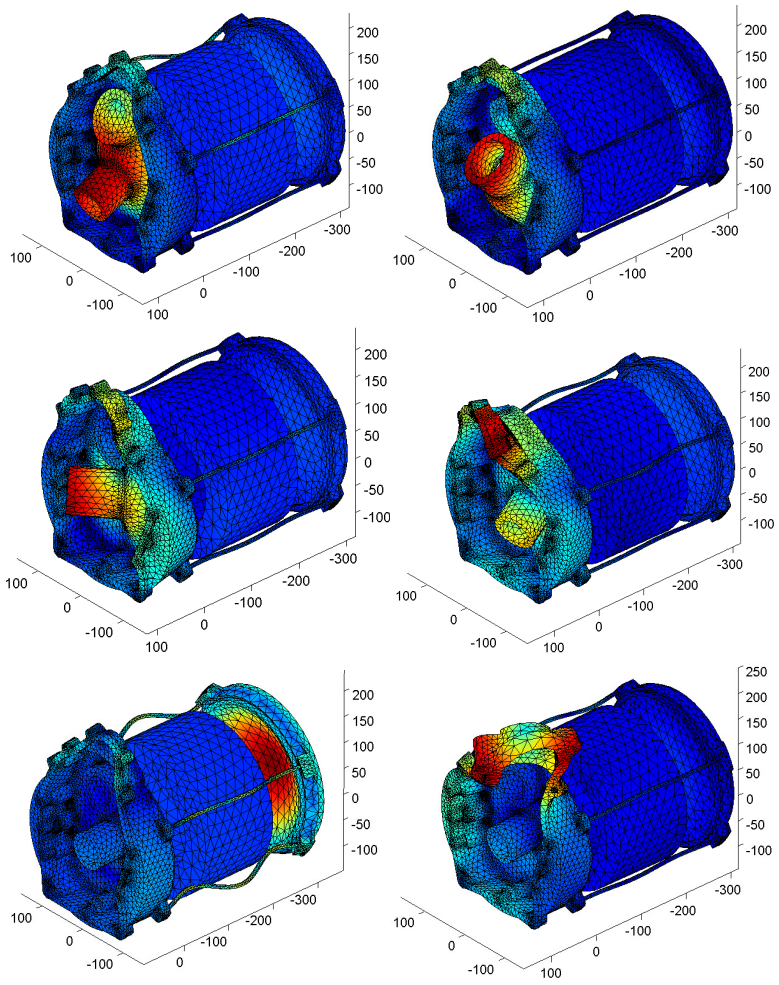

System F Frequencies	
Mode 7	948.7808
Mode 8	1163.362
Mode 9	1276.056
Mode 10	1321.855
Mode 11	1470.034
Mode 12	1572.061
Mode 13	1806.452
Mode 14	1855.186
Mode 15	1939.32
Mode 16	2222.04
Mode 17	2412.477
Mode 18	2432.3
Mode 19	2437.187
Mode 20	2449.113
Mode 21	2453.044
Mode 22	2468.844
Mode 23	2526.869
Mode 24	2597.12
Mode 25	2651.627
Mode 26	2686.16
Mode 27	2782.983
Mode 28	2876.727
Mode 29	2975.773